INAUGURAL-DISSERTATION

zur

Erlangung der Doktorwürde

der

Naturwissenschaftlich - Mathematischen

Gesamtfakultät

der

Ruprecht-Karls-Universität

Heidelberg

vorgelegt von

Dipl.Phys. Bernd Buchholz

aus Celle

Tag der mündl. Prüfung: 15.2.1995

Thema

Acoustically Heated Chromospheres of Late Type Stars

Gutachter: Prof. Dr. Peter Ulmschneider

Priv.Doz. Dr. Joachim Krautter

Abstract

We have calculated time dependent models of acoustically heated chromospheres for main sequence stars of spectral types F0 V to M4 V and for two giant stars of spectral types K0 III and K5 III.
The equations of hydrodynamics together with the equation of radiative transfer (RTE) are solved in order to investigate the propagation of acoustic waves into chromospheric regions. A new computational method has been developed which is able to solve the RTE on the very irregular depth grids resulting from the presence of shock discontinuities in the computational domain.
Molecular opacities of TiO and water vapor have been included to get realistic models for the coolest M-dwarfs.
The emergent radiation of the MgII h+k and CaII H+K lines has been calculated and compared with observations. We find good agreement of the time averaged emissions from both ions with the observed basal emissions which are thought to be due to a non-magnetic chromospheric heating mechanism operating in all late type stars. The height dependence of the acoustic heating can be explained by the limiting strength of the shocks and is consistent with the height dependence of heating observed for the quit sun.
Our results strongly support the idea that the basal non-magnetic heating mechanism for stellar chromospheres is due to the dissipation of acoustic wave energy.

Contents

Chapter 1

Introduction

1.1 Hot Layers around Cool Stars

The first star for which the existence of an outer atmospheric layer of high temperature became apparent was our Sun. The identification of emission lines in coronal spectra as due to forbidden transitions in highly ionized atoms by Grotrian (1939) and later Edlen (1941) could only be explained by the fact that the corona, which is visible during eclipses, must consist of extremely rarefied gas at extremely high temperatures of up to several million degrees.

While the corona extends to a distance of several solar radii beyond the photospheric limb, the chromosphere is a rather thin layer, which at eclipses flashes up in the red light of H_α a few seconds before and after totality. The solar chromosphere extends from the temperature minimum at about 500 km above the basis of the photosphere (defined by the level where the optical depth $\tau_{5000\,\text{Å}} = 1$) to a height of 2000 km, where the temperature reaches values of about 10000 K. From this height a thin transition layer connects the chromosphere with the overlying corona.

The results of the Einstein and IUE satellites, both launched in 1978, then demonstrated that practically all stars (with the possible exception of A-stars) have hot outer layers and thus are largely similar to our Sun. The stars hotter than spectral type A show X-ray emission which are now known to arise from hot blobs of gas moving in the extended winds of these stars. For stars later then spectral type A chromospheres and coronae similar to those of the Sun are found except for the cool red giants beyond the Linsky-Haisch dividing line, where coronae are absent, yet these stars too have chromospheres.

Among the indicators for chromospheres and coronae are spectral lines of abundant atoms with moderate to high levels of ionization. Most important as chromospheric diagnostics are the CaII H +K lines at $\lambda = 3968\,\text{Å}$ and $\lambda = 3934\,\text{Å}$ and the MgII h+k lines at $\lambda = 2803\,\text{Å}$ and $\lambda = 2796\,\text{Å}$. For stars with chromospheres, these lines have a typical line shape.

In late type stars the CaII H and K lines are strong and have very extended wings. An emission feature is always seen at the center of the line. This emission feature is often double peaked. The central dip is the result of self reversal of the emission core due to the large optical depth in the line.

The photospheric background in the ultraviolet part of the spectrum is weak for late type stars. Therefore and because of the high abundance of magnesium relative to calcium, the MgII h+k emission lines are often easier to detect than CaII H+K. MgII emission lines are found in all main sequence stars of spectral types later than F2 (Böhm-Vitense and Dettman, 1980).

Variations of the absolute and relative strengths of the diagnostic lines give the possibility to analyze the physical nature of these hot layers and the processes responsible for their existence.

1.2 Mechanisms of Heating

The existence of chromospheres and coronae is only possible if there is a heating mechanism which constantly provides the amount of energy necessary to maintain the large radiative cooling loss of such high temperatures. Because heating by convection or conduction from the cooler photosphere can be ruled out by the second law of thermodynamics, there must exist a nonthermal heating mechanism. Without a persistent heating, radiative energy losses would cool down the hot gas to the radiative equilibrium boundary temperature $T_{\rm RE} = 2^{-1/4} \cdot T_{\rm eff}$ ($\approx$ 4900 K for the Sun) within a timescale comparable to the radiative damping time $t_{\rm rad}$ which for the chromosphere is less than 10 min (Ulmschneider, 1971).

All stars later than spectral type A possess convection zones where the main process of energy transport is the turbulent motion of convection cells. Overshooting makes the turbulent motions visible to the observer. In case of the Sun, these motions can be observed directly and for stars they show up in the asymmetry of photospheric spectral lines (Gray, 1989).

The pressure fluctuations caused by the turbulence produce acoustic waves which propagate down the steep density gradient of the outer stellar layers and will form shocks. These shocks then heat the extremely thin outer stellar layers. This idea, first mentioned by Biermann (1946) was suggested by the fact that any turbulent flow zone invariably generates sound. This idea of acoustic wave heating was also supported by calculations of Lighthill (1952), who showed that the acoustic wave generation is proportional to the eighth power of the turbulent velocity, a relation which in subsequent terrestrial experiments on the generation of aircraft noise was beautifully confirmed (e.g. Goldstein, 1976).

Yet the Einstein and IUE results conclusively showed that the chromospheric emission strongly depends on the amount of magnetic flux present on the stellar surface. This same dependence is also found for different regions on the Sun. The chromospheric emission is highest in the network region at the boundary of supergranulation cells where the magnetic flux is highest. Thus for a time after the initial Einstein and IUE results the acoustic heating theory had fallen into disfavor.

The convective motions in the turbulent layers of a star are not only the source of an acoustic flux, but act together with the stellar rotation to generate and maintain a magnetic field which also transports mechanical energy from the convection zone into the outer layers of the star, either by direct magnetic field dissipation or by magneto-hydrodynamic (MHD) waves.

The magnetic heating mechanisms of chromospheres and coronae have been reviewed by many authors of which we cite only Kuperus et al. (1981) as well as Narain & Ulmschneider (1990) Ulmschneider, Priest & Rosner (1991) and most recently Narain & Ulmschneider (1995). These reviews show, that depending on the spectrum of the foot point motions of chromospheric and coronal field lines, a large zoo of different MHD wave (AC) and direct current (DC) heating mechanisms are at work simultaneously. Yet it is presently not possible to decide which mechanism, AC or DC, is dominant and where, although it appears that closed magnetic loops are primarily heated by DC mechanisms and open field regions by waves.

The acoustic and magnetic heating pictures do not contradict each other. In addition to the dominant magnetic heating mechanisms for the most active stars, it is necessary to also have heating mechanisms for nonmagnetic solar regions and for slowly rotating stars which presumably have very little magnetic flux at their surface. Such stars could be very old main sequence stars, which have suffered a large amount of rotational braking, and particularly late type giants, which because of angular momentum conservation and the radius increase due to the rise on the post main sequence evolutionary track, become very slow rotators.

In view of the variety of mechanisms capable to provide the heating, the problem is to determine which process or which combination of processes is responsible for the heating of chromosphere observed at a particular star.

1.3 Basal Fluxes

As the magnetic field of late-type stars is not a fossil field but is due to the dynamo mechanism, which arises from the joint action of stellar convection and rotation, a slower rotation rate leads to less magnetic flux and thus to less magnetic heating. This intimate relation between rotation and chromospheric as well as coronal emission, which was empirically well established (see e.g. Rutten 1986, Schrijver et al. 1989) and valid only for magnetic heating, was soon seen as the distinguishing indication of a magnetic heating mechanism. As stars have very different ages and thus rotation rates, the magnetic heating mechanisms show themselves also by the spread of chromospheric emission (henceforth called chromospheric emission spread) among essentially identical stars (of the same $T_{\rm eff}$ and log g (g = surface gravity)) but different rotation.

The favorization of the magnetic heating mechanism in the wake of the impressive Einstein and IUE results changed when e.g. Middelkoop (1982) showed that towards very late-type giants the chromospheric emission spread essentially decreases to zero and the chromospheric emission of these stars became similar for a given $T_{\rm eff}$. This indicated that a chromospheric heating mechanism was at work which acts independently from magnetic fields and which could be the acoustic heating mechanism. Recalling from above that acous-

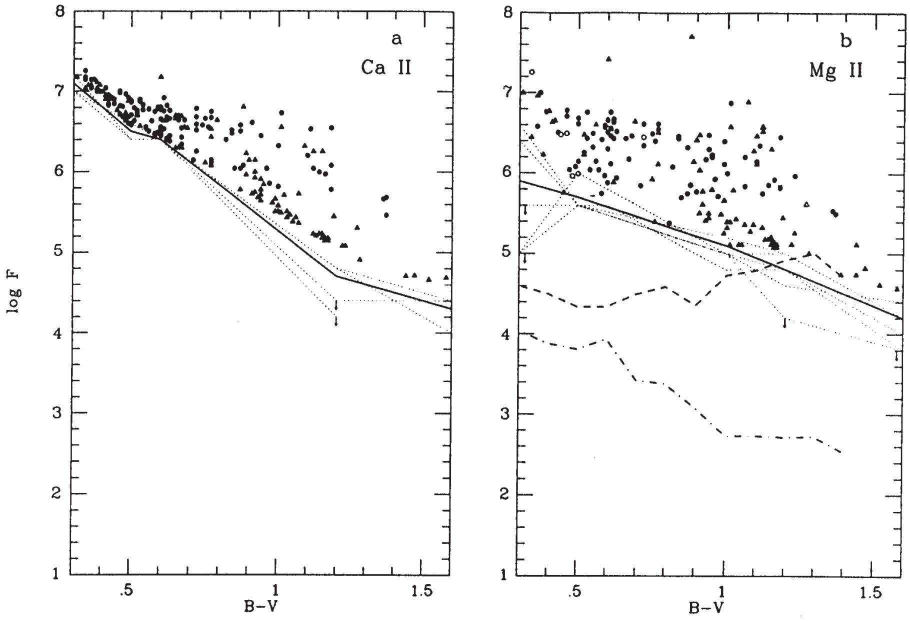

Figure 1.1: Radiative flux densities in the CaII H+K and the MgII h+k lines vs. color B-V (from Rutten et al., 1991). Dwarfs are shown by circles and giants by triangles. The line is the basal flux line derived by Schrijver (1987) by optimizing the relation between soft X-ray and CaII H+K excess fluxes. The dashed and dot-dashed lines in (b) are the detection limits of IUE for dwarfs and giants, respectively.

tic heating must inevitably occur and that shock formation is the unavoidable consequence of the strong density decrease (of seven orders of magnitude in case of the Sun) when the acoustic wave energy flux $F_{\rm M} = \rho v^2 c_S$ is conserved, it thus is only the question: where the acoustic heating shows itself, when compared to the more efficient magnetic mechanism.

Observing the chromospheric emission fluxes for stars with decreasing rotation rate, Oranje and Zwaan (1985) and particularly Schrijver (1987) discovered, (by separating the chromospheric emission into two components: a *nonmagnetic component* which is independent of rotation and only depends on $T_{\rm eff}$ and g, and a *magnetic component* which depends on rotation) upon subtraction of the nonmagnetic emission, the observed flux-flux relations of chromospheric and coronal emission were considerably improved. Those stars which rotate most slowly, show the lowest chromospheric emission, which henceforth were called basal flux stars (cf. Fig.(1.1)), should thus be the stars where the acoustic heating mechanism is dominant.

This joint heating picture, of a basic acoustic heating for all stars with an added magnetic heating which depends on rotation and is increasingly dominant the greater the magnetic flux is on the star, can also explain other observations. Due to the much larger convective velocities in F-stars as compared to M-stars it is expected that the acoustic flux generation peaks near F- stars (Bohn, 1984) and for these stars dominates the non-magnetic heating. This explains the small chromospheric emission spread found for these stars (Walter & Schrijver 1987). That picture is further supported by Simon & Landsman (1991) who analyze measurements of CII 1335 Å in several hundred low resolution IUE spectra. They find that the CII emission of main sequence stars reach a maximum near F0 and declines towards the late A stars. In addition, they observe that the emission for stars earlier than F5 is uncorrelated with rotation.

1.4 Acoustic Heating

The only realistic possibility to heat nonmagnetic regions of stars is either by flows or by acoustic as well as pulsational waves. While flows can occasionally increase the temperature by adiabatic compression they are not large and persistent enough to provide continuous heating. Pulsational waves do indeed heat the outer stellar layers as e.g. known from Mira stars. The only steady heating process for a non-magnetic solar type atmosphere thus is by acoustic waves.

Acoustic waves in principle could heat via viscous dissipation or thermal conduction. Taking typical values of the velocity v and temperature ΔT amplitudes of acoustic waves for the Sun ($v = c_S \sim 7$ km/s where c_S is the soundspeed), $\Delta T \sim 1000$ K) and length scales of the order of the scale height ($L = H \sim 200$ km) it can be shown that the viscous heating rate is $\eta v^2/L^2 \approx 5 \cdot 10^{-7}$ erg cm^{-3} s^{-1}, where η is the coefficient of viscosity, and that the thermal conductive heating rate is $\kappa \Delta T/L^2 \approx 3 \cdot 10^{-7}$ erg cm^{-3} s^{-1}, where κ is the coefficient of thermal conduction. Both values are several orders of magnitude below the heating rates of $1 \cdot 10^{-1}$ erg cm^{-3} s^{-1} inferred from the empirical solar models e.g of Vernazza et al. (1981). It thus becomes clear that acoustic waves heat only by shock dissipation, which is essentially viscous and thermal conductive heating, where the height scale L has been reduced to the size of the molecular mean free path.

It has long been thought that the height-dependence of the chromospheric emission could be a powerful means to identify the nature of the chromospheric heating mechanism. By including losses in the Fe II lines, Anderson & Athay (1989a, b), improving earlier empirical loss determinations by Vernazza et al. (1981), find that the solar chromospheric cooling flux is for many scale heights proportional to the gas pressure, that is, shows a constant heating rate (erg/g s) per gram. As shown by Ulmschneider (1990b) as well as by us (see below), this cooling flux can be balanced theoretically by a monochromatic limiting acoustic shock wave flux with a wave period of around $P = P_A/5$ ($\approx 40\ s$ for the Sun).

In addition the Anderson & Athay (1989a, b) chromospheric cooling fluxes are found to be consistent with the directly observed propagating acoustic wave flux (Endler & Deubner 1983, Deubner 1988), see also Fig. 9 of Ulmschneider (1990b). Deubner (1988) finds acoustic fluxes of $2.0 \cdot 10^7$, $1.2 \cdot 10^6$, $4.5 \cdot 10^5$ erg cm^{-2}s^{-1} at the heights 300, 800, 1500 km, respectively.

Finally the application of acoustic frequency spectra to chromospheric wave calculations by Sutmann & Ulmschneider (1994) shows that largely independent of the initial acoustic wave spectrum (Gaussian, Box, Exponential, Random) the overtaking property of shock waves leads to a heating behavior with height which is roughly equivalent to that of a monochromatic wave of period $P \sim P_A/5$.

1.5 This Work

In view of the observational facts and theoretical results mentioned above, it remains to be demonstrated, that with realistic acoustic wave fluxes computed in the stellar convection zones, the observed basal emission flux behavior can be reproduced. To theoretically simulate these emission fluxes and thus close the circle of arguments in favor of acoustic waves, is the main aim of the present work.

For a sample of late type stars of luminosity classes V and III radiation hydrodynamic wave calculations were performed. The fluxes and wavelengths of the acoustic waves sent into the atmospheric slabs were taken from theoretical calculations by Bohn (1981,1984). The resulting time dependent chromospheric models were analyzed and emission line fluxes calculated. Straight time means of the chromospheric models as well as of the emission fluxes are taken and compared with observational results.

Chapter 2 contains the basic equations and the numerical method used to solve the one-dimensional hydrodynamic equations in the Lagrangean frame, using the *method of characteristics.*

In Chapter 3 we develop a new and very fast method of solution for the radiative transfer equation in spectral lines especially suited to deal with the existence of radiating shock fronts and allowing for shocks as discontinuities. In addition the method to solve the radiative transfer equation for the continuum radiation is discussed.

The results of the modeling procedure for main sequence stars and giants are shown in Chapter 4. The properties of shock heating are examined and theoretical chromospheric emission fluxes are compared with the empirical basal emission fluxes.

Results obtained for M-dwarf stars are presented in Chapter 5. The newly introduced treatment of molecular opacities is described and the theoretical emission fluxes are compared with recent observational results.

Finally, Chapter 6 contains our conclusions and discusses possible future improvements of the modeling procedure.

Chapter 2

Hydrodynamics

In this Chapter we describe the basic equations of one-dimensional hydrodynamics and and the *numerical method of characteristics* employed to solve our problem of wave and shock propagation in a gravitationally stratified stellar atmosphere.

Among the different methods of computational fluid dynamics (CFD) the method of characteristics is rarely used. It is difficult to implement because one has to consider several special cases, as e.g. intersection of characteristics with the shock path or merging of shocks. In each of these special cases the computational procedure has to be altered.

As two separate grids have to be used to deal with normal grid points and the shock points, it is hardly suited to be vectorized or run on a parallel computer.

Moreover, if one tries to generalize the method of characteristics to two or even three dimensions, both the complexity and the variety of the special cases to be treated accurately explodes.

In contrary, a variety of other CFD methods exist which do not suffer from the apparent shortcomings of the method of characteristics. Usually, *artificial viscosity* (Von Neumann and Richtmyer, 1950) is used to smear out the shock discontinuity over several grid points. The numerical resolution at the shocks can be improved by using an *adaptive grid* (Dorfi and Drury, 1987) where grid-points can concentrate to the regions where the gradients of the flow variables are steep.

In these computational schemes, no special treatment of the shocks is needed, and the generalization to more dimensions is easily done. As these methods can be vectorized they can take full advantage of the architecture of modern supercomputers.

On the other hand, the method of characteristics has several advantages. In particular, it solves the *exact* equations of hydrodynamics for inviscid flows. The necessity of introducing artificial viscosity terms into the set of hydrodynamic equations changes their nature and one is not solving the original equations.

Second, the most important radiative effects take place at or in the vicinity of the shocks.

Smearing out the shocks by means of artificial viscosity has a severe effect on the solution of the radiative transfer equation, as the changes of the opacity and the source function then occur over a considerable optical distance. As the shocks are treated as discontinuities by the method of characteristics, the optical distance between front and back of the shock vanishes without causing spurious solutions.

Third, if one chooses a scheme with an adaptive grid, a large number of grid points is necessary if one tries to calculate situations with many shocks. The time required to solve the equation of transfer for all these points will grow enormously.

Fourth, to cover the same spatial range of an atmospheric model, the method of characteristics only needs a small number of mesh points. In addition as each shock only requires the solution of the radiative transfer at two additional points, the requirements of computational time are small compared to the other methods.

2.1 Basic Equations

We want to perform hydrodynamic wave calculations in the atmospheres of late type stars of spectral type F to M. To simplify our computations we restrict the problem to one dimension. This implies that our models are in some sense averaged over possible horizontal inhomogenities of the atmospheres like e.g. sunspots, network regions or granulation cells. Therefore all variables like density, pressure and temperature are only dependent on the height coordinate x and the time t. As the vertical extension of our stellar atmospheres is always small compared to the radius of the star it can be treated as plane-parallel and the gravitational acceleration g can be considered as constant. We assume an ideal gas with constant ratio of specific heats $\gamma = \frac{5}{3}$ and a mean molecular weight of $\mu = 1.3$ and neglect viscosity and heat transfer as well as ionization. Conservation of mass then leads to the equation of continuity,

$$\left(\frac{\partial \varrho}{\partial t}\right)_x + \left(\frac{\partial \varrho u}{\partial x}\right)_t = 0 \quad , \tag{2.1}$$

where ϱ (g cm^{-3}) is the mass density and u (cm sec^{-1}) is the gas velocity. The subscript x denotes that the derivatives are taken at a fixed point in space. x is the Euler height. Here and throughout the following chapters we will use cgs-units.

The equation of motion for a gas under the influence of gravity g can be written as

$$\left(\frac{\partial u}{\partial t}\right)_x + u\left(\frac{\partial u}{\partial x}\right)_t + \frac{1}{\varrho}\left(\frac{\partial p}{\partial x}\right)_t + g = 0 \tag{2.2}$$

with the gas pressure p (dyn cm^{-2}).

The energy equation is expressed in terms of the entropy conservation ,

$$\left(\frac{\partial s}{\partial t}\right)_x + u\left(\frac{\partial s}{\partial x}\right)_t = \left.\frac{\mathrm{d}s}{\mathrm{d}t}\right|_{\mathrm{ext}} . \tag{2.3}$$

where s (erg g^{-1} K^{-1}) is the entropy per gram and $\left.\frac{\mathrm{d}s}{\mathrm{d}t}\right|_{\mathrm{ext}}$ describes the rate of change of entropy by external sources. The only process, aside of that by shock heating, by which the entropy is changed in our calculations is radiation, and we have

$$\left.\frac{ds}{dt}\right|_{\mathrm{ext}} \equiv \left.\frac{ds}{dt}\right|_{\mathrm{rad}}$$

where the value of $D = \left.\frac{ds}{dt}\right|_{\mathrm{rad}}$ is obtained from the solution of the radiative transfer equation.

The calculations of one–dimensional hydrodynamics are greatly simplified by switching to the co-moving frame of individual gas elements, or Lagrangean frame. We define $a = x(t=0)$, the position of the gas element at time $t = 0$, as the Lagrangean height coordinate. a is independent of time (Courant, Friedrichs 1948). The Eulerian height coordinate x, the position of a given gas element at time t, can then be seen as a function of a and t: $x = x(a,t)$. The time derivative in the co-moving frame is defined as

$$\left(\frac{\partial}{\partial t}\right)_a = \left(\frac{\partial}{\partial t}\right)_x + u\left(\frac{\partial}{\partial x}\right)_t \tag{2.4}$$

and from mass conservation we get $\varrho \mathrm{d}x = \varrho_0 \mathrm{d}a$, where $\varrho_0(a)$ is the initial density distribution.

The continuity equation in the co-moving frame (2.1) now reads

$$\left(\frac{\partial \varrho}{\partial t}\right)_a + \frac{\varrho}{v}\left(\frac{\partial u}{\partial a}\right)_t = 0 \quad , \tag{2.5}$$

with the dimensionless relative volume (Hoskin, 1964)

$$v \equiv \left(\frac{\partial x}{\partial a}\right)_t = \frac{\varrho_0}{\varrho} \quad .$$

The equation of motion (2.2) is written as

$$\left(\frac{\partial u}{\partial t}\right)_a + \frac{1}{\varrho_0}\left(\frac{\partial p}{\partial a}\right)_t + g = 0 \tag{2.6}$$

and for the energy equation (2.3) we obtain

$$\left(\frac{\partial s}{\partial t}\right)_a = \left.\frac{\mathrm{d}s}{\mathrm{d}t}\right|_{\mathrm{rad}} \quad . \tag{2.7}$$

The equation of state for an ideal gas

$$p = \varrho \frac{\mathcal{R}T}{\mu} \tag{2.8}$$

connects the pressure p with the density ϱ and the temperature T and from the first and second law of thermodynamics we get

$$T\ \mathrm{d}s = \frac{1}{\gamma - 1}\frac{\mathcal{R}}{\mu}\mathrm{d}T + p\ \mathrm{d}\left(\frac{1}{\varrho}\right) \tag{2.9}$$

as relation between the temperature and the entropy s. The gas constant is $\mathcal{R} = 8.3144 \times 10^7$ erg K^{-1} mol^{-1}.

Following Ulmschneider et al. (1977) we use the entropy s and the sound velocity

$$c_{\mathrm{s}}{}^2 = \gamma \frac{\mathcal{R}T}{\mu} \tag{2.10}$$

as thermodynamic variables. By eliminating ϱ and p in favor of c and s we finally get a quasi-linear system of hyperbolic partial differential equations

$$\begin{aligned} \frac{\partial u}{\partial t} + \frac{2}{(\gamma-1)} \frac{c}{v} \frac{\partial c}{\partial a} - \frac{\mu c}{\gamma R} \frac{c}{v} \frac{\partial s}{\partial a} + g &= 0 \\ \frac{2}{(\gamma-1)} \frac{\partial c}{\partial t} - \frac{\mu c}{R} \frac{\partial s}{\partial t} + \frac{c}{v} \frac{\partial u}{\partial a} &= 0 \\ \frac{\partial s}{\partial t} - \left. \frac{\mathrm{d}s}{\mathrm{d}t} \right|_{\mathrm{rad}} &= 0 \end{aligned} \tag{2.11}$$

for our set (u, c, s) of independent variables.

2.2 Characteristics

We can rewrite the system of equations (2.11) in a more compact form by introducing

$$\mathbf{f} = \begin{pmatrix} u \\ c \\ s \end{pmatrix} \tag{2.12}$$

as the vector of the hydrodynamic variables. Clearly $\mathbf{f}$ depends on the Lagrangean height and time: $\mathbf{f} = \mathbf{f}(a, t)$. The partial derivatives of c, u, and s, with respect to time can be written

$$\frac{\partial \mathbf{f}}{\partial t} \equiv \begin{pmatrix} \frac{\partial u}{\partial t} \\ \frac{\partial c}{\partial t} \\ \frac{\partial s}{\partial t} \end{pmatrix} \tag{2.13}$$

and the derivatives with respect to a are

$$\frac{\partial \mathbf{f}}{\partial a} \equiv \begin{pmatrix} \frac{\partial u}{\partial a} \\ \frac{\partial c}{\partial a} \\ \frac{\partial s}{\partial a} \end{pmatrix} \quad . \tag{2.14}$$

Using equations (2.13) and (2.14) we obtain from (2.11)

$$\mathbf{A} \frac{\partial \mathbf{f}}{\partial \mathbf{t}} + \mathbf{B} \frac{\partial \mathbf{f}}{\partial \mathbf{a}} + \mathbf{c} = 0 \tag{2.15}$$

where the coefficient matrices are

$$\mathbf{A} = \begin{pmatrix} 1 & 0 & 0 \\ 0 & \frac{2}{\gamma-1} & -\frac{\mu c}{R} \\ 0 & 0 & 1 \end{pmatrix} \tag{2.16}$$

and

$$\mathbf{B} = \begin{pmatrix} 0 & \frac{2}{\gamma-1}\frac{c}{v} & -\frac{\mu c}{\gamma R}\frac{c}{v} \\ \frac{c}{v} & 0 & 0 \\ 0 & 0 & 0 \end{pmatrix} \quad . \tag{2.17}$$

The vector $\mathbf{c}$ contains the external influences of gravity and radiation losses, i.e.

$$\mathbf{c} = \begin{pmatrix} g \\ 0 \\ -\left.\frac{\mathrm{d}s}{\mathrm{d}t}\right|_{\mathrm{rad}} \end{pmatrix} \quad . \tag{2.18}$$

Equation (2.15) has the general form of a quasi-linear system of first order differential equations. It is linear in the first derivatives of the dependent variables (the elements of $\mathbf{f}$), and the coefficients in $\mathbf{A}$ and $\mathbf{B}$ are functions of the dependent variables.

Each of the equations in (2.15) has different combinations of the derivatives for each of the $f_j, j = 1, \ldots, 3$, it therefore couples derivatives in different directions of the (a, t)-plane. We now seek combinations of the equations (2.15) that the resulting equation contains derivatives in one direction only (Courant,Friedrichs 1948). These directions define the *characteristic curves* or *characteristics*. Following Whitham (1974) we consider the linear combination

$$\mathbf{l} \cdot \left(\mathbf{A}\frac{\partial \mathbf{f}}{\partial \mathbf{t}} + \mathbf{B}\frac{\partial \mathbf{f}}{\partial \mathbf{a}} \right) + \mathbf{l} \cdot \mathbf{c} = 0 \tag{2.19}$$

with a vector $\mathbf{l}$ which in general may be a function of a and t as well as of the f_j. If $\mathbf{l}$ can be chosen such as (2.19) takes the form

$$\mathbf{m} \cdot \left(\beta\frac{\partial \mathbf{f}}{\partial \mathbf{t}} + \alpha\frac{\partial \mathbf{f}}{\partial \mathbf{a}} \right) + \mathbf{l} \cdot \mathbf{c} = 0 \tag{2.20}$$

with some arbitrary vector $\mathbf{m}$ one has a single equation which provides a relation between the directional derivatives of all the f_j in the direction (α, β) of the (a, t)-plane. Such a transformation is possible if

$$\mathbf{l} \cdot \mathbf{A} = \mathbf{m} \cdot \beta \quad \text{and} \quad \mathbf{l} \cdot \mathbf{B} = \mathbf{m} \cdot \alpha \quad . \tag{2.21}$$

Now let $a = a(\xi)$, $t = t(\xi)$ be a parametrical representation of a curve in the (a, t)-plane defined by the vector field of (α, β). The total derivative of $\mathbf{f}$ along that curve is

$$\frac{\mathrm{d}\mathbf{f}}{\mathrm{d}\xi} = \frac{\mathrm{d}t}{\mathrm{d}\xi}\frac{\partial \mathbf{f}}{\partial \mathbf{t}} + \frac{\mathrm{d}a}{\mathrm{d}\xi}\frac{\partial \mathbf{f}}{\partial \mathbf{a}} \quad . \tag{2.22}$$

In (2.21) we can choose, without loss of generality, the direction (α, β) as $(\frac{d\,a}{d\,\xi}, \frac{d\,t}{d\,\xi})$, and together with (2.22) we finally obtain

$$\mathbf{m} \cdot \frac{\mathrm{d}\mathbf{f}}{\mathrm{d}\xi} + \mathbf{l} \cdot \mathbf{c} = 0 \tag{2.23}$$

as a system of ordinary differential equations along the characteristics. Equation (2.23) is said to be in characteristic form.

After eliminating $\mathbf{m}$ from (2.21) the requirement on the directions for a transformation of (2.15) into characteristic form is written as

$$\mathbf{l}\left(\mathbf{A}\frac{\mathrm{d}a}{\mathrm{d}\xi} + \mathbf{B}\frac{\mathrm{d}t}{\mathrm{d}\xi}\right) = 0 \quad . \tag{2.24}$$

This equation only has a nontrivial solution if

$$\det\left(\mathbf{A}\frac{\mathrm{d}a}{\mathrm{d}\xi} + \mathbf{B}\frac{\mathrm{d}t}{\mathrm{d}\xi}\right) = 0 \tag{2.25}$$

and using $\mathbf{A}$ and $\mathbf{B}$ from (2.16) and (2.17) this leads to

$$\frac{2}{\gamma-1}\left(\frac{\mathrm{d}\ a}{\mathrm{d}\ \xi}\right)^2 - \frac{2}{\gamma-1}\left(\frac{c}{v}\right)^2\left(\frac{\mathrm{d}\ t}{\mathrm{d}\ \xi}\right)^2\left(\frac{\mathrm{d}\ a}{\mathrm{d}\ \xi}\right) = 0 \quad . \tag{2.26}$$

In our case the matrix $\mathbf{B}$ is singular, det $\mathbf{B} = 0$ and $\left(\frac{d\ a}{d\ \xi}\right) = 0$ gives a solution of (2.26) showing that the t-direction itself is a characteristic. On the other hand, as $\mathbf{A}$ is not singular and we have $\left(\frac{\mathrm{d}\ t}{\mathrm{d}\ \xi}\right) \neq 0$, the a-direction is not a characteristic. It is therefore possible to use the time t as the curve parameter ξ and we get

$$\left(\frac{\mathrm{d}\ a}{\mathrm{d}\ \xi}\right) = \left(\frac{\mathrm{d}\ a}{\mathrm{d}\ t}\right) \quad \text{and} \quad \left(\frac{\mathrm{d}\ t}{\mathrm{d}\ \xi}\right) = 1 \quad . \tag{2.27}$$

Now the solution of (2.26) gives the characteristic directions as

$$\frac{\mathrm{d}\ a}{\mathrm{d}\ t} = 0 \tag{2.28}$$

which is the path of the fluid element, and

$$\frac{\mathrm{d}\ a}{\mathrm{d}\ t} = \pm\frac{c}{v} \tag{2.29}$$

for the two remaining characteristics, respectively.

As each characteristic equation (2.23) gives only one relation between the derivative of $\mathbf{f}$ along one single characteristic curve, the complete set of characteristic equations along the three characteristics can be found by using three independent vectors $\mathbf{l}^{(k)}, k = 1, \ldots, 3$ in equation (2.19). These vectors are

$$\mathbf{l}^{(1)} = \begin{pmatrix} 1 \\ 1 \\ 0 \end{pmatrix} \quad , \quad \mathbf{l}^{(2)} = \begin{pmatrix} 1 \\ -1 \\ 0 \end{pmatrix} \quad , \quad \mathbf{l}^{(3)} = \begin{pmatrix} 0 \\ 0 \\ 1 \end{pmatrix} \quad , \tag{2.30}$$

and the corresponding characteristic equations are (Ulmschneider et al. 1977)

$$\mathrm{d}u + \frac{2}{\gamma-1}\mathrm{d}c - \frac{\mu c}{\gamma R}\left(\mathrm{d}s + (\gamma-1)\left.\frac{\mathrm{d}s}{\mathrm{d}t}\right|_{\mathrm{rad}}\mathrm{d}t\right) + g\ \mathrm{d}t \ = \ 0 \tag{2.31}$$

along the C^+-characteristic, $\left(\frac{\mathrm{d}a}{\mathrm{d}t} = \frac{c}{v}\right)$,

$$\mathrm{d}u - \frac{2}{\gamma - 1}\mathrm{d}c + \frac{\mu c}{\gamma R}\left(\mathrm{d}s + (\gamma - 1)\left.\frac{\mathrm{d}s}{\mathrm{d}t}\right|_{\mathrm{rad}}\mathrm{d}t\right) + g\ \mathrm{d}t \ = \ 0 \tag{2.32}$$

along the C^--characteristic, $\left(\frac{\mathrm{d}a}{\mathrm{d}t} = -\frac{c}{v}\right)$ and

$$\mathrm{d}s = \left.\frac{\mathrm{d}s}{\mathrm{d}t}\right|_{\mathrm{rad}}\mathrm{d}t \tag{2.33}$$

along the C^0-characteristic with (a=const.).

2.3 The Numerical Method of Characteristics

To solve the discretized form of the characteristic equations (2.31) – (2.33) we apply the *method of characteristics with fixed time intervals* (Lister 1960, Hoskin 1964, Ulmschneider et al. 1977). The atmospheric slab is divided into $N-1$ discrete height intervals $(\Delta a)_i = a_{i+1} - a_i, i = 1, \ldots, N-1$ with the grid points $a_j, j = 1, \ldots, N$.

We start our calculations from an initial state at time $t = 0$, for which u, c and s as well as the radiative damping $D \equiv \left.\frac{\mathrm{d}s}{\mathrm{d}t}\right|_{\mathrm{rad}}$ is given. The initial atmosphere satisfies the conditions of radiative and hydrostatic equilibrium and is at rest. We thus have $D = 0$ and $u = 0$ for each grid point.

In addition we need to know the slope of the $C^{\pm}$-characteristics which can be calculated as (Ulmschneider et al. 1977)

$$y = \left.\frac{\mathrm{d}a}{\mathrm{d}t}\right|_{C^{\pm}} = \pm\frac{c}{v} = \pm\frac{c^4}{{c_0}^3}e^{-\frac{S-S_0}{R}\mu} \tag{2.34}$$

using the sound speed c_0 and the entropy S_0 of an arbitrary but fixed reference state.

With all variables given at each grid point at a given time t the value of the entropy s at a later time $t+\Delta t$ at an interior point (that is: far from the boundaries or shocks) is computed by integrating (2.33) along the fluid path using the trapezoidal rule under the assumption that D is known. To calculate the remaining unknowns the values at the intersection points of the characteristics with the old time level (see Fig.(2.1)) are interpolated between the values at A, B, and C. We then integrate (2.31) and (2.32) along the $C^{\pm}$-characteristics in order to get u and c at P. This procedure has to be repeated until all variables have converged, because the slopes at P and subsequently the positions of R and S are not known in advance. For an interior point the three unknowns are specified by the three characteristics through this point.

At the boundaries only two of the three characteristics lie inside the computational domain. Thus one unknown has to be specified by the determination of a boundary condition. This specification is completely arbitrary. However, as our computational domain is a slab

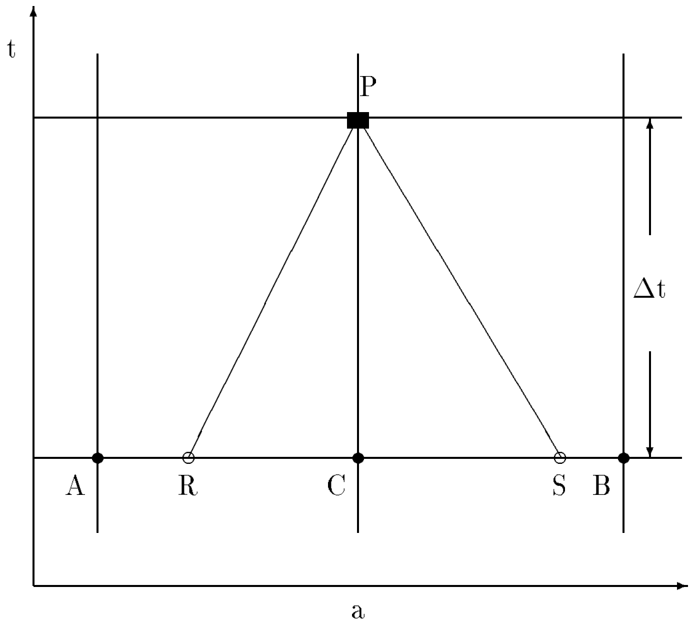

Figure 2.1: Calculation for an interior point. RP and SP are the characteristics, filled circles denote the points where the solution is known, open circles show the interpolated values.

of the atmosphere which is cut out of a more extended atmosphere where the physical state is not drastically different, the boundary conditions are chosen to be consistent with the greater surroundings.

At the lower boundary a mass element serves as a piston whose motions give rise to the acoustic waves. Here the boundary condition is given by specification of the piston velocity. The velocity of the piston as a function of time can either be purely sinusoidal for a monochromatic acoustic wave, or follow the conditions of the acoustic spectrum used for the calculation, and is given at each time step.

The entropy $s_{\rm P}$ at the lower boundary is calculated in the same way as for an interior point because the C^0-characteristic is present. Only the calculation of $c_{\rm P}$ needs an iterative procedure and is done by integrating (2.32) along the C^--characteristic which is completely situated inside the computational domain.

At the upper boundary only the C^0 and the C^+-characteristic are inside the computational domain. Unlike the situation at the lower boundary we now cannot prescribe the velocity $u_{\rm P}$ by means of a time dependent function, instead it must follow consistently from the gas flow. As said before, our model covers only a part of the stellar envelope. In reality a wave would cross the chromosphere and transition layer and run into the corona. As our models usually end at such heights where the transition layer would form, we must allow the upward traveling disturbances to leave the computational domain. The choice of the boundary condition should therefore not result in unphysical behavior like reflection of the waves. Following Leibacher (1971) and Stein (1972), Ulmschneider (1977) chose the *trans-*

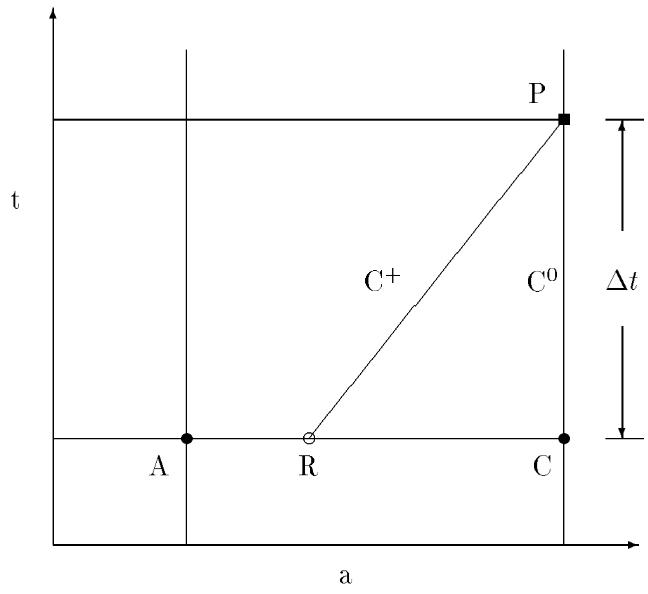

Figure 2.2: Calculation at the upper boundary. Notation as in Fig.(2.1).

mitting boundary condition where the velocity at the boundary point u_P is chosen as the velocity at the foot-point of the C^+-characteristic through P. Referring to Figure 2.2 this is

$$u_\mathrm{P} = u_\mathrm{R} \quad . \tag{2.35}$$

Again, s_P is determined as for an interior point and the sound speed c_P follows from the integration of (2.31) along the C^+-characteristic.

The choice of (2.35) as the upper boundary condition is suggested by the case of sound waves and simple waves in non-stratified media where (2.35) holds exactly. But we are dealing here with shocks and gravitationally stratified atmospheres. Therefore, equation (2.35) is only an approximation to an exact boundary condition needed to ensure complete transmission of disturbances of arbitrary strength through the upper boundary.

In some cases, especially for strong shocks, the boundary condition (2.35) leads to reflection of disturbances which then move downwards. The density increases with depth and as the reflected waves travel downwards, their amplitude decreases and becomes small.

Yet, a more severe problem is caused by the momentum transfer to the boundary point when partial reflection occurs. In some cases this leads to an expansion of the atmosphere in terms of the Eulerian height.

By slightly modifying the boundary condition this effect can be reduced. We introduce two factors f^+ and f^- and write the modified boundary condition as

$$u_{\mathrm{P}} = u_{\mathrm{R}} \cdot \begin{cases} f^+ , & u_{\mathrm{R}} \geq 0 \\ f^- , & u_{\mathrm{R}} < 0 \end{cases} \tag{2.36}$$

with $f^+ < 1$ and $f^- > 1$.

The idea behind this choice is that the gas element loses energy if it moves upward ($u > 0$) and its velocity is reduced by f^+ and for the downward motion ($u < 0$) the gain of gravitational energy leads to a higher velocity by the factor of f^-.

Appropriate values for f^+ and f^- have to be found by experience requiring that the unphysical expansion of the atmosphere due to the reflections is avoided. The thermal energy deposited in the outer layers of the atmosphere by the shocks also causes a slight expansion of the atmosphere. The discrimination between both cases of expansion is possible by noting that the unphysical momentum transfer due to partial shock reflection results in an extreme expansion of only the topmost height interval whereas in the other case the upper parts of the atmosphere expand in a more uniform way.

For satisfactory results f^+ and f^- differ only slightly from unity. For our calculations we choose $f^+ = 0.999$ and $f^- = 1.001$.

2.4 Shocks

The method of characteristics treats shocks as real discontinuities which separate the region in front of the shock (denoted as region 1) from the post shock region (denoted as region 2). For that reason, the differential form of the conservation laws for mass, linear momentum and energy, equations (2.1)–(2.3), cannot be applied. We have to use the Hugoniot relations instead, which describe the conservation of mass, momentum, and energy across the shock front.

With the velocity u_s of the shock front these relations are (Landau,Lifshitz 1959)

$$\varrho_1(u_1 - u_s) = \varrho_2(u_2 - u_s) \tag{2.37}$$

for the conservation of mass,

$$p_1 + \varrho_1(u_1 - u_s)^2 = p_2 + \varrho_2(u_2 - u_s)^2 \tag{2.38}$$

for momentum conservation, and the energy equation is written as

$$\frac{1}{2}\varrho_1(u_1 - u_s)^2 + H_1 = \frac{1}{2}\varrho_2(u_2 - u_s)^2 + H_2 \quad , \tag{2.39}$$

where we introduced the enthalpies per gram H_1 and H_2 at the shock points in region 1 and 2, respectively. Without ionization we have for the enthalpy

$$H = \frac{\gamma}{\gamma - 1}\frac{\mathcal{R}T}{\mu} \quad . \tag{2.40}$$

For a given shock jump of the velocity $u_2 - u_1$ and the known front shock state, the Hugoniot relations (2.37) – (2.39) can now be used to determine the velocity of the shock (Ulmschneider et al. 1977),

$$u_s = u_1 + \frac{\gamma + 1}{4}(u_2 - u_1) + \sqrt{\left(\frac{\gamma + 1}{4}\right)^2 (u_2 - u_1)^2 + c_1^2} \tag{2.41}$$

as well as the sound speed c_2 and the entropy s_2 in the post shock region. To solve the characteristic equations for the shock, the seven unknowns u_1, c_1, s_1, u_2, c_2, s_2, and u_s must be determined. For the shock point in region 1, all three characteristics are available and the unknowns are computed in the same way as for an interior grid point. The only difference is, that because the shock moves along the regular grid, the values at the foot-points of all of the characteristics must be found by interpolation.

In the post shock region one only has the C^+ characteristic, and equation (2.31) is integrated along that characteristic to get u_2. Given the values of the hydrodynamic variables so far, u_s follows from (2.41) and we use (Ulmschneider et al. 1977)

$$c_2 = \sqrt{\frac{\gamma - 1}{2}(V_1^2 - V_2^2) + c_1^2} \tag{2.42}$$

and

$$s_2 = s_1 + \frac{2}{\gamma - 1}\frac{\mathcal{R}}{\mu}\ln\left(\frac{c_2}{c_1}\right) - \frac{\mathcal{R}}{\mu}\ln\left(\frac{V_2}{V_1}\right) \quad , \tag{2.43}$$

where $V_1 \equiv u_1 - u_\mathrm{s}$ and $V_2 \equiv u_2 - u_\mathrm{s}$, to complete the solution. In summary, for the seven unknowns at the shock in the new time level, we have four relations along characteristics and three Hugoniot relations.

During the calculations, the amplitudes of the acoustic waves steepen as they propagate into atmospheric regions of decreasing density. The development of an acoustic wave into a shock is determined by the intersection of two or more characteristics of the same family (in our case: the C^+ characteristics). At that point, the solutions of the characteristic equations would be multi-valued, and to have a physically meaningful single valued solution, a shock must be inserted. In our calculations, the shock is represented by two additional points with infinitesimally small separation, on each side of the shock discontinuity. The shock can move freely across the fixed spatial grid of regular mesh points until it is transmitted at the top boundary.

Chapter 3

Radiative Transfer

The solution of the radiative transfer equation (RTE) plays an essential role for the computation of stellar atmospheres. The energy transfer by radiation couples different atmospheric regions with different physical conditions. It determines entirely the structure of the undisturbed atmosphere and influences the propagation of waves and shocks by means of the energy exchange between different parts of the disturbed atmosphere.

In addition the shape and the variability of spectral lines provide the observer with information on the physical conditions of the line forming regions.

In our calculations we consider continuous radiation as well as line radiation. For solar-type stars the photospheric radiation is dominated by emission and absorption due to the negative hydrogen ion H^-. Waves entering the photosphere from below will propagate upwards through the regions with dominant H^- radiation and lose part of their energy.

In the overlying chromospheric regions the bulk of radiative transfer takes place in a few strong spectral lines. Most important are the MgII h+k doublet and the CaII H+K doublet. Due to the high element abundance these lines are especially important as they dominate the energy transfer of the lower chromosphere and are the most prominent chromospheric diagnostic lines.

Our model atmospheres are traversed by acoustic waves and shocks leading to a highly inhomogeneous dependence of the temperature, the density, and the opacity with height. We thus need methods capable to solve the RTE under these conditions with sufficient accuracy. In addition these methods must be able to deal with internal boundaries, like shocks, and the related large gradients in the flow variables.

The wave motions lead to changes of sign in the gas velocity leading to similar changes in the direction of the Doppler shift of the line profiles. We are therefore forced to solve the RTE in the observer's frame.

The solution of the hydrodynamic equations requires the solution of the RTE for each height grid point and at each timestep. This sets up the need for extremely fast, stable, and reliable methods of solution.

In this chapter we discuss the methods of solution applied to the problems of continuous and line radiation transfer.

3.1 Transfer Equation for Spectral Lines

Consider a plane parallel atmosphere traversed by a vertically propagating acoustic wave which causes fluctuations of the temperature T, the density ϱ, and the velocity u. The equation of radiative transfer (e.g., Mihalas, 1978 p. 449) is then given by

$$\mu \frac{\partial I_{\nu\mu}(z)}{\partial z} = \eta_{\nu\mu}(z) - \chi_{\nu\mu}(z) I_{\nu\mu}(z) \quad . \tag{3.1}$$

Here z is the geometrical height, $I_{\nu\mu}$ the specific monochromatic intensity in (erg cm^{-2} sec^{-1} sr^{-1} Hz^{-1}) of the radiation field, μ the angle cosine between the direction of the photons and the outward normal, and ν the frequency. The total emissivity is given by $\eta_{\nu\mu}$ whereas $\chi_{\nu\mu}$ describes the total extinction. We consider here the case of a two level atom with background radiation in LTE. The line emission and absorption profiles are calculated assuming complete redistribution (CRD). Then the emissivity and the extinction coefficient can be written as

$$\eta_{\nu\mu}(z) = \eta_{\mathrm{C}}(z) + \eta_{\mathrm{L}}(z) \varphi_{\nu\mu}(z) \tag{3.2}$$

and

$$\chi_{\nu\mu}(z) = \chi_{\mathrm{C}}(z) + \chi_{\mathrm{L}}(z) \varphi_{\nu\mu}(z) \quad , \tag{3.3}$$

respectively. Here, χ_{L} and χ_{C} are frequency-independent line and continuum extinction, η_{L} and η_{C} are the line and continuum emissivities and $\varphi_{\nu\mu}$ is the absorption profile, given by the Voigt function

$$\varphi_{\nu\mu} = \frac{H(a,v)}{\sqrt{\pi}\Delta\nu_{\mathrm{D}}} \quad , \tag{3.4}$$

where

$$a = \frac{\Gamma}{4\pi\Delta\nu_{\mathrm{D}}} \tag{3.5}$$

is the damping parameter with the damping width Γ, and

$$v = \frac{\nu - \nu_0 \left(1 - \mu \; u(z)/c_{\mathrm{L}}\right)}{\Delta\nu_{\mathrm{D}}} \tag{3.6}$$

gives the frequency displacement from the line center in units of the thermal Doppler width $\Delta\nu_D$. Here u is the gas velocity, and the speed of light is c_L. The total damping width Γ consists of two contributions. The radiation damping width is given by the Einstein coefficient of spontaneous emission, $\Gamma_{\mathrm{rad}} = A_{21}$, and the collisional damping is given as

$$\Gamma_{\mathrm{col}} = \Gamma_{\mathrm{VdW}} \left(\frac{T}{5000\ \mathrm{K}}\right)^{0.3} \cdot n_{\mathrm{H}} \quad . \tag{3.7}$$

Here $\Gamma_{\rm VdW}$ is the Van der Waals collisional width, and the number density of hydrogen is $n_{\rm H}$. The total damping width is then obtained as $\Gamma = \Gamma_{\rm rad} + \Gamma_{\rm col}$.

The absorption profile satisfies the normalization condition

$$\int_{-1}^{1}\int_{-\infty}^{\infty} \varphi_{\nu\mu}{\rm d}\nu{\rm d}\mu = 1. \tag{3.8}$$

The background source function is defined as

$$S_{\rm C} = \frac{\eta_{\rm C}}{\chi_{\rm C}} \tag{3.9}$$

and similarly the line source function as

$$S_{\rm L} = \frac{\eta_{\rm L}}{\chi_{\rm L}} \quad . \tag{3.10}$$

The line source function S_{rmL} for the two-level approximation assuming CRD is given by

$$S_{\rm L}(z) = [1-\epsilon(z)]\,\overline{J}(z) + \epsilon(z)B(z) \quad , \tag{3.11}$$

where we introduce

$$\epsilon(z) = \frac{\epsilon'(z)}{1+\epsilon'(z)} \tag{3.12}$$

with the photon destruction probability (Mihalas 1978, p. 337)

$$\epsilon'(z) = \frac{n_e(z)\Omega_{21}(z)}{A_{21}}\left(1-{\rm e}^{-h\nu/kT(z)}\right) \quad . \tag{3.13}$$

Ω_{21} denotes the rate for collisional deexcitation. The line profile averaged mean intensity $\overline{J}(z)$ is given by

$$\overline{J}(z) = \frac{1}{2}\int_{-\infty}^{\infty}{\rm d}\nu\int_{-1}^{1}{\rm d}\mu\;\varphi_{\nu\mu}(z)I_{\nu\mu}(z). \tag{3.14}$$

If we assume that the background source function is Planckian and constant over the line center, $S_{\rm C}(z) = B(T(z))$, we can write the total source function, $S_{\nu\mu}(z)$, as

$$S_{\nu\mu}(z) = \frac{\varphi_{\nu\mu}(z)S_{\rm L}(z) + r(z)B(z)}{\varphi_{\nu\mu}(z) + r(z)}, \tag{3.15}$$

with the residual strength of the continuum, $r(z)$, given by $r(z) = \chi_{\rm C}(z)/\chi_{\rm L}(z)$. Following Mihalas (1978) we define

$$\xi_{\nu\mu}(z) = \frac{\epsilon(z)\varphi_{\nu\mu}(z) + r(z)}{\varphi_{\nu\mu}(z) + r(z)} \tag{3.16}$$

and rewrite Eq. (3.15) as

$$S_{\nu\mu}(z) = (1-\xi_{\nu\mu}(z))\overline{J}(z) + \xi_{\nu\mu}(z)B(z), \tag{3.17}$$

which has the same form as Eq. (3.12).

Introducing the optical depth along a ray, specified by $(\nu\mu)$,

$$\tau_{\nu\mu}(z) = \frac{1}{\mu}\int_z^{z_{\max}} \chi_{\nu\mu}(z)\mathrm{d}z \tag{3.18}$$

we can write the transfer equation for one ray as

$$\frac{\partial I_{\nu\mu}(z)}{\partial \tau_{\nu\mu}(z)} = [I_{\nu\mu}(z) - S_{\nu\mu}(z)] \quad . \tag{3.19}$$

For a given source function $S_{\nu\mu}$ Eq. (3.19) is readily integrated to obtain the specific intensities for each angle, frequency and depth point. A formal solution, i.e., the calculation of $\overline{J}$ for known source function, is then completed by using Eq. (3.14).

3.2 Operator Splitting Method for Atmospheres with Shocks

Formally, we write the sequence of operations needed to compute $\overline{J}$ for a given source function as

$$\overline{J} = \mathbf{\Lambda}[S], \tag{3.20}$$

the so-called "Λ-operation". The operator acting on the source function to obtain $\overline{J}$, is called "Λ-operator". Combining Eqs.(3.20) and (3.17) we find

$$S_{\nu\mu}(z) = (1 - \xi_{\nu\mu}(z))\mathbf{\Lambda}[S_{\nu\mu}] + \xi_{\nu\mu}(z)B(z). \tag{3.21}$$

The problem is to solve Eq. (3.21) for a given model atmosphere with prescribed boundary conditions for the specific intensities. In the following we drop the subscripts to simplify the notation.

The ordinary Λ-iteration proceeds by calculating the (n+1)-th iterate of the source function, S^{n+1}, from the n-th by means of the expression

$$S^{n+1} = (1-\xi)\mathbf{\Lambda}[S^n] + \xi B. \tag{3.22}$$

The well known drawback of this iteration scheme, i.e., slow convergence, can be avoided by splitting the Λ-operator according to

$$\mathbf{\Lambda} = \mathbf{\Lambda}^* + (\mathbf{\Lambda} - \mathbf{\Lambda}^*), \tag{3.23}$$

with an appropriately chosen "approximate Λ-operator", $\mathbf{\Lambda}^*$. Using Eq. (3.23), the iteration scheme for the operator splitting method then reads

$$S^{n+1} = (1-\xi)\mathbf{\Lambda}^*[S^{n+1}] + (1-\xi)(\mathbf{\Lambda} - \mathbf{\Lambda}^*)[S^n] + \xi B, \tag{3.24}$$

or, with the formal solution of the n-th iterate, $\overline{J}^{\rm FS} = \mathbf{\Lambda}[S^n]$ and $S^{\rm FS} = (1-\xi)\overline{J}^{\rm FS} + \xi B$,

$$\begin{aligned} S^{n+1} - S^n &= [1-(1-\xi)\mathbf{\Lambda}^*]^{-1}\left[S^{\rm FS} - S^n\right] \\ &\equiv \mathbf{A}^{-1}\left[S^{\rm FS} - S^n\right]. \end{aligned} \tag{3.25}$$

Equation (3.25) shows that, for robust convergence, $\mathbf{\Lambda}^*$ should contain the essential physics of the line transfer problem and, in order to save computer time, should be easy to compute and to invert.

Starting with a first guess for the source function, S^0, the transfer equation Eq. (3.19) is integrated to compute a formal solution using Eqs. (3.14) and (3.17). We then solve Eq. (3.25) *directly* and obtain an improved value for S. This new source function is subsequently used to calculate a new formal solution. $\mathbf{\Lambda}^*$ and $\mathbf{A}^{-1}$ can be precomputed[1]and reused, thus greatly reducing the number of operations required for a full iteration step.

Note that the frequency and angle dependence of the total source function $S_{\nu\mu}$ enters the problem only via $\xi_{\nu\mu}$, Eq.(3.17). Therefore, we can solve for the frequency independent line source function,

$$S_{\rm L}^{n+1} - S_{\rm L}^n = [1-(1-\epsilon)\mathbf{\Lambda}^*]^{-1}\left[S_{\rm L}^{\rm FS} - S_{\rm L}^n\right]. \tag{3.26}$$

instead of Eq. (3.25). The formal solution for the line source function is given by

$$S_{\rm L}^{\rm FS} = (1-\epsilon)\overline{J}^{\rm FS} + \epsilon B \tag{3.27}$$

where $\overline{J}^{\rm FS}$ is obtained from the total source function, Eq. (3.15), as

$$\overline{J}^{\rm FS} = \mathbf{\Lambda}[S_{\nu\mu}^n]. \tag{3.28}$$

Formal solution

We consider an atmospheric slab with D grid-points. The depth dependent variables S and J are then vectors whose components are the values taken at the grid-points. We use N discrete frequency points $\nu_n, n = 1,\ldots,N$ in the range $-\infty,\ldots,\infty$, covering the width of the line and M discrete angle points $\mu_m, m = 1,\ldots,M$ in the range $\mu = 0,\ldots,1$. We put the frequency and angle points together in rays labeled by (ν_n,μ_m) and define a ray index as $r = m + (n-1)M$. In this case, the discrete representation of the $\mathbf{\Lambda}$-operator is a D$\times$D-matrix, and Eq. (18) becomes

$$\overline{J}_d = \sum_{d'} \Lambda_{dd'} S_{d'} . \tag{3.29}$$

[1]it is preferable to use LU decomposition for the solution of Eq.(3.25)

The elements of the k-th column, Λ_{dk}, of the exact $\mathbf{\Lambda}$-matrix are the elements $\overline{J}_d$ of a formal solution obtained using a "pulse" like source function,

$$S_k = 1 \, , S_{d \neq k} = 0 \, , \tag{3.30}$$

see also Olson, Auer & Buchler (1986).

We treat shocks as real discontinuities in the physical variables so that we have to deal with large differences in optical distances $\Delta\tau$ between adjacent grid-points and, at the shock-points themselves with vanishing optical distances, $\Delta\tau = 0$. Another complication arises from the fact that density and temperature, as well as velocity, undergo rapid variations from pre-shock to post-shock regions, causing discontinuous jumps in the extinction and the emissivity as well as in $\overline{J}$. On the other hand, the monochromatic specific and mean intensities are continuous over the shock-points, which must be reproduced by the numerical solution. Therefore, to compute the formal solution, we integrate the transfer equation using a piecewise linear interpolation to the source function. For such an interpolation, Kalkofen and Ulmschneider (1984) showed that the specific intensities along an outgoing ray can be written as

$$I^+_{dr} = a^+_{dr} I^+_{(d+1)r} + b^+_{dr} S_{dr} + c^+_{dr} S_{(d+1)r} \quad , \tag{3.31}$$

with

$$\begin{array}{llll} a^+_{dr} = & \frac{2-\delta}{2+\delta}; & b^+_{dr} = c^+_{dr} = \frac{\delta}{2+\delta}, & \delta \leq 1 \\ a^+_{dr} = & c^+_{dr} = \frac{1}{2\delta+1}; & b^+_{dr} = \frac{2\delta-1}{2\delta+1}, & \delta > 1 \end{array} \tag{3.32}$$

where

$$\delta = \tau_{(d+1)r} - \tau_{dr} . \tag{3.33}$$

Here τ_{dr} denotes the optical depth at grid-point d along the outgoing ray with index r. The superscript "+" denotes outgoing ($\mu > 0$) radiation. Similarly we find for the ingoing ($\mu < 0$, superscript "$-$") intensities

$$I^-_{dr} = a^-_{dr} I^-_{(d-1)r} + b^-_{dr} S_{dr} + c^-_{dr} S_{(d-1)r} \quad , \tag{3.34}$$

where the values a^-_{dr}, b^-_{dr}, c^-_{dr} are the same as the a^+_{dr}, b^+_{dr}, c^+_{dr} except that now

$$\delta = \tau_{dr} - \tau_{(d-1)r} \quad , \tag{3.35}$$

with the optical depth along the ingoing ray. The formal solution is then obtained by integrating the specific intensities over all rays and directions as indicated by Eq. (3.14).

Choice of Λ^*

A crucial point concerning the performance and reliability of operator splitting methods is the choice of the approximate operator $\mathbf{\Lambda}^*$. Cannon (1973) constructed an approximate operator by reducing the number of frequency and angle grid points used for the $\mathbf{\Lambda}^*$- operator compared to the full set $(\nu_{\rm n}, \mu_{\rm m})$ of the formal solution. By this choice the computational effort to invert $\mathbf{\Lambda}^*$ could be reduced. Another approach by Scharmer (1981) combined Cannon's method with the idea of *core saturation* (Rybicki 1972). This method discriminates between photons in the line wing and the line core where the optical depth is so large that the photons are trapped. For the calculation of $\mathbf{\Lambda}^*$ only the photons in the line wings are considered and one cuts out those frequencies and directions where the medium is optically thick. Furthermore the Eddington -Barbier approximation is used to calculate the intensity at a certain point in the slab. The resulting matrix then takes approximately triangular shape and can be inverted by very efficient numerical methods.

The concept of core saturation has also been applied by Ulmschneider and Kalkofen (1984) to the solution of the RTE in moving media with shocks. Here the radiation in the line wings is calculated using ordinary Λ–iteration and the line core is treated as optically thick with $S = B(T)$. The method has subsequently been used for modeling line radiation in the solar chromosphere. In order to separate the line wing from the core a free parameter $\Delta\tau_\gamma$ has to be specified properly to ensure a stable convergence behavior and to avoid spurious solutions. This parameter gives the limiting optical distance between two adjacent grid points up to which a photon is said to be in the line wing. Usually $\Delta\tau_\gamma$ is chosen the order of unity. As the structure of the atmosphere in our calculations changes at each time step it is impossible to adjust the parameter to a value where convergence could be assured without losing speed of computation. For a further discussion on these problems see Rammacher (1991) and Buchholz et al. (1994).

Olson, Auer & Buchler (1986, OAB) showed, that a good choice for $\mathbf{\Lambda}^*$ is the main diagonal of the exact matrix. In that case, $\mathbf{\Lambda}^*$ is a diagonal matrix and the operator splitting method is the classical Jacobi-method for the solution of linear equations. Using a tri-diagonal $\mathbf{\Lambda}^*$, Olson & Kunasz (1987,OK) could considerably improve the convergence rate and decrease the amount of CPU time required for the solution of line transfer problems. In addition, they introduced the so-called *short-characteristics method* to calculate the formal solution for the specific intensities. As stated before, the elements of the exact Λ-matrix can be found by solving the RTE for a "pulse" like source function (see equation (3.30)) using equations (3.31) and (3.34) with the coefficients of equation (3.32). In this case, the elements of $\mathbf{\Lambda}$ and therefore $\mathbf{\Lambda}^*$, are given by combinations of the coefficients of equation (3.32) (Buchholz et al., 1994).

Our approach to the solution of the transfer equation (3.19) closely resembles the method used by OK, with the main advantage that the costly calculations of exponentials are avoided. Furthermore, our choice of quadrature coefficients, Eq. (3.32), *unconditionally guarantees* a stable solution of the transfer equation, even for the very irregular τ-grids encountered in our hydrodynamic calculations (Kalkofen and Wehrse, 1982). In addition, this form of the formal solution gives the correct run of the intensity over the shock points.

In our hydrodynamical wave calculations, we use the tridiagonal $\mathbf{\Lambda}^*$ with Ng-Acceleration (Auer 1987, 1991). The speed of the method is further improved by using the result for S of the old hydrodynamic time step as starting value for the operator splitting in the following time step. For temperature-correction methods used to obtain an initial model atmosphere, we found that the best choice is a $\mathbf{\Lambda}^*$ with a bandwidth of nine for calculations performed on an IBM 3090-180VF.

3.3 Line Radiation with Partial Redistribution

We described in the preceding section our method of radiative transfer under the assumption of complete redistribution. In this approximation the highly idealized case of identical absorption and emission profiles is used and coherence effects are neglected. CRD provides a reasonable description of the line transfer if the spectral lines are formed under conditions with frequent collisions. In this case the absorption process is immediately followed by an collision of the excited atom. The disturbances caused by the collision will then lead to a loss of information about the initial state of the absorbed photon. Frequency and direction of the reemitted photon will show no correlation to the absorbed photon.

The chromospheric diagnostic lines are formed in the middle chromosphere where the collisional rates are too low for a reasonable application of CRD. If scattering takes place under chromospheric conditions, the reemitted photon will have its frequency and direction changed only slightly and the scattering is essentially coherent. For that case we have to apply the approximation of *partial redistribution* (PRD). The coherence between the incoming and the scattered photon is described by the *redistribution function* $R(\nu', \mu'; \nu, \mu)$ giving the conditional probability that a photon absorbed from the ray (ν', μ') will be scattered into the ray (ν, μ).

We can write the total source function as

$$S_{\nu\mu}(z) = \frac{\varphi_{\nu\mu}(z) S^{\mathrm{L}}_{\nu\mu}(z) + r(z) B(z)}{\varphi_{\nu\mu}(z) + r(z)} \quad , \tag{3.36}$$

where analogous to equation (3.15) B is the Planck function. Contrary to the CRD case the line source function $S^{\mathrm{L}}_{\nu\mu}(z)$ is now frequency and angle dependent.

Following Paletou and Auer (1994) we introduce the mean PRD intensity

$$\overline{J}_{\nu\mu}(z) = \int \int G(\nu', \mu'; \nu, \mu) \; I_{\nu'\mu'}(z) \mathrm{d}\mu' \; \mathrm{d}\nu' \tag{3.37}$$

with

$$G(\nu', \mu'; \nu, \mu) \equiv \frac{R(\nu', \mu'; \nu, \mu)}{\varphi_{\nu\mu}} \quad . \tag{3.38}$$

The frequency and angle dependent line source function is then given as

$$S^{\mathrm{L}}_{\nu\mu}(z) = (1 - \epsilon(z))\overline{J}_{\nu\mu}(z) + \epsilon(z)B(z) \tag{3.39}$$

in analogy to the CRD case. For a given source function $S_{\nu\mu}$, the transfer equation (3.19) can be integrated for each ray, and equation (3.37) gives the formal solution of the transfer equation in PRD. As in the CRD case, the sequence of operations needed to obtain the mean intensity from the total source function is called Λ-operation.

We now need to specify the redistribution function R. For a two-level atom with a sharp lower level and a broadened upper level one can show that the redistribution function has two contributions (Milkey and Mihalas,1973),

$$R = \beta \ R^{\mathrm{II}} + (1 - \beta) \ R^{\mathrm{III}} \quad . \tag{3.40}$$

In equation (3.40) we dropped the subscripts denoting the frequencies and directions of incoming and scattered photons. R^{II} gives the redistribution function for strictly coherent scattering in the atoms frame of reference and the upper level of the transition is only naturally broadened. R^{III} corresponds to the case of complete redistribution in the atoms rest frame with the upper state broadened naturally and collisionally. The coefficient β is given as (Cheng, 1991)

$$\beta = \frac{\Gamma_{\mathrm{rad}} + \Gamma_{\mathrm{inelastic}}}{\Gamma_{\mathrm{rad}} + \Gamma_{\mathrm{inelastic}} + \Gamma_{\mathrm{elastic}}} \tag{3.41}$$

with Γ_{rad}, $\Gamma_{\mathrm{inelastic}}$, and $\Gamma_{\mathrm{elastic}}$ expressing the widths by radiative decays, inelastic collisions and elastic collisions, respectively. For our calculations we use the angle-averaged redistribution function in the fluid frame (Vardavas, 1976) and the transformation into the observers frame is given by (Cheng, 1991)

$$R(\nu', \mu'; \nu, \mu) = R(\alpha' - u\mu', \alpha - u\mu) \quad , \tag{3.42}$$

with

$$\alpha' \equiv \frac{\nu' - \nu_0}{\Delta\nu_{\mathrm{D}}} \quad ,$$

$$\alpha \equiv \frac{\nu - \nu_0}{\Delta\nu_{\mathrm{D}}} \quad ,$$

and

$$u \equiv \frac{\nu_0(v/c_{\mathrm{L}})}{\Delta\nu_{\mathrm{D}}} \quad .$$

Here, v is the gas velocity. We solve the transfer equation for line radiation in PRD using an operator splitting method similar to that employed for the CRD case (Ulmschneider, 1994). We restrict ourselves to two beams and distribute the frequency points in a small frequency range around the line center. This is done in order to resolve the emission cores resulting from the temperature inversion in the chromosphere with as few frequency points as possible in order to save computational time.

We assume that the branching ratio β in equation (3.40) can be approximated by unity, thus leading to $R = R^{\mathrm{II}}$, and R^{II} is calculated using the approximation of Gouttebroze (1986).

In order to save computer memory, we use a diagonal $\mathbf{\Lambda}^*$-operator instead of the tridiagonal operator used for CRD. The inversion of $\mathbf{\Lambda}^*$ now requires the inversion of an $N \times N$ matrix at each height grid point. N gives the number of frequency points. As before, for a given timestep the redistribution matrices and the inverse of the $\mathbf{\Lambda}^*$ are precomputed and reused during the iteration cycle. During a sequence of calculating the radiative transfer for several successive time steps the results from the preceding time step are used as a first guess of the current time step. The rate of convergence is further improved by using Ng-acceleration similar to the CRD calculations.

Compared to the CRD case, the rate of convergence is reduced. One needs about 200 iterations to achieve a reasonable accuracy of 0.1 percent (Ulmschneider, 1994). The same accuracy for the CRD case with tridiagonal $\mathbf{\Lambda}^*$-operator only needs 55 iterations, showing the effect of the additional elements in the operator on the rate of convergence.

As the calculation of line transfer in PRD is very costly in terms of memory as well as of computational time, it is only applied to selected phases of the wave calculations in order to obtain the chromospheric line emission.

3.4 Continuous Radiation

The major difference between continuous radiation and spectral lines is that the continuous opacity does not vary strongly with frequency. Therefore we do not need to take care of effects caused by the differential motion of the radiating gas, like the Doppler effect. Furthermore a much smaller number of frequency points is required to calculate the continuous radiation for a large frequency range.

The transfer equation is written as

$$\mu \frac{\mathrm{d}I_\nu}{\mathrm{d}z} = -\chi_\nu (I_\nu - S_\nu) \tag{3.43}$$

and solved on a discrete τ-grid with

$$\tau_i = \frac{\tau_\nu(z_i)}{|\mu|} \tag{3.44}$$

using a method based on an integral equation (Kalkofen 1974).

We apply the two-stream approximation and consider only one angle point with $\mu = 1/\sqrt{3}$. The discretized equation of transfer for the monochromatic specific intensity in the outgoing direction ($\mu = +1/\sqrt{3}$) is written as

$$I_i^+ = I_{\mathrm{BC}}^+ e^{-(\tau_N - \tau_i)} + \sum_{k=i}^{N-1} \int_{\tau_k}^{\tau_{k+1}} S(t) e^{-(t-\tau_i)} \mathrm{d}t \tag{3.45}$$

with the intensity I_{BC} which enters the photosphere from deeper layers as the boundary condition for the outgoing radiation. I_{BC} is computed under the assumption that the temperature structure of the layers beneath the computational domain is that of the gray case. The value of I_{BC}^+ can be precomputed and is held fixed throughout the time dependent calculations. Similarly the intensity in the ingoing ray is

$$I_i^- = \sum_{k=i}^{i} \int_{\tau_{k-1}}^{\tau_k} S(t) e^{-(\tau_i - t)} \mathrm{d}t \tag{3.46}$$

where the boundary condition of vanishing incoming radiation, $I_1^- = 0$, is used.

I_i^+ and I_i^- are computed recursively using a parabolic expansion of the source function in the interval ($\tau_i \leq t \leq \tau_{i+1}$):

$$S(t) = S_i + (t - \tau_i)S' + (t - \tau_i)^2 S'' \quad . \tag{3.47}$$

S' and S'' are determined by the requirement that (3.47) be satisfied at three neighboring grid points.

Performing the integrations in (3.45) and (3.46) then leads to recursion equations for the ingoing and the outgoing radiation (Kalkofen and Ulmschneider, 1977).

To ensure the validity of the diffusion limit at large optical depth, I^+ and I^- at a grid-point i are calculated with their respective leading parabola which for both directions runs through grid-points $(i-1, i, i+1)$. The resulting coefficients can be found in Kalkofen and Ulmschneider (1977).

The calculation scheme has to be altered at the shock points where the infinitesimally small geometrical distances lead to vanishing $\Delta\tau$. If the respective leading parabolas crossed the shock, the calculation switches to trailing parabolas (see Fig.(3.1)). For the outgoing ray, grid-points $s_2, i, i+1$ are used to obtain the intensity at the post-shock point s_2 and, as the monochromatic intensities are unaffected by the infinitesimally small shock front, one has $I_{s_1}^+ = I_{s_2}^+$ at the pre-shock point. In analogy, the ingoing intensity is calculated through points $i-2, i-1, s_1$, and $I_{s_2}^- = I_{s_1}^-$ is the intensity at the post-shock point.

3.5 Opacity of H^-

Wildt (1939) identified the negative hydrogen ion H^- as the main source of solar photospheric absorption and emission. It is responsible for about 95 percent of the continuous

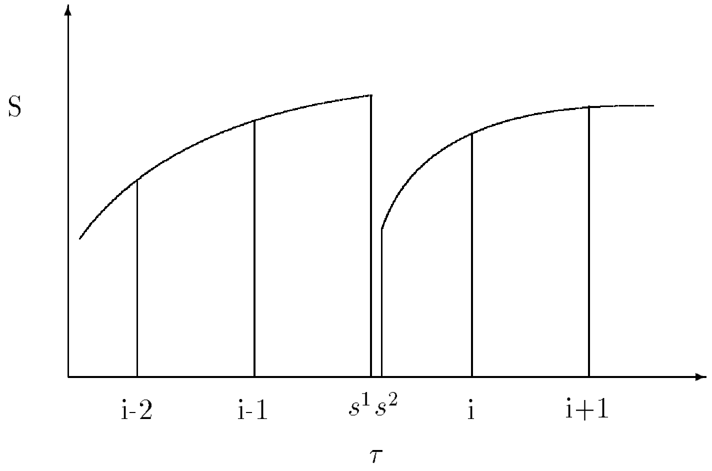

Figure 3.1: Calculation of the intensities at shock points

radiation of cool stars. The negative hydrogen ion is formed by the attachment of electrons provided by ionized metals like, e.g. Magnesium. The ionization potential is only 0.75 eV and photoionization of H^- is possible for wavelengths below $\lambda = 1.65\ \mu m$.

The total opacity of H^- consists of two parts,

$$\chi_\nu = \chi_\nu^{\mathrm{ff}} + \chi_\nu^{\mathrm{bf}} \tag{3.48}$$

with free-free radiation dominating from the far infrared up to $\lambda \approx 16000$ Å . Bound-free absorption extends from the wavelength of photoionization to the violet with a maximum around 8500 Å.

After Kurucz (1970), we use

$$\chi_\nu^{\mathrm{ff}} = n_{\mathrm{H}} n_{\mathrm{e}} \mathcal{F}_\nu(T) \tag{3.49}$$

for the free-free absorption, where $\mathcal{F}_\nu(T)$ is a fit to theoretical calculations of Stilley and Callaway (1970) and has the form

$$\mathcal{F}_\nu(T) = [1.3727{\times}10^{-25} + (4.3748{\times}10^{-10} - 2.5993{\times}10^{-7}/T)/\nu]/\nu \quad . \tag{3.50}$$

Assuming that the electron density and the collisional rates are large enough, the free-free source function is treated in LTE

$$S_\nu^{\mathrm{ff}} = B_\nu(T) \tag{3.51}$$

and $B_\nu(T)$ is the Planck function at the local temperature T.

Unfortunately, dependent on the frequency, the fit (3.50) can result in negative values for the opacity at low temperatures. At $\nu = 8.56 \times 10^{10}$, $\mathcal{F}_\nu(T)$ yields negative results for temperatures below $T_{\mathrm{crit}} \approx 600\ K$. The critical temperature where the fit formula produces unphysical results is lower for higher frequencies. Although such low temperatures are unlikely to occur during our calculations, precautions have to be taken to avoid spurious results caused by using (3.49) below $T_{\rm crit}$. If $\chi_\nu^{\rm ff}$ has to be calculated for temperatures below 600 K, the value of $\mathcal{F}_\nu(T = 600\ {\rm K})$ is adopted instead.

The bound-free opacity can be written as (Mihalas and Mihalas 1984)

$$\chi_\nu^{\rm bf} = \left(n_{H-} - n^*_{H-} e^{-\frac{h\nu}{kT}}\right) \alpha_\nu^{\rm bf} \tag{3.52}$$

and the emissivity is given by

$$\eta_\nu^{\rm bf} = \frac{2h\nu^3}{c_L^2} n^*_{H-} e^{-\frac{h\nu}{kT}} \alpha_\nu^{\rm bf} \quad . \tag{3.53}$$

n_i and n_i^* are the current and the LTE number densities of the negative hydrogen ion, and $\alpha_\nu^{\rm bf}$ is the cross section of photoionization. Using

$$b_{H-} = \frac{n_{H-}}{n^*_{H-}} \tag{3.54}$$

we have from (3.52)

$$\chi_\nu^{\rm bf} = n^*_{H-}\, b_{H-}\, \alpha_\nu^{\rm bf} \left(1 - \frac{e^{-\frac{h\nu}{kT}}}{b_{H-}}\right) \tag{3.55}$$

as the opacity and with (3.53) the bound-free source function is obtained as

$$S_\nu^{\rm bf} \equiv \frac{\eta_\nu^{\rm bf}}{\chi_\nu^{\rm bf}} = \frac{2h\nu^3}{c_L^2} \frac{1}{b_{H-} e^{\frac{h\nu}{kT}} - 1} \quad . \tag{3.56}$$

The number density of H^- is computed directly using the Saha equation,

$$n^*_{H-} = \frac{g_{H-} n^*_H n_e}{g_H g_e} \left(\frac{h^2}{2\pi m_e kT}\right)^{\frac{3}{2}} e^{\varepsilon_{\rm Ion}/kT} \quad . \tag{3.57}$$

The statistical weights are $g_{\rm H-} = 1$, $g_{\rm H} = 2$ and $g_{\rm e} = 2$ and ionization potential is $\varepsilon = 0.785$eV.

The departure coefficient $b_{\rm H-}$ describes the deviation of the current number density of the negative hydrogen ion from the number density expected in LTE. In LTE, the rate equations describing the production and destruction of H^-, are dominated by collisional rates, whereas increasing influence of radiative processes is characteristic for non-LTE rate equations.

To evaluate the rate equations responsible for the number density of H^- we consider in particular (Schmitz et al. 1985) photoionization,

$$H^- + h\nu \longleftrightarrow H + e \tag{3.58}$$

and collisions with free electrons,

$$H^- + e \longleftrightarrow H + 2e \quad . \tag{3.59}$$

The rate of destruction of H^- by collisions with neutral hydrogen atoms,

$$H^- + H \longleftrightarrow H_2 + e \tag{3.60}$$

which results in the production of hydrogen molecules, is influenced by the production of H_2 in the process

$$3H \longleftrightarrow H_2 + H \quad . \tag{3.61}$$

With the radiation field given by the mean monochromatic intensity J_ν, the radiative rates are

$$R_\uparrow = 4\pi \int_{\nu_1}^{\infty} \frac{\alpha_\nu^{\rm bf} J_\nu}{h\nu} d\nu \tag{3.62}$$

for the photoionization (3.58), and

$$R_\downarrow = \frac{n_{H^-}^*}{n_H^*} R^\dagger \tag{3.63}$$

for the radiative recombination, where $R^\dagger$ is defined as

$$R^\dagger = 4\pi \int_{\nu_1}^{\infty} \frac{\alpha_\nu^{\rm bf} e^{-\frac{h\nu}{kT}}}{h\nu} \left(\frac{2h\nu^3}{c_L^2} + J_\nu \right) d\nu \quad . \tag{3.64}$$

We can collect the different collisional rates and write (Schmitz et al. 1985)

$$r = 2.0 \times 10^{-9} \left(\frac{n_H}{1+\delta} + \theta^{-\frac{3}{2}} n_e \right) \tag{3.65}$$

where δ is

$$\delta = 58\sqrt{\theta} e^{1.736\,\theta} \frac{n_e}{n_H} \tag{3.66}$$

and we used the usual definition of $\theta \equiv \frac{5040}{T}$. The departure coefficient is now given as

$$b_{H^-} = \frac{R^\dagger + r}{R_\uparrow + r} \quad . \tag{3.67}$$

From equations (3.52) and (3.56) we see that the opacity and subsequently the bound-free source function depend on the departure coefficient $b_{\rm H^-}$ which in turn, via the radiation field J_ν, is dependent on S_ν^{bf}. Therefore, the solution for the NLTE source function must be found iteratively. As the typical optical depths as well as the optical distances between grid-points are not very large for the upper photosphere and lower chromospheric regions, ordinary $\mathbf{\Lambda}$-iteration is used. During the time dependent calculations the convergence is increased by reusing the solutions from the previous time step as initial guess for the source function in the current time step.

3.6 Radiative Cooling

In our time dependent calculations we assume that the acoustic waves lose energy only by radiative damping. The solution of the radiative transfer equation for lines and the continuum described in the preceding sections is done to obtain the value of the radiative damping function $D = \frac{\mathrm{d}s}{\mathrm{d}t}\Big|_{\mathrm{rad}}$ for all grid points and at each time step.

To determine the energy losses we integrate the equation of transfer

$$\frac{1}{c_{\mathrm{L}}}\frac{\partial I_{\nu\mu}}{\partial t} + \mu\frac{\partial I_{\nu\mu}}{\partial z} = -\chi_{\nu\mu}(I_{\nu\mu} - S_{\nu\mu}) \tag{3.68}$$

over frequency and angle. For completeness the term $\frac{1}{c_{\mathrm{L}}}\frac{\partial I_{\nu\mu}}{\partial t}$ is added, which we neglected in writing the time independent equation of transfer in (3.1) or (3.48). The integration yields

$$\frac{4\pi}{c_L}\frac{\partial J}{\partial t} + \frac{\partial F}{\partial z} = -2\pi\int\int\chi_{\nu\mu}(I_{\nu\mu} - S_{\nu\mu})\mathrm{d}\mu\ \mathrm{d}\nu \tag{3.69}$$

with the mean intensity

$$J = \frac{1}{2}\int\int I_{\nu\mu}\mathrm{d}\mu\mathrm{d}\nu \tag{3.70}$$

and the radiative flux

$$F \equiv 2\pi\int\int\mu I_{\nu\mu}\,\mathrm{d}\mu\,\mathrm{d}\nu \quad . \tag{3.71}$$

The first term on the right hand side of equation (3.69) gives the time derivative of the energy density $u = \frac{4\pi}{c_L}J$ of the radiation field, the second denotes the divergence of the radiative energy flux. Equation (3.69) is the equation of conservation for the radiative energy with the right hand side denoting the sources and sinks of the field. Changes of the radiative field energy by interaction with the absorbing or emitting gas lead to changes of the energy content $\mathrm{d}Q$ (erg cm^{-3}) of the gas. For late type stars the derivative of the energy density may be neglected (Kalkofen and Ulmschneider, 1977) and we write the change of energy of the gas element due to radiation as

$$\frac{dQ}{dt}\Big|_{\mathrm{rad}} = -\frac{\partial F}{\partial z} \equiv -\Phi_R \tag{3.72}$$

as definition for the radiative cooling rate Φ_R. The solution of the hydrodynamic equations requires the radiative change of the entropy s which is given by

$$D = \frac{\mathrm{d}s}{\mathrm{d}t}\Big|_{\mathrm{rad}} = \frac{1}{\varrho\,T}\,\frac{dQ}{dt}\Big|_{\mathrm{rad}} \quad . \tag{3.73}$$

By comparing with (3.69) we find

$$D = \frac{2\pi}{\varrho T}\int\int\chi_{\nu\mu}(I_{\nu\mu} - S_{\nu\mu})\mathrm{d}\mu\ \mathrm{d}\nu \quad . \tag{3.74}$$

We consider several contributions to the radiative energy transfer. The radiative damping by H^- is computed as

$$D = \frac{4\pi}{T}\int_0^\infty[\kappa_\nu^{\mathrm{bf}}\,(J_\nu - S_\nu^{\mathrm{bf}}) + \kappa_\nu^{\mathrm{ff}}(J_\nu - B_\nu)]\ \mathrm{d}\nu \quad , \tag{3.75}$$

	MgII k	CaII K	Ly α
relative abundance	$3.9 \cdot 10^{-5}$	$2.82 \cdot 10^{-6}$	1
molecular weight	24.305	40.08	1.008
wavelength	2796 Å	3933 Å	1216 Å
$\Gamma_{\rm rad}[\rm sec^{-1}]$	$2.7 \cdot 10^{8}$	$1.5 \cdot 10^{8}$	$4.72 \cdot 10^{8}$
$\Gamma_{\rm VdW}[\rm sec^{-1}\ cm^{3}]$	$1.0 \cdot 10^{-8}$	$1.1 \cdot 10^{-8}$	0
$\Omega_{21}\ [\rm sec^{-1}\ cm^{3}]$	$3.63 \cdot 10^{-7}$	$2.92 \cdot 10^{-7}$	$2.3 \cdot 10^{-8}$

Table 3.1: Atomic data for the lines used in our computations

where we separated the contributions from free-free and bound-free radiation and performed the integration over μ to express the radiative damping in terms of the monochromatic mean intensity

$$J_\nu = \frac{1}{2} \int I_{\nu\mu}\ \mathrm{d}\mu \quad . \tag{3.76}$$

$\kappa_\nu = \frac{\chi_\nu}{\varrho}$ is the opacity per gram.

Radiative damping by line radiation in the chromosphere is calculated using MgII k as representative line. We assume that the total radiative losses by all the spectral lines can be approximated by the losses in this single line, if CRD is used. Although this is a crude simplification of reality it can be justified by calculations of Ulmschneider et al. (1987) and more recently by Rammacher (1991), demonstrating that the cooling rates calculated this way closely resemble those observed for the sun.

Here the usage of CRD instead of the more realistic case of PRD leads to an overestimation of radiative damping. The enhanced radiative losses of the single line are in good agreement with the total losses of all the chromospheric lines.

The influence of MgII k decreases in the upper parts of the atmosphere, and the atmospheric losses are dominated by Lyman α and the Lyman continuum. These contributions are considered by computing radiation of Lyman α assuming a two-level atom and CRD.

We show the relevant atomic data for our line calculations in Table (3.1) and add the data for the CaII K line for completeness.

For temperatures above $\approx 10^4$ K we use the cooling function

$$Q_{\mathrm{T}>10^4} = -\varrho^2\ P_{\rm rad}(T) \tag{3.77}$$

for an optically thin plasma. The dependence of the radiative energy coefficient $P_{\rm rad}$ with temperature has been calculated by Mc Whirter et al. (1975).

The total radiative damping function D is the sum of the different contributions and is computed as

$$D = D_{\mathrm{H}^-} + D_{\rm Lines} + D_{\rm Mc\,Whirter} \quad . \tag{3.78}$$

D_{Lines} contains the damping by MgII and Ly α.

The contributions from Ly α and the optically thin cooling function are calculated in order to add radiative cooling to the outer parts of the atmosphere. Without energy losses these regions would be adiabatic and the resulting high temperatures would cause numerical problems. As our calculations neglect the effects of hydrogen ionization we do not discuss the results of our models where the temperature largely exceeds 10^4 K.

Chapter 4

Chromospheric Models

In this chapter we present the results from our hydrodynamic calculations for main sequence stars between spectral types F5V and M0V. In Section 4.1, the model assumptions and relevant parameters for the calculations are briefly summarized.

Section 4.2 outlines the characteristic behavior of our time dependent chromospheric models. We explain the changes of the models along the main sequence of the HR-diagram.

In Section 4.3 we examine the differences in radiative damping of acoustic waves as they propagate through the atmospheres.

We then look, in Section 4.4, at the line emissions obtained from our calculations. In Section 4.5 we compare our results with observations, where special emphasis is laid on the basal emissions.

Properties of the time averaged models are discussed in section 4.6 where we compare the outcome of our models with observations and explain the observations as results of the acoustic origin of magnetically inactive chromospheres.

Section 4.7 adresses the height dependence of the heating rates found in our model calculations. We compare our results with those from weak shock heating and results from semi-empirical modeling of non-nonmagnetic regions on the sun.

In Section 4.8 we briefly present models of two giant stars and check whether the absence of a gravity dependence of the basal emission can be explained by the properties of acoustic heating.

4.1 Model Assumptions

For a calculation of acoustically heated chromospheres in late type stars we use purely monochromatic waves. The motion of the piston is sinusoidal,

$$u(t) = -u_0 \sin\left(\frac{2\pi}{P_0}t\right) \tag{4.1}$$

with the period P_0 of the acoustic wave. The velocity amplitude u_0 is determined by the input mechanical flux F_{M} and is given as (Ulmschneider et al. 1977)

$$u_0 = \left[\frac{2\pi F_{\mathrm{M}}}{\varrho_0 c_0}\right]^{1/2} \tag{4.2}$$

with the initial density ϱ_0 and sound speed c_0 at the bottom of the atmosphere. The piston velocity in (4.1) is chosen to be negative for the first half period to ensure that the initial disturbance running into the atmosphere is an expansion rather than a compression. This considerably reduces the oscillations triggered by the very first wave running into the undisturbed atmosphere.

Bohn (1984) using mixing length models of stellar convection zones, calculated the theoretical acoustic energy production by the turbulent surface layers of the stars. The results of this work are shown in Fig.(4.1), where the acoustic flux versus the effective temperature is shown for stellar models with different values of $\log g$. Bohn gives a fit for the linear part of the curves in Fig.(4.1) as

$$F_a \approx 6 \cdot 10^8 \left(\frac{T_{\mathrm{eff}}}{T_{\mathrm{eff},\odot}}\right)^{9.75} \left(\frac{g_\odot}{g}\right)^{0.5} \left(\frac{\alpha}{1.5}\right)^{2.8} \mathrm{erg\,cm^{-2}\,sec^{-1}} \tag{4.3}$$

Here, the subscript $\odot$ denotes the solar values of effective temperature and surface gravity and α is the mixing-length parameter

$$\alpha = \frac{L_{\mathrm{M}}}{H} \quad , \tag{4.4}$$

with the pressure scale height H and the mixing length L_{M}. The calculations made by Bohn (1981,1984) also showed, that for stars on the main sequence the maximum of the acoustic frequency spectrum is in the region between $10 \cdot \omega_{\mathrm{ac}}$ and $5 \cdot \omega_{\mathrm{ac}}$ with a slight shift towards the lower frequencies for stars with decreasing T_{eff}. Here $\omega_{\mathrm{ac}} = \gamma g / 2 c_{\mathrm{s}}$ is the acoustic cutoff frequency. Figure (4.2) shows the acoustic frequency spectra calculated by Bohn (1981) for main sequence stars.

For our calculations we make the simplifying assumption that the entire acoustic wave flux enters the atmosphere as monochromatic waves with a fixed frequency of $\omega_0 = 5 \cdot \omega_{\mathrm{ac}}$ corresponding to a wave period of $P_0 = 2\pi/\omega_0 = 0.2 \cdot P_{\mathrm{ac}}$.

This choice can be justified by recent results of Sutmann (1994, see also Sutmann and Ulmschneider 1994), who used different kinds of frequency spectra to examine the wave propagation in the solar atmosphere for adiabatic cases. The results for averaged shock strengths are in good agreement with those obtained from calculations with a purely monochromatic wave of a period of about $0.2 \cdot P_{\mathrm{ac}}$.

Radiative energy losses are calculated under the assumption that continuous photospheric radiation solely comes from absorption and emission by the negative hydrogen ion

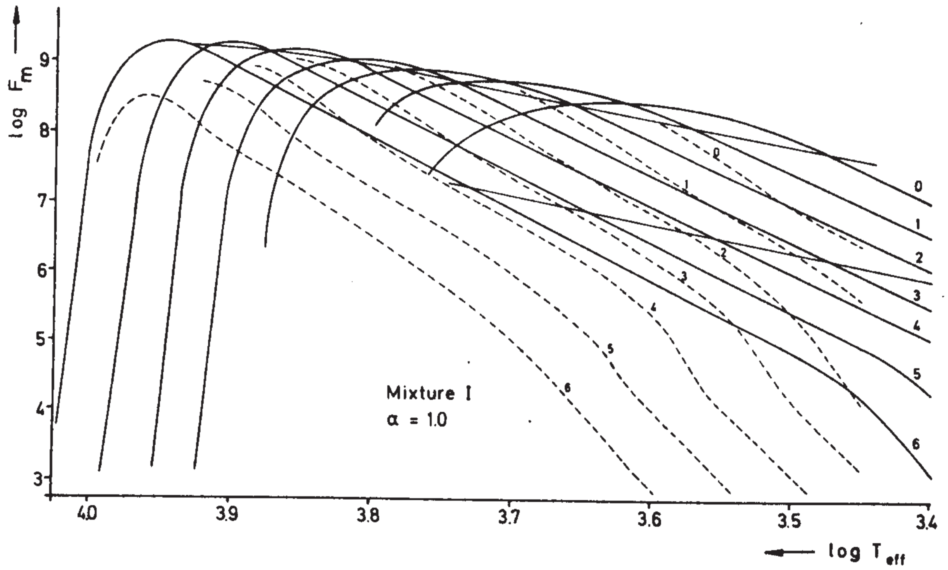

Figure 4.1: Acoustic fluxes after Bohn (1984). Logarithm of the acoustic flux $F_{\rm M}$ vs. $T_{\rm eff}$. The full lines are labelled with log g.

H^-. In the middle chromosphere the radiation loss is mainly due to spectral line emission from the MgII h+k lines as well as from CaII H+K and the infrared triplet lines. The most important emitters in the upper chromosphere and the transition layer are the Lyman lines and continuum.

Ulmschneider et al. (1987) demonstrate that the radiative losses in the solar middle chromosphere can be represented by the emissions of only the MgII k line if one uses the two-level approximation and complete redistribution as described in Chapter 3. We extend their approximation to all the stars of our sample.

In the upper chromosphere radiation from Magnesium is negligible. Without any mechanism of energy loss the shocks would heat up these parts of the atmosphere to extremely high temperatures which are not observed. We therefore included Lyman α in the two-level approximation to serve as cooling agent in the upper parts of the atmosphere.

The initial model is calculated form the time independent form of the characteristic equations (2.31)-(2.33). A temperature correction method described by Cuntz, Rammacher and Ulmschneider (1994) is applied to ensure that the gradient of the total radiative flux calculated from the emitters mentioned above vanishes for the entire atmosphere. This procedure results in an atmospheric model which is in radiative equilibrium and at rest.

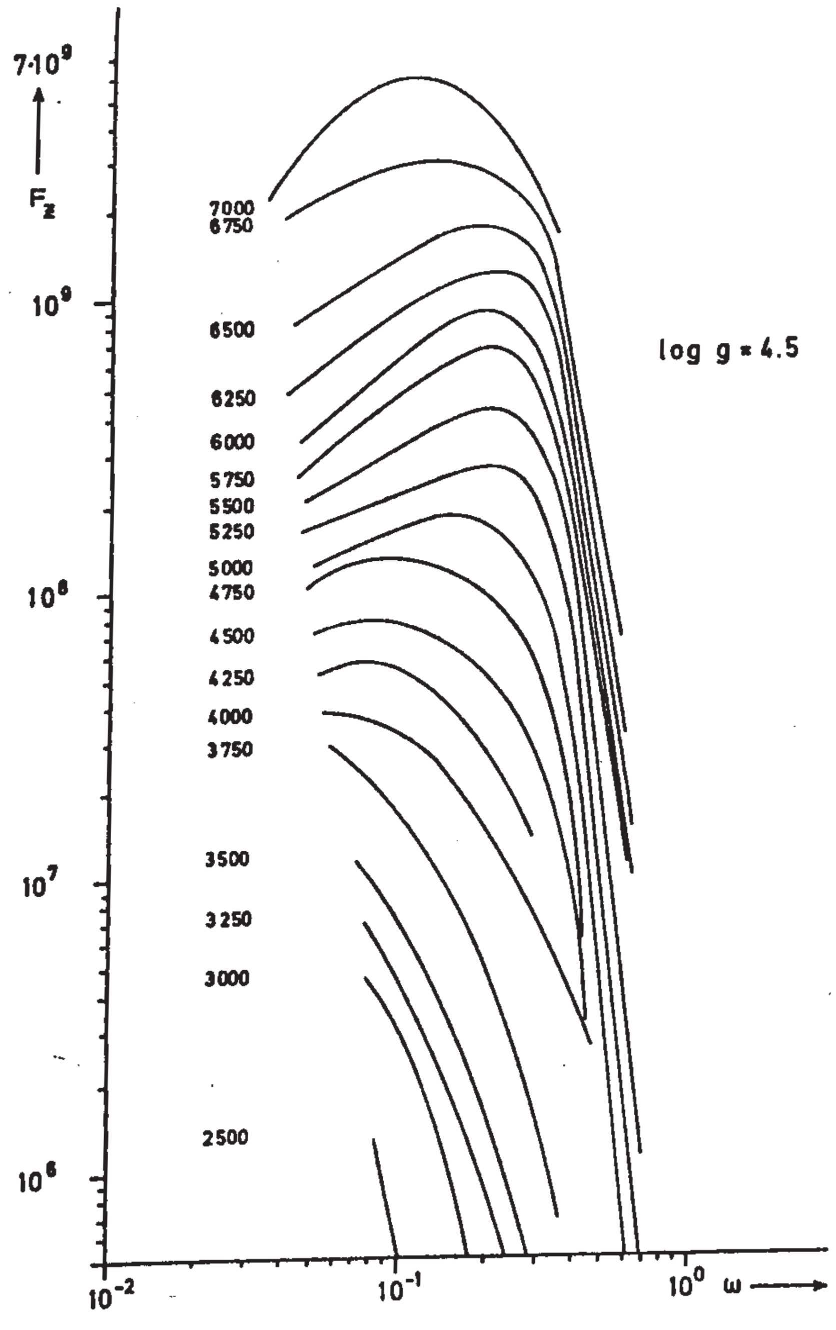

Figure 4.2: Acoustic spectra after Bohn (1984) for stars with log $g = 4.5$ and different values of T_{eff}.

Star	$T_{\rm eff}(K)$	log g	$F_{\rm M}$ (erg cm^{-2}sec^{-1})	P(sec)
F5 V	6440	4.34	$6.56 \cdot 10^8$	50
G0 V	6030	4.39	$3.26 \cdot 10^8$	45
G5 V	5770	4.49	$1.88 \cdot 10^8$	40
K0 V	5250	4.49	$7.53 \cdot 10^7$	35
K5 V	4350	4.54	$1.14 \cdot 10^7$	26
M0 V	3850	4.59	$1.84 \cdot 10^6$	22

Table 4.1: Model parameters for the stars used in this work

4.2 Time Dependent Chromospheric Models

The wave calculations start with the motion of the piston according to (4.1), producing the acoustic waves which heat up the chromosphere by forming shocks. Table 4.1 shows the wave fluxes resulting from equation (4.3) for the different stellar models and the corresponding wave periods. The first wave which enters the atmosphere propagates into an undisturbed medium and develops into a large shock which triggers an oscillatory motion of the upper third of the atmosphere. This oscillation relaxes subsequently. After sufficient time a dynamical equilibrium is reached as the acoustic waves are running continuously through the atmosphere.

We then take time means of the values of temperature, velocity, etc. to produce an averaged chromospheric model which can be compared to semi-empirical models. For each time step used for the averaging procedure the emerging line profiles in PRD for CaII and MgII are calculated and averaged over time to get the mean chromospheric emissions.

The sample of main sequence stars in this investigation ranges from F5 V with $T_{\rm eff}$ = 6440 K and $\log g$ = 4.34 to M0 V with $T_{\rm eff}$ = 3850 K and $\log g$ = 4.59. Fig.(4.3) shows a snapshot of the wave calculation for the F5 V-star after 1123 seconds. The period of the piston for this calculation was 50 seconds, and about 22 wave crests already entered the atmosphere. 20 shocks have developed, and their dissipation has increased the temperature of the outer parts of the atmosphere. The height where the acoustic waves form shocks lies near the column mass density $m = 0.1$ g cm^{-2}, corresponding to a geometric height of about 500 km above the top of the convection zone. The gas velocity for the same phase of the wave is plotted in Fig.(4.4). It shows the deformation of the wave profile with height from a sinusoidal shape to the sawtooth wave form typical for fully developed shocks. The wave amplitude grows as the waves propagate up into regions of decreasing density. In the photosphere it is of the order of 1km/sec. The velocity jumps at the shocks quickly grow from the point of formation until their final value of about 6 km/sec is reached. This velocity

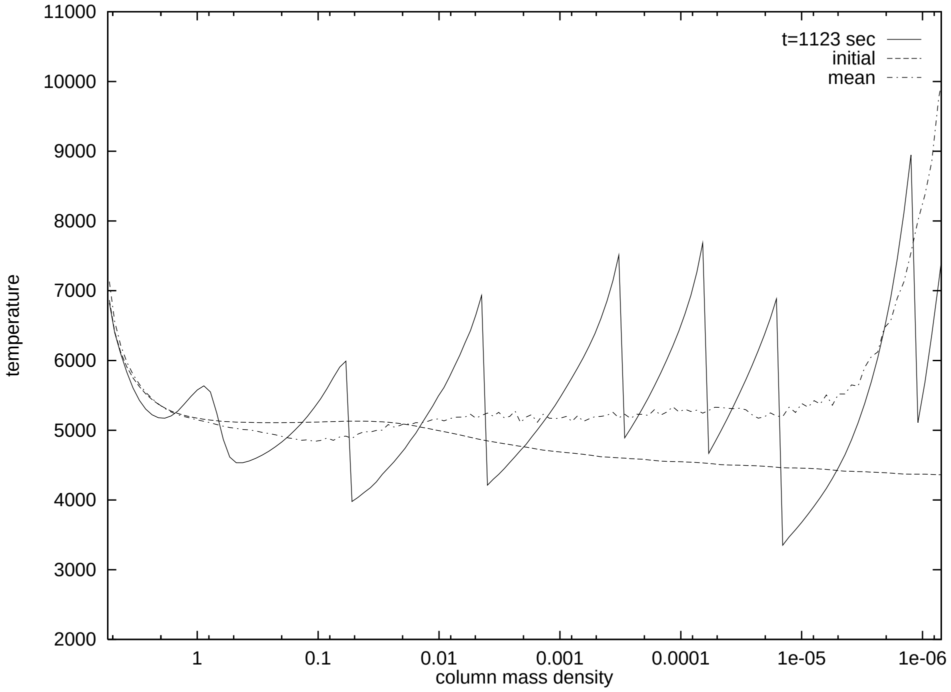

Figure 4.3: Temperature [K] vs. column mass density [g cm^{-2}] for the F5 V model. Shown are: temperature after 1123 sec, initial radiative equilibrium temperature, and mean chromospheric temperature.

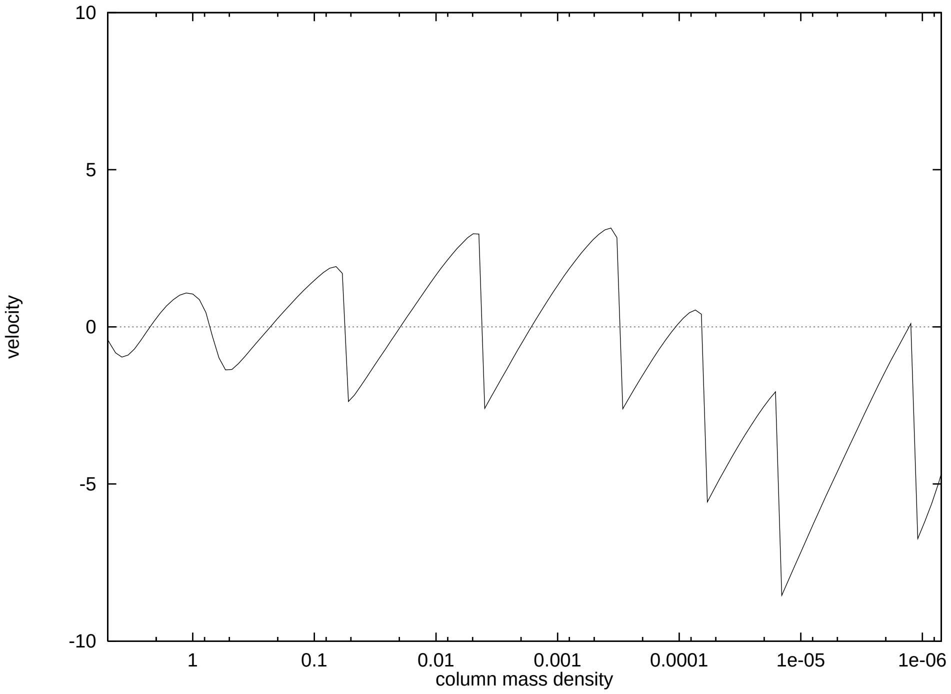

Figure 4.4: Gas velocity [km/sec] vs. column mass density [g cm^{-2}] at t=1123 sec for the F5 V model.

jump remains almost constant although the density decreases by orders of magnitude from bottom to top.

The upper parts of the atmosphere oscillate with the atmospheric eigenfrequency. The oscillation is triggered by large shocks which result from merging of two or more ordinary shocks. This type of excitation of stellar atmospheres has first been found by Rammacher and Ulmschneider (1992), and the process was named *shock overtaking pulsation.* After this large scale pulsation has started, the following wave trains are superimposed over the flow patterns caused by the oscillations.

In Fig.(4.5) the geometrical heights at time t=0 and t=1123 sec are shown as function of the column mass density. Due to the shocks the upper boundary of the atmosphere has been lifted from its initial height of 2250 km to its actual position about 800 km higher. The

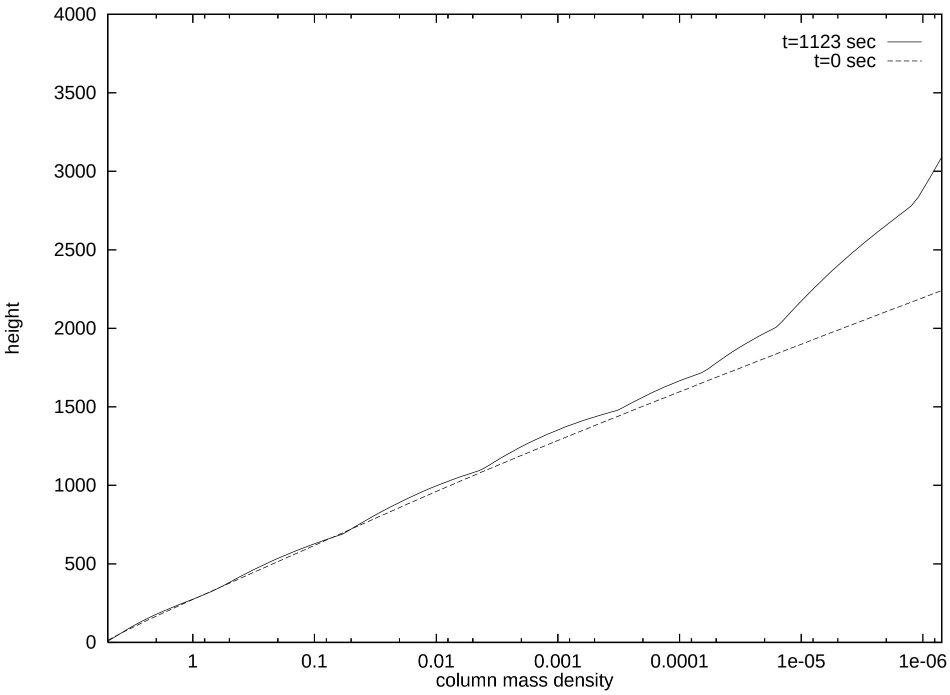

Figure 4.5: Geometrical height [km] at t=1123 sec and of the initial model vs. mass column density [g cm^{-2}].

strength of a shock can be described by the shock strength parameter η, which is defined as

$$\eta = \frac{\varrho_2 - \varrho_1}{\varrho_1} = \frac{\varrho_2}{\varrho_1} - 1 \quad , \tag{4.5}$$

with the density ϱ_1 in front of the shock and ϱ_2 in the post shock region. Another useful parameter is the Mach number,

$$M = \frac{|U|}{c_s} \tag{4.6}$$

which gives the ratio of the flow velocity of the gas through the shock front, $U = u_s - u_1$, to the sound speed. For constant ratio of the specific heats, $\gamma = \frac{c_p}{c_v}$, the Mach number and the densities on both sides of the shock are related via (Witham, 1974)

$$\frac{\varrho_2}{\varrho_1} = \frac{(\gamma+1)M^2}{(\gamma-1)M^2+2} \quad . \tag{4.7}$$

From equation (4.7) we see that for extremely large shocks with $M \to \infty$ the density jump between front and back of the shock only can grow to a maximal size of

$$\lim_{M\to\infty} \frac{\varrho_2}{\varrho_1} = \frac{\gamma+1}{\gamma-1} = 4 \quad , \tag{4.8}$$

thus limiting the shock strength parameter η to a maximal value of $\eta^{\max} = 3$. We can express the Mach number in terms of η as

$$M = \sqrt{\frac{1+\eta}{2-\eta(\gamma-1)}} \quad , \tag{4.9}$$

and the ratio of the pressures in front and behind the shock is written as

$$\frac{p_2}{p_1} = \frac{2\gamma(\eta+1)}{(\gamma+1)(2-\eta(\gamma-1))} \quad . \tag{4.10}$$

The run of the gas density with height is shown in Fig.(4.6). Throughout the atmosphere, we find density jumps of a constant size at the shock points. A similar behavior can be seen in Fig.(4.7) for the gas pressure p. The reason for this is that the shock dissipation counterbalances the influences of the overall decrease in density with height. The property that the jumps ΔT, Δu, $\Delta \varrho$, and Δp attain a constant value over height is called *limiting shock strength behavior*. It is well known from weak shock theory (WST) (see Ulmschneider, 1970), where it can be derived analytically for isothermal, gravitationally stratified atmospheres. Although the weak shock theory is not applicable for our calculations due to the large shock strengths and the non-isothermal structure we can compare our results with those obtained from the WST. In an isothermal, non-ionizing atmosphere under the influence of a surface gravity g, shocks reach a *limiting strength* $\eta^{\lim}$ which is independent of the initial state. For a given atmosphere this shock strength is only dependent on the wave period P and takes a value of (Ulmschneider 1990)

$$\eta^{\lim} = \frac{\gamma\, gP}{(\gamma+1)c_s} \quad . \tag{4.11}$$

We only consider propagating waves with periods shorter than the acoustic cutoff period

$$P_{\rm ac} = \frac{2\pi}{\omega_{\rm ac}} = \frac{4\pi c_s}{\gamma g} \tag{4.12}$$

and write the actual wave period as $P = f \cdot P_{\rm ac}$ with $f < 1$. The resulting limiting shock strength can than be expressed as

$$\eta^{\lim} = \frac{4\pi}{\gamma+1} \cdot f \approx 4.712 \cdot f \quad . \tag{4.13}$$

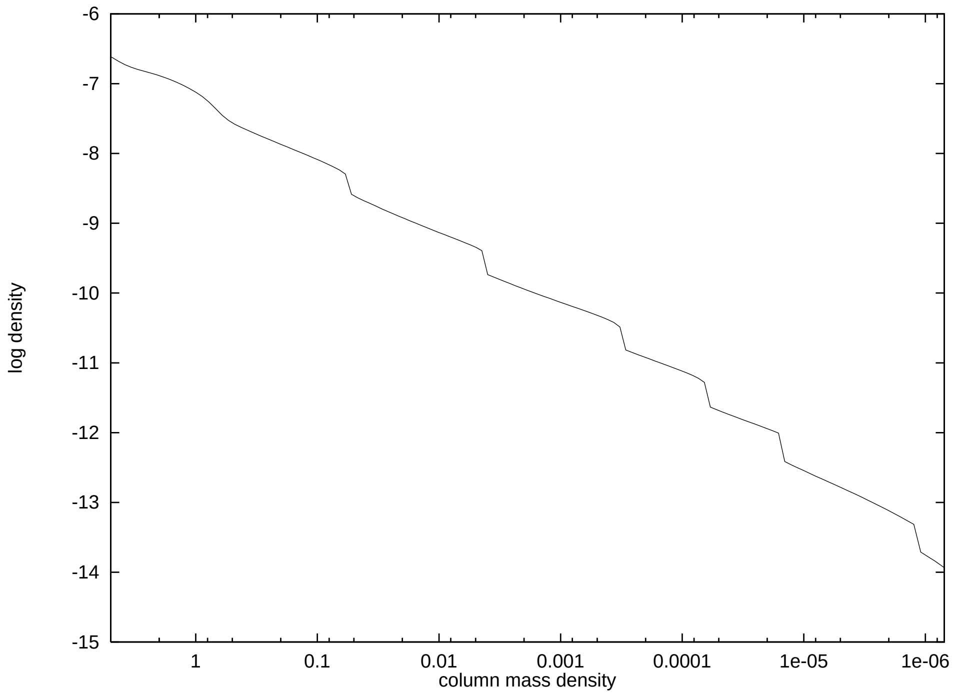

Figure 4.6: Logarithm of the gas density [g cm^{-3}] vs. column mass density [g cm^{-2}] for the F5 V model at t=1123 sec.

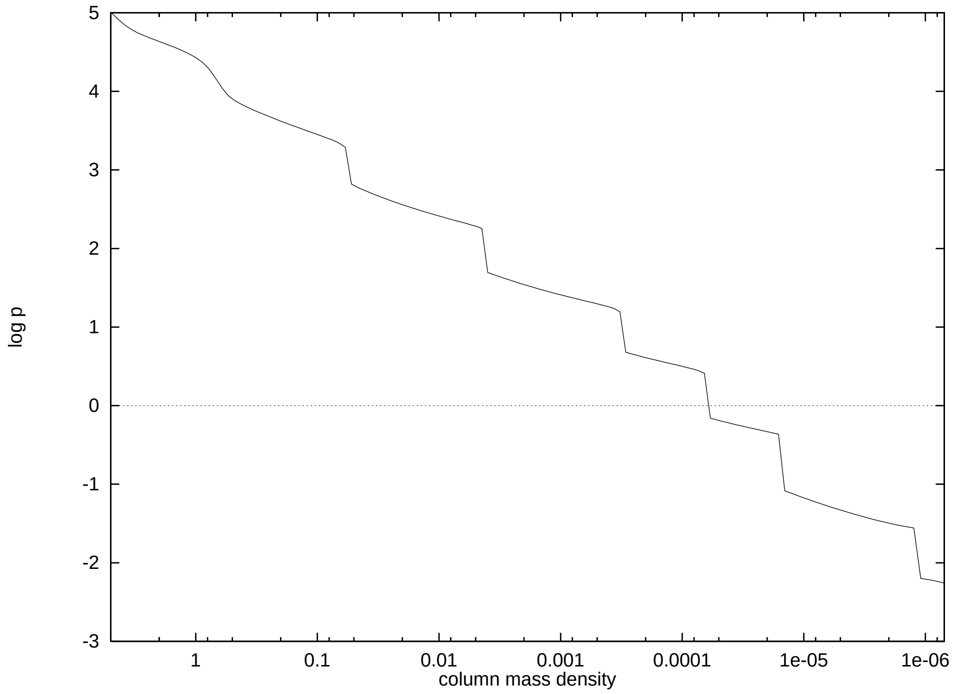

Figure 4.7: Logarithm of the gas pressure [dyn cm^{-2}] vs. column mass density [g cm^{-2}] for the F5 V model at t=1123 sec.

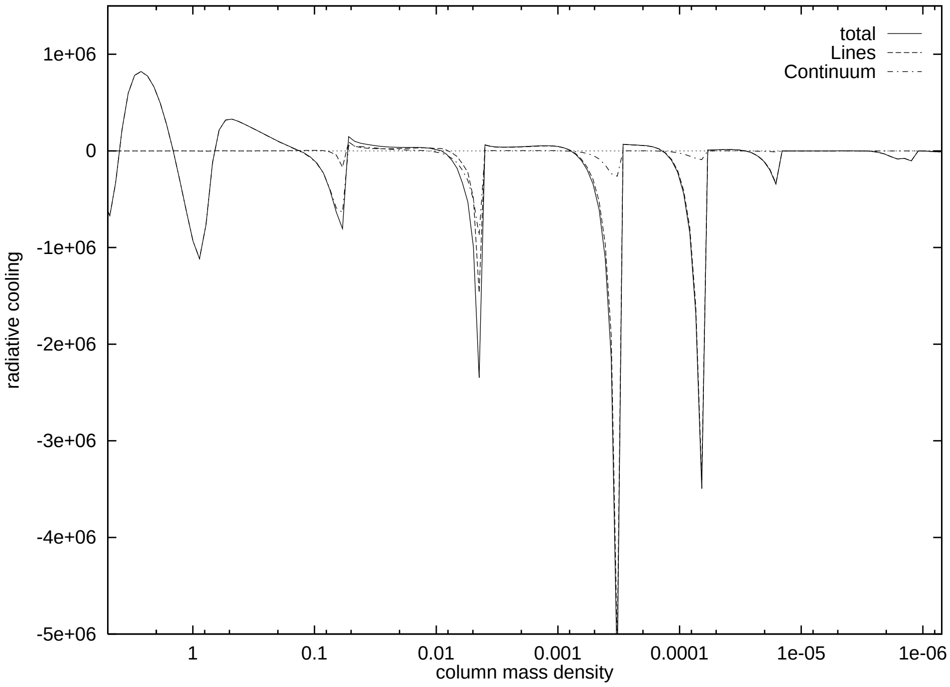

Figure 4.8: Radiative damping function D [erg g^{-1} K^{-1} sec^{-1}] vs. column mass density [g cm^{-2}] for the F5 V model at t=1123 sec.

As the maximally possible shock strength was found to be $\eta^{\max} = 3$, we see that equation (4.13) and the WST at best is applicable to waves with periods shorter than $\approx 0.6 \cdot P_{\rm ac}$. The shock strength increases with the wave period, thus equation (4.13) leads to unphysical limiting shock strengths for long period waves.

For our wave calculations we choose short period waves with $f = 0.2$. Equation (4.13) gives for this value of f a limiting strength of

$$\eta^{\rm lim}\Big|_{f=0.2} = 0.94 \quad . \tag{4.14}$$

From the calculations for the F5 V star we find a ratio of the densities at shocks of $\varrho_2/\varrho_1 = 1.86$ and the corresponding shock strength is $\eta = 0.86$, which is only about 10 percent less than $\eta^{\rm lim}$ as expected from WST.

This comparison, however, has to be taken with caution. As our atmospheres are non-isothermal, the actual ratio of the wave period P and the local cutoff period should be taken as value for f rather than $f = 0.2$, the latter only being valid at the top of the convection zone.

The second basic process affecting the propagation of acoustic waves in stellar chromospheres is the exchange of radiative energy. From Fig.(4.8) we identify several regions of the atmosphere by the main contributors to the radiative damping of acoustic waves. From the bottom of the atmosphere up to a column mass density $m = 0.09$ g cm^{-2}, corresponding to a geometrical height of 700 km, radiation of the H^--continuum dominates the radiative damping function D, while the contributions from spectral lines are negligible. It then follows a region for which lines and the continuum are equally important. In the overlying parts, starting at $m = 0.001$ g cm^{-2}, only line radiation is important. Here the hottest parts of the shock waves with temperatures exceeding $T \approx 5800K$ are cooled by line radiation. Cooling by H^- only plays a minor role for the upper half of the atmosphere. Near the top boundary of the chromosphere the opacity in the lines as well as in the continuum is so small that no further damping takes place and the waves propagate through an essentially adiabatic gas.

It is important to note that for the F5 V star the point of shock formation lies inside the region where H^- is the dominant emitter. The shocks are prevented from growing until they reach those regions where H^- is negligible. The F5 V star lies at the high temperature end

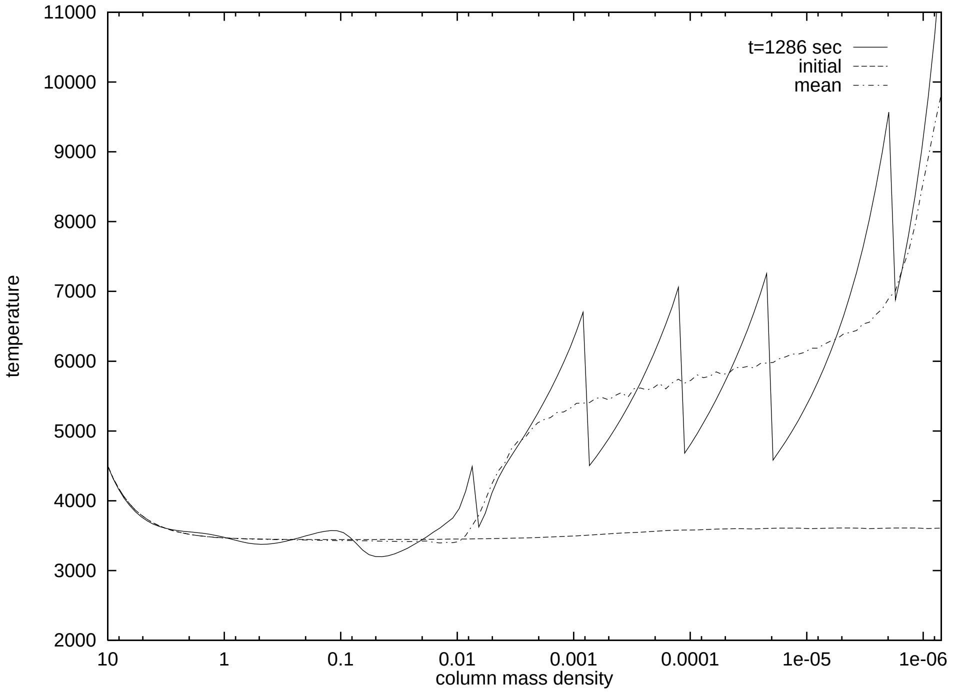

Figure 4.9: Temperature [K] vs. column mass density [g cm^{-2}] for the K5 V model. Shown are: temperature after 1286 sec, radiative equilibrium temperature structure, and mean chromospheric temperature structure.

of our sample of stellar models. We now look at the behavior of the cooler stars of spectral type K and later. As an example, Fig.(4.9) shows the temperature structure of a K5 V model star after $t = 1286$ sec. The wave period used for this star is $P = 26$ sec and 50 wave crests have entered the atmosphere at the instant shown here. The first difference to note is that, unlike in the F5 V star, the photospheric temperature structure of the K5 V star is almost unaltered by the acoustic waves. A similar result can be seen in Fig.(4.10) for the

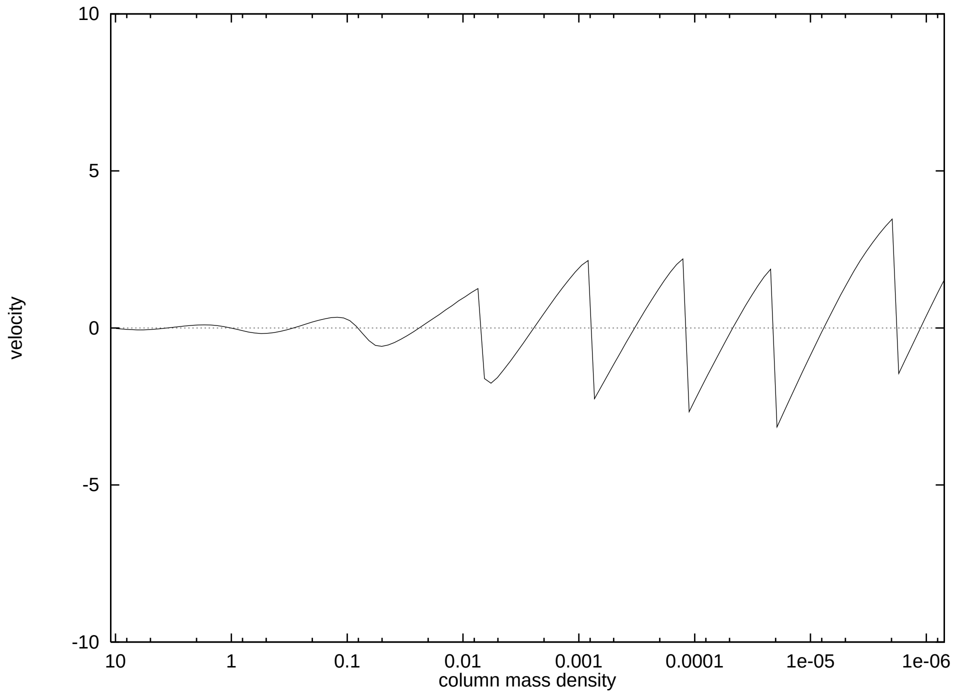

Figure 4.10: Gas velocity [km/sec] vs. column mass density [g cm^{-2}] at t=1286 sec for the K5 V model.

gas velocities, which hardly exceed 100 m/sec at photospheric levels. This is to be compared to the photospheric velocity variations of up to 2 km/sec found for the F5 V model.

The reason for these differences are both the higher photospheric gas density and the smaller acoustic wave flux of the K5 V star. From Table 4.1 we see, that the acoustic wave flux for the K5 V star is smaller by a factor of $\approx 1/57$ compared to the hotter F5 V model. The density at the bottom of the model for the K5 V star (the bottom of the atmosphere is defined by optical depth $\tau_{5000\ \mathring{A}} = 1.3$) is larger by an order of magnitude than that at the bottom of the F5 V star atmosphere. From Eq.(4.2) the wave amplitude expected for the K5 V star is only 0.08 times that for the F5 V star model.

Despite the presence of waves, the temperature structure of the photosphere of the K5 V star is very close to radiative equilibrium. Therefore, no considerable damping of the wave at photospheric levels takes place. This can be seen in Fig.(4.11), where noticeable cooling rates are only found for the shocks in the upper part of the atmosphere. As a consequence of the much smaller wave amplitude the point of shock formation is shifted farther out to $m = 0.01$ g cm^{-2}. The shocks reach a limiting strength of $\eta^{\rm lim} = 0.91$, a value slightly larger than for the hotter star.

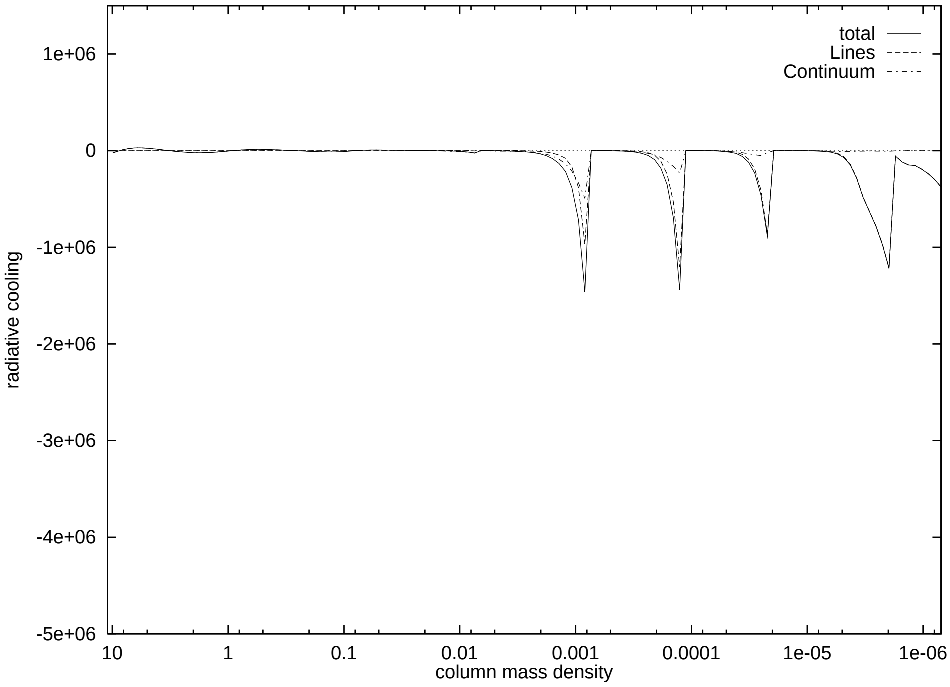

Figure 4.11: Radiative damping function D [erg g^{-1} K^{-1} sec^{-1}] vs. column mass density [g cm^{-2}] for the K5 V model at t=1286 sec.

4.3 The Radiative Damping Zone

The efficiency of acoustical flux transfer from the convection zone into the chromosphere is determined by the radiative damping in the photosphere. If D is large in photospheric regions, then only a small part of the initial flux reaches the chromosphere to produce the temperature inversion and the chromospheric emission. The radiative losses in the photosphere are dependent on the amplitude of the disturbances caused by the waves, on the opacities, and on the radiative equilibrium temperature. This can be seen by the following derivations. Using equation (3.75) we write the radiative damping as

$$D \equiv \left.\frac{\mathrm{d}s}{\mathrm{d}t}\right|_{\mathrm{rad}} = \frac{4\pi}{T}\int \kappa_\nu (J_\nu - S_\nu)\mathrm{d}\nu \tag{4.15}$$

with the total opacity per gram $\kappa_\nu = \chi_\nu/\varrho$. D vanishes if the atmosphere is in radiative equilibrium with $T(z) = T_0(z)$ everywhere. It is possible for D to be very small even for large departures from radiative equilibrium if the opacity is sufficiently small.

Let us assume for the moment that we have a gray case with frequency independent opacities, $\kappa_\nu = \kappa$. From equation (4.15) we then have

$$T\frac{\mathrm{d}s}{\mathrm{d}t} = 4\pi\kappa(J - S) \tag{4.16}$$

and assuming LTE, we can replace the source function S with the frequency integrated

Planck function,

$$S = B = \frac{\sigma T^4}{\pi} \tag{4.17}$$

Here J is the frequency integrated mean intensity. We denote the equilibrium values for temperature, density, entropy, etc with an index 0, and the perturbations caused by the wave are written as δT, $\delta \varrho$, δs, etc. The temperature of the perturbed atmosphere is then given by $T = T_0 + \delta T$, and we have similar expressions for the entropy and the density. Linearizing (4.16) leads to

$$T_0 \frac{d\delta s}{dt} = 4\pi\kappa_0(\delta J - \delta B) \quad . \tag{4.18}$$

If we make the optical thin approximation, J remains constant. Thus we have $\delta J = 0$ and the linearized energy exchange is

$$\begin{aligned} T_0 \frac{d}{dt}\delta s &= -16\sigma\kappa_0 T_0^3 \delta T \\ &= -c_v \cdot t_{\mathrm{rad}}^{-1} \cdot \delta T \end{aligned} \tag{4.19}$$

with the *radiative relaxation time* (Spiegel, 1957)

$$t_{\mathrm{rad}} = \frac{c_v}{16\sigma\kappa_0 T_0^3} \quad . \tag{4.20}$$

For non-gray radiation, linearization of equation (4.15) yields (Schmitz, 1989)

$$T_0 \frac{d}{dt}\delta S = 4\pi \left[\int_0^\infty \delta\kappa_\nu \left(J_{\nu\,0} - S_{\nu\,0}\right) d\nu - \int_0^\infty \kappa_{\nu\,0}\delta S_\nu \, d\nu \right] \quad , \tag{4.21}$$

where we again used the optical thin approximation with $J_\nu = J_{\nu,0}$ and $\delta J_\nu = 0$.

For our calculations, we assume pure H^--opacities for which the contribution of the free-free transitions is small compared to the contribution of the bound-free transitions: $\kappa_\nu^{\mathrm{ff}} \ll \kappa_\nu^{\mathrm{bf}}$. The bound-free absorption coefficient is given by equation (3.55). If we assume that the departures from LTE are negligible, we have $b_{H^-} = 1$ and the opacity per gram can be written as (Kurucz, 1973)

$$\kappa_\nu^{\mathrm{bf}}(T,p) = \alpha_\nu^{\mathrm{bf}} \cdot f(T,p) \left(1 - e^{-\frac{h\nu}{kT}}\right) \quad , \tag{4.22}$$

with a function $f(T,p)$ only dependent on temperature and pressure. We neglect the stimulated emission correction, $e^{-\frac{h\nu}{kT}}$, in (4.22) and write the equilibrium opacity in (4.21) approximately as (Schmitz, 1989)

$$\kappa_{\nu\,0} \approx \kappa_\nu^{\mathrm{bf}}(T_0, p_0) \approx \alpha_\nu^{\mathrm{bf}} \cdot f(T_0, p_0) \tag{4.23}$$

Using (4.23), the perturbation $\delta\kappa_\nu$ is approximated by

$$\begin{aligned} \delta\kappa_\nu &\approx \alpha_\nu^{\mathrm{bf}} \cdot \delta f(T,p) \\ &\approx \frac{\delta f(T,p)}{f(T_0,p_0)} \cdot \kappa_{\nu\,0} \quad . \end{aligned} \tag{4.24}$$

The first term of the r.h.s. in equation (4.21) vanishes because we can write

$$\int_0^\infty \delta\kappa_\nu \left(J_{\nu\,0} - S_{\nu\,0}\right)\,d\nu = \frac{\delta f}{f_0}\int_0^\infty \kappa_{\nu\,0}\left(J_{\nu\,0} - S_{\nu\,0}\right)\,d\nu \equiv 0 \tag{4.25}$$

with $f_0 \equiv f(T_0, p_0)$.

In our case of considering only H^-, the linearized expression of equation (4.15) is given as

$$T_0 \frac{d}{dt}\delta S = -4\pi \int_0^\infty \kappa_{\nu\,0}\delta S_\nu \,d\nu \quad . \tag{4.26}$$

The perturbation of the source function is then calculated as

$$\delta S_\nu = \left.\frac{\partial S_\nu}{\partial T}\right|_{T_0} \cdot \delta T \quad . \tag{4.27}$$

Using (4.27) in equation (4.26) and comparing to the results of the gray calculations, (equations (4.19) and (4.20)), one can identify (Schmitz, 1989)

$$\overline{\kappa_0} = \frac{\int_0^\infty \kappa_{\nu\,0}\left.\frac{\partial S_\nu}{\partial T}\right|_{T_0} d\nu}{\int_0^\infty \left.\frac{\partial S_\nu}{\partial T}\right|_{T_0} d\nu} \tag{4.28}$$

as the appropriate mean opacity to use for the determination of the radiative relaxation time t_{rad} in the non-gray case, if H^- is the dominant source of opacity.

So far our calculations have been made under the assumption of an optically thin medium. This assumption, however, is insufficient for the bottom of the atmosphere, as the piston producing the acoustic waves is located at the top of the convection zone, where $\tau \approx 1$. Spiegel (1957) gives a modification for the radiative relaxation time which reads

$$t_{\mathrm{rad}}^{-1} = \frac{16\sigma T_0^3 \overline{\kappa_0}}{c_v} g(\xi) \tag{4.29}$$

with $g(\xi) = 1 - \xi\ \mathrm{arccot}(\xi)$. The parameter ξ depends on the frequency of the wave and can be written as (Schmitz,1989)

$$\xi = \frac{\varrho_0 \overline{\kappa_0} c_s}{\omega} \quad . \tag{4.30}$$

In a recent paper of Zhugzda et al. (1993), the authors calculated the radiative relaxation time scale without using the Rosseland mean as

$$t_{\mathrm{rad}}^{-1} = \frac{16\sigma\, T_0^3}{c_v} \frac{\int_0^\infty \kappa_\nu \frac{\partial S_\nu}{\partial T}(1 - \xi_\nu\ \mathrm{arccot}\xi_\nu)\,d\nu}{\int_0^\infty \left.\frac{\partial S_\nu}{\partial T}\right|_{T_0} d\nu} \tag{4.31}$$

with $\xi_\nu = \frac{\varrho_0 \kappa_\nu c_s}{\omega}$. Their results differ from those obtained with the Rosseland type mean used in our calculations by less than 10 percent.

Radiative damping of waves with period P is efficient, if the ratio $\mathcal{E} = \frac{P}{t_{\rm rad}} \geq 1$. During one wave period radiation damping decreases the wave flux like $F_{\rm M} \sim \exp(-\mathcal{E})$ (Ulmschneider 1988), leading to a considerable loss of mechanical flux for $\mathcal{E}$. For values of $\mathcal{E}$ smaller than unity the effect of radiative damping quickly becomes less important. If we denote the atmospheric region with a damping efficiency $\mathcal{E}$ greater than unity as the *radiative damping zone* (Ulmschneider et al.,1978; Schmitz and Ulmschneider, 1981) we can classify the stars according to the extension of their damping zones. In Fig.(4.12) we compare the extensions

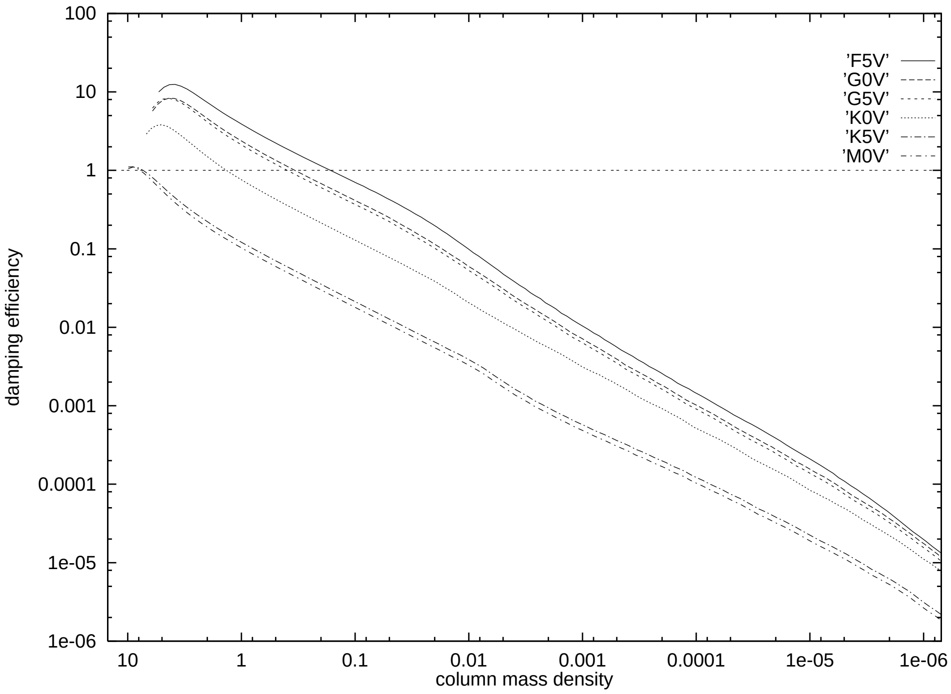

Figure 4.12: Radiative damping efficiency $\mathcal{E}$ vs. column mass density m [g cm^{-2}] for the time averaged stellar models.

of the radiative damping zones for the different stellar models. The main sequence stars can be separated into two classes with different damping properties. The later type stars up to K5 V do not suffer from radiative damping as their damping zones are negligible. From K0 V on towards the earlier stellar types, the radiative damping zone extends over a significant part of the photosphere. The acoustic waves suffer from large damping and the wave flux is significantly reduced.

We can use equation (4.19) to express the radiative damping function as

$$D = -16\sigma\overline{\kappa_0}g(\xi)T_0^2\;\delta T = c_v\;t_{\rm rad}^{-1}\;\frac{\delta T}{T_0} \quad . \tag{4.32}$$

Equation (4.32) allows us to estimate the behavior of the radiative damping function for our sample of stars. For given opacity and frequency of the waves, those stars with the higher equilibrium temperature and the larger temperature fluctuations will have stronger damping. For a given temperature fluctuation, the hotter stars will radiate away the excess energy much more efficiently than cooler stars. We therefore can expect the efficiency of acoustic energy transfer from the convection zone through the photosphere into the chromosphere to be larger for the stars at the cool end of the HRD. For stars of spectral type K5 V and later, a larger fraction of the mechanical flux will reach the chromosphere than for the earlier types.

4.4 Chromospheric Line Emission

Chromospheric line emission is calculated for the MgII k and CaII K line for each time step of the time-dependent wave calculation. For a determination of the energy losses caused by spectral line radiation, the emissions are calculated under the approximation of *complete redistribution* (CRD). In this approximation, emission and absorption profiles are identical. It is known from observations, that CRD does not produce the observed shapes of the chromospheric lines. Better results are achieved if *partial redistribution* (PRD) is assumed, where the fact is taken into account that in the line wings there is coherent scattering, and complete redistribution essentially occurs only in the Doppler cores of the lines. In PRD the emission and absorption profiles are no longer taken to be identical. This results in a reduction of the line wings compared to the results of CRD, where photons absorbed in the line center are permitted to leak out through the far line wings, thus allowing for an enhanced energy loss.

For the computation of the time dependent radiation losses CRD is used to artificially enhance the emissions of one single line, the MgII k line, in order to give a crude estimate of the total radiation losses in the middle chromosphere. Yet the computation of the true line shapes of MgII k and CaII K generated by our models, requires the usage of PRD to get realistic results which can be compared with the observations.

Examples of the line emission from CaII and MgII are shown in Figs. (4.13) and (4.14). For the F5 V model the emerging line profiles at t=994 sec both in PRD and CRD of MgII k and CaII K are depicted, each with the corresponding profile of the radiative equilibrium atmosphere.

To save computer time and memory, the calculations for the PRD profiles are performed for the inner parts of the line only. This is possible because the contributions of the line wings are greatly reduced for PRD as compared to CRD, as can be seen from Figs. (4.13) and (4.14). The intensities are given in erg cm^{-2} sec^{-1} sr^{-1} Hz^{-1} and plotted as functions of the wavelength displacement from the line center. Both lines show the characteristic appearance of chromospheric emission line cores.

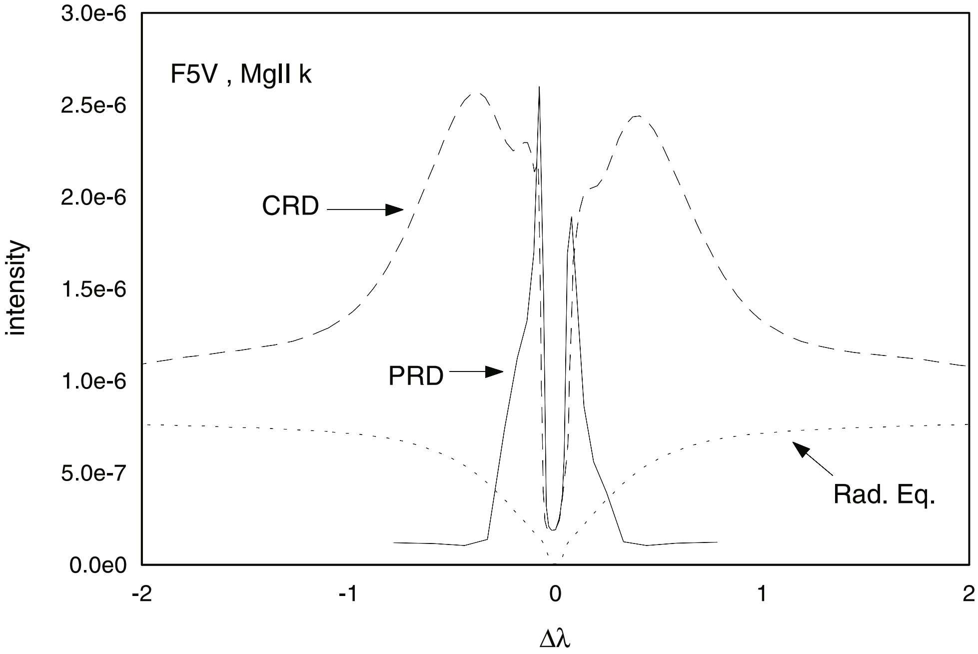

Figure 4.13: Emerging MgII k line profile at t=994 sec. Intensity (erg cm^{-2} sec^{-1} sr^{-1} Hz^{-1}) vs. displacement $\Delta\lambda$ [Å] from the line center at $\lambda_0 = 2796$ Å

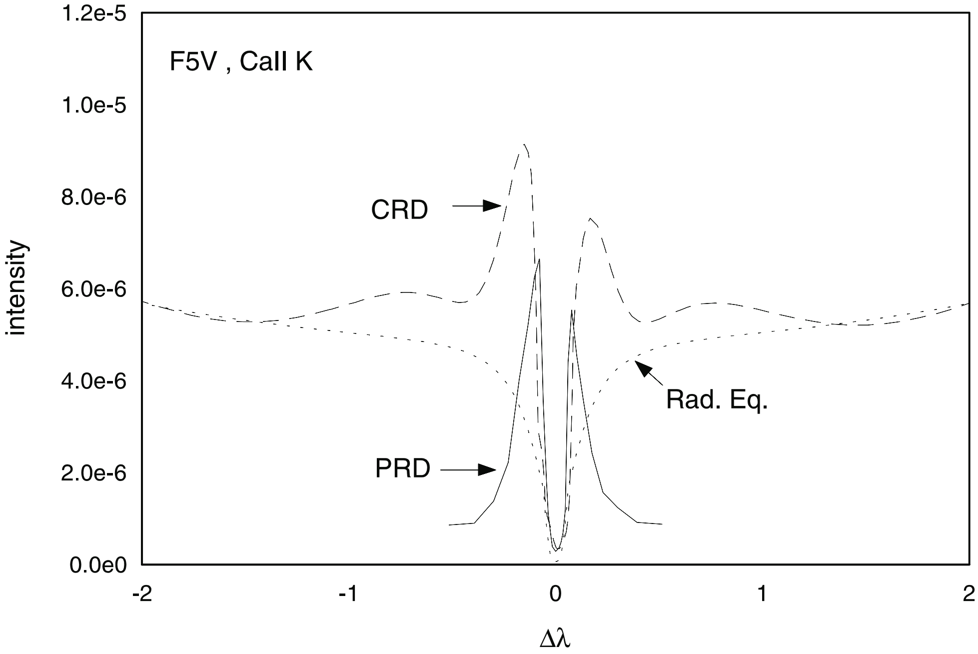

Figure 4.14: Emerging CaII K line profile at t=994 sec. Intensity erg cm^{-2} sec^{-1} sr^{-1} Hz^{-1} vs. displacement $\Delta\lambda$[Å] from the line center at $\lambda_0 = 3933$Å

Comparing the CRD profiles of both lines with those resulting from the PRD calculations, one notes that the emission cores in PRD are narrower for both lines. The broad emission cores found in CRD are a result of the above mentioned possibility for photons to escape through the line wings, thus enhancing the wing intensities. In PRD these photons are trapped in the line core and cannot escape because of the large optical depth.

Again as in the preceding section, we compare the results found for the F5 V model with those from the K5 V to describe the systematic changes as one moves along the main sequence of the HRD. We show in Figs.(4.15) and (4.16) the emerging intensity profiles for both diagnostic lines as they result from the K5 V model atmosphere at t=590 sec. The first point to note is the difference in the wavelength scale of the two plots. Both CRD and PRD profiles are much broader for the F5 V model than for the K5 V star. Due to the different surface temperatures of the stars , the rest intensity seen in the line wings of the pure absorption profiles of the initial radiative equilibrium models is different in both stars because of the temperature dependence of the Planck function. The differences observed for the radiative equilibrium profiles of the two lines for *one* star are due to the frequency dependence of the Planck function. The line profiles in CRD and PRD are not very different

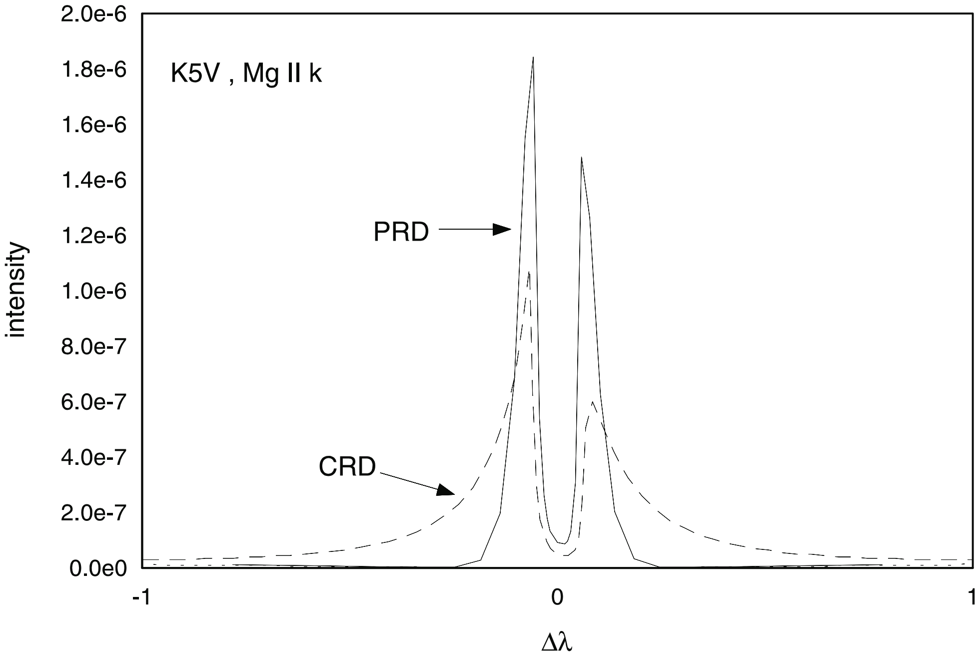

Figure 4.15: Emerging MgII k line profile at t=590 sec. Intensity erg cm^{-2} sec^{-1} sr^{-1} Hz^{-1} vs. displacement $\Delta\lambda$[Å] from the line center at $\lambda_0 = 2796$Å

for the K5 V star, whereas the profiles for the F5 V star show broad line wings in CRD which are not present in the PRD profile. This difference is caused by the different number

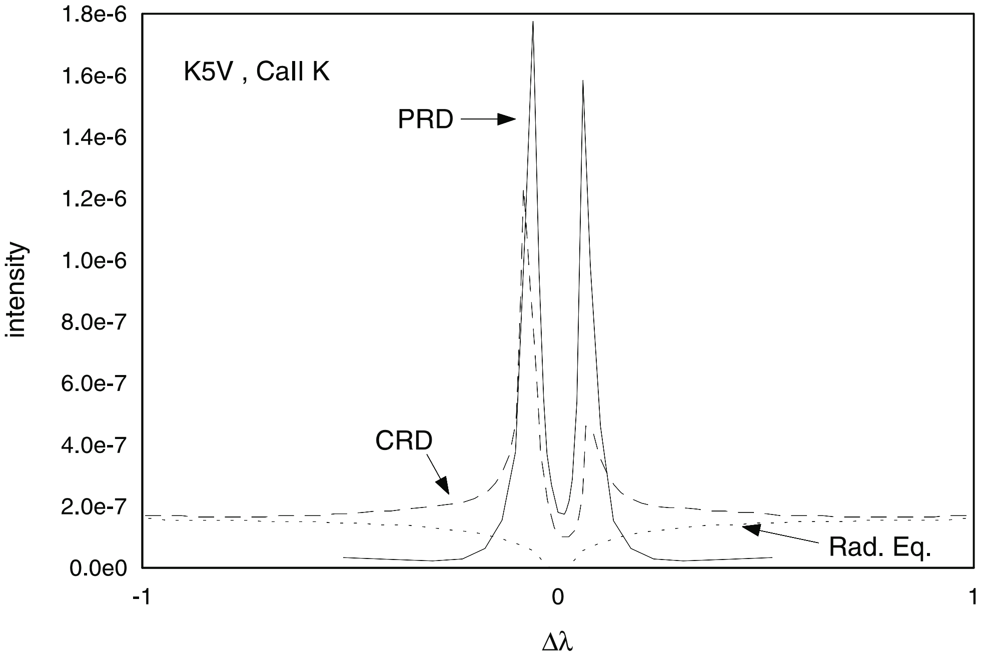

Figure 4.16: Emerging CaII k line profile at t=590 sec. Intensity erg cm^{-2} sec^{-1} sr^{-1} Hz^{-1} vs. displacement $\Delta\lambda$[Å] from the line center at $\lambda_0 = 3933$Å

densities of CaII and MgII in the line forming regions of both stars. For the K5 V star the number densities in the line forming region are low, and only the line cores are optically thick. The consideration of coherent scattering in PRD only affects the line wings and the differences between CRD and PRD become small in the K5 V star.

The physical conditions in the line forming regions undergo large variations with time. The temperature enhancement occurring when a shock runs through the emitting gas is accompanied by changes in magnitude and direction of the gas motions. This results in large variations with time of the line profiles. Examples for this behavior can be found in the Figs.(4.17) and (4.18) where the time variations for the MgII k line in CRD and PRD are shown. The peak intensities vary by a factor of about 1.5 over one wave period but the width of the lines does not change much. Note that all line profiles are computed without assuming additional broadening by microturbulence. The line width of the MgII k line for the F5 V star is $W_{\rm Mg} = 0.5$Å and for the K5 V star we find $W_{\rm Mg} = 0.2$Å.

4.5 The Basal Flux Line

The variations with time resulting from the dynamics of the atmosphere cannot be observationally resolved for stars other than the sun. Photometric or spectroscopic observations integrate the infalling light over the exposure time, thus losing the information on short

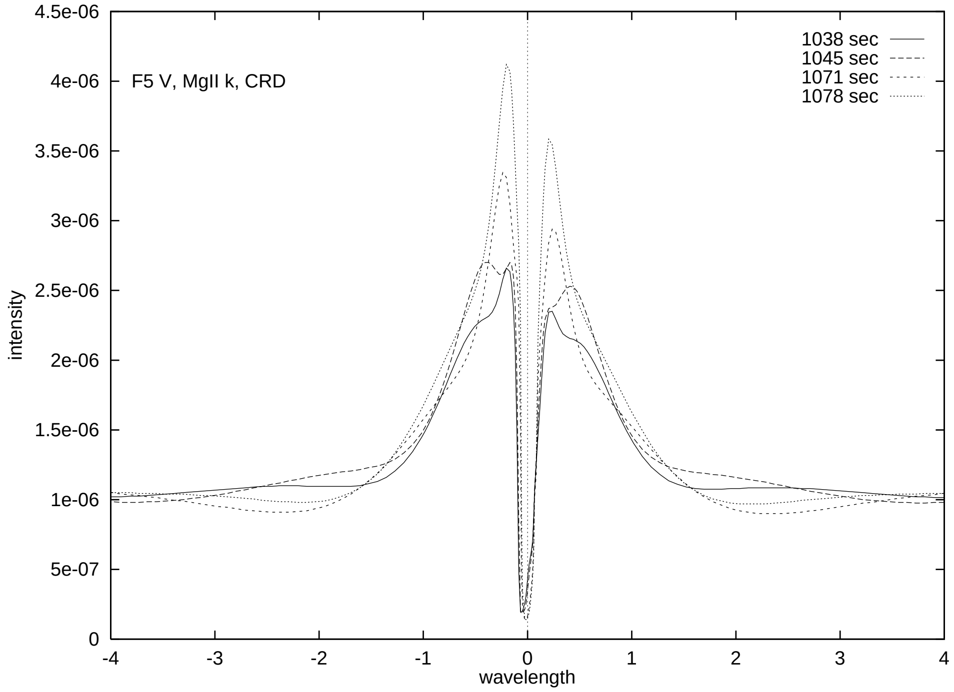

Figure 4.17: Intensity variations with time for the MgII k line (CRD) from F5 V. Intensity erg cm^{-2} sec^{-1} sr^{-1} Hz^{-1} vs. displacement $\Delta\lambda$[Å] from the line center at $\lambda_0 = 2796$Å

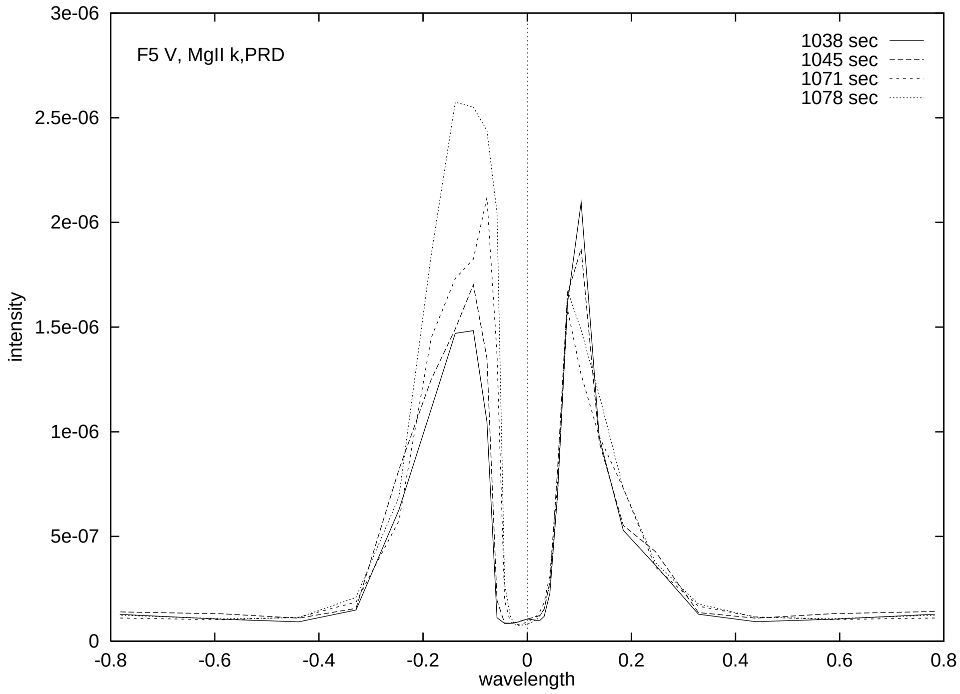

Figure 4.18: Intensity variations with time for the MgII k line (PRD) from F5 V. Intensity erg cm^{-2} sec^{-1} sr^{-1} Hz^{-1} vs. displacement $\Delta\lambda$[Å] from the line center at $\lambda_0 = 2796$Å

time variations. To compare our results with those observations, we average the calculated line profiles over a time interval to get the mean chromospheric emission.

Schrijver (1987) and Rutten et al. (1991) presented a detailed statistical analysis of flux-flux and flux-color relations derived from selected emission lines for a large sample of late-type stars. The statistical correlations found for these relations can best be understood when the stellar emission line fluxes are assumed to consist of a *basal* flux, which is independent on magnetic activity, and a *magnetic* component depending on rotation and age of the star.

The existence of a lower limit in the chromospheric emissions in CaII H+K and MgII h+k as well as in several other lines could be identified as an intrinsic property of the stars and is not an artifact of detection limits. The most probable mechanism to explain the observational results, is heating by acoustic waves. We therefore compare the results of our averaging procedure to those of Rutten et al.(1991).

From each stellar model we calculate the emergent line profiles of MgII k and CaII K for a large number of time-steps both in CRD and PRD. As shown in Figure (4.18) the emerging profiles vary with the phase of the wave. We then integrate the emission cores over wavelength between the k1 and K1 minima to obtain the total emergent intensities I^+_{Mg} and I^+_{Ca}. In the two-beam approximation the total flux is then given by

$$F = 2\pi \; \mu \; I^+ \tag{4.33}$$

with the angle cosine $\mu = 1/\sqrt{3}$. We now average the fluxes over time to get the mean chromospheric emission flux in CaII K and MgII k.

The fluxes for CaII and Mg II given by Rutten et al. are essentially CaII H+K and MgII h+k fluxes. In order to compare our results with the observations, we multiply the fluxes by a factor of 2 to estimate the total emission flux of MgII h+k and CaII H+K. This factor would be correct, if both lines were optically thick. In the optically thin case, a factor of 1.5 would be appropriate. So our choice results in an upper limit of the mean chromospheric line emission from acoustically heated chromospheres.

Additional care has to be taken to compare our CaII results with the observations. The data used by Rutten et al. for CaII H+K are taken with the Mount Wilson HK photometer (see Duncan et al. 1991). The original data contain not only the net emission flux from the emission peaks in both lines but also a significant contribution by photospheric radiation.

The data for CaII given by Rutten at al. (1991) are corrected for the photospheric contributions. We do a similar correction by subtracting the equilibrium flux F_0 from the time averaged total emission flux.

For magnesium no correction has been applied because photospheric contributions are negligible. We show our results for the time averaged emission fluxes as obtained from our hydrodynamic calculations in Table (4.2). We calculate mean emissions for CRD as well as

Star	B - V	log F_{mean}			
		CaII CRD	CaII PRD	MgII CRD	MgII PRD
F5 V	0.44	6.6	6.5	7.3	6.1
G0 V	0.58	6.4	6.1	7.5	5.9
G5 V	0.68	6.5	6.2	7.0	5.6
K0 V	0.81	5.9	5.4	6.5	5.3
K5 V	1.15	5.1	4.8	5.8	5.2
M0 V	1.40	4.4	4.3	4.6	4.8

Table 4.2: Mean chromospheric net emission for CaII H+K and MgII h+k.

for PRD. In order to compare our resulting emission fluxes directly with the observational results, we show in Fig.(4.19) the observational results of Rutten et al.(1991) together with our theoretical results. The fluxes obtained for CaII in PRD and CRD are close together, with PRD yielding the smaller results. The differences are between 0.1 and 0.5 of the logarithmic values.

Using PRD has a more dramatic impact on the MgII fluxes. The results are smaller by more than an order of magnitude. The only exception is found for the coolest star in the sample, the M0 V. Here the PRD emissions are slightly larger than those obtained assuming CRD. The CRD results are given as $+-$ signs and the PRD results as crosses. Whereas the CaII basal flux line is reproduced both for CRD and PRD, only the PRD results match with the empirical lower limits of MgII fluxes. This emphasizes the need for a careful treatment of PRD effects on spectral lines.

The close correspondence of our theoretical results with the observed basal flux line gives strong evidence that indeed acoustic waves are the basic heating mechanism of chromospheres. Despite the obvious limitations of our calculations, where monochromatic waves instead of acoustic spectra have been used, and where the radiative energy losses of spectral lines have been approximated by one single line, we think the above result shows strong evidence that acoustic heating is present and important in all late-type stars.

When we compare the total energy flux emitted by MgII h+k and Ca II H+K, we see that the fraction of the input acoustic flux which is visible as chromospheric line emission increases with (B-V). While a star of spectral type F has an total chromospheric emission flux $F_{\rm Ca+Mg}$ which is as small as $1/150 \times F_{\rm M}$, a star of spectral type M has an chromospheric emission flux which is $1/20 \times F_{\rm M}$ (see Fig. (4.20) and Tables (4.1) and (4.2)). The efficiency of acoustic heating increases with increasing (B-V).

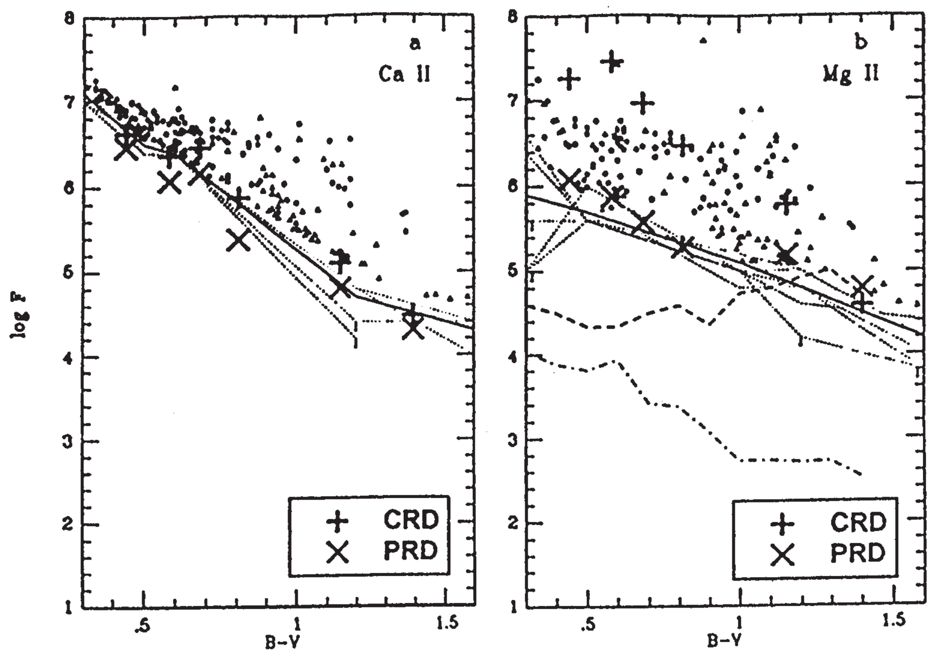

Figure 4.19: Theoretical emission fluxes compared with empirical fluxes (after Rutten et al. (1991), see also Chapter 1). Our results are shown as + signs (CRD) and crosses (PRD).

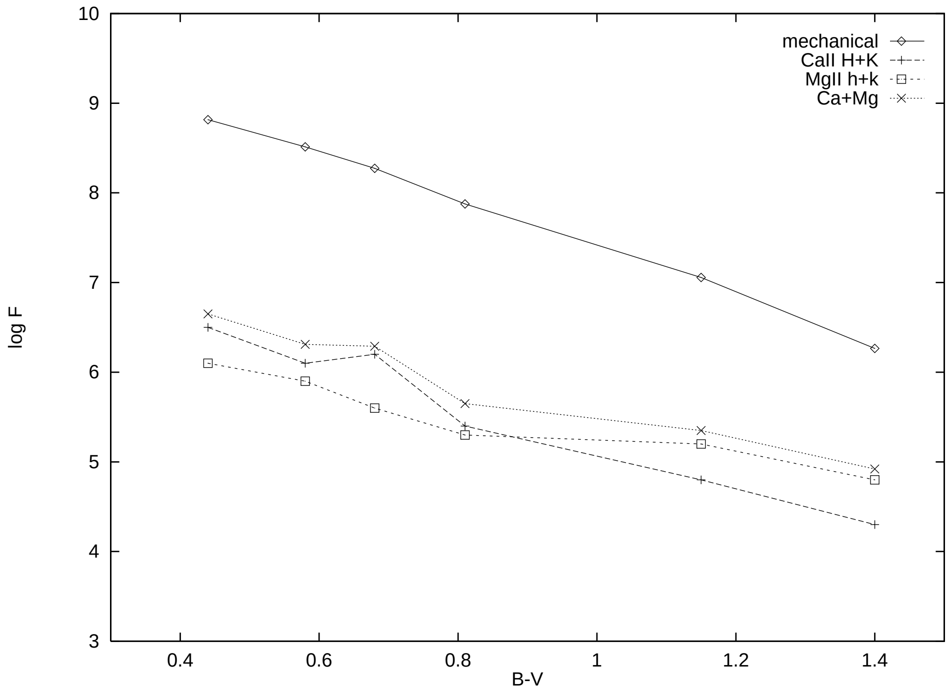

Figure 4.20: Comparison of the chromospheric emission fluxes with the acoustic input flux.

4.6 Properties of Time Averaged Chromospheres

In this section we study the properties of the time averaged chromospheric models. After a sufficient computational time a dynamical equilibrium state is reached in our time dependent calculations. Usually we have to wait until about 20 to 25 wave crests have passed through the atmosphere. The physical variables at each height are then averaged over a time interval long enough to include several wave periods.

The resulting time averaged model will not show the large variations of the time-dependent chromospheric models, but resemble the more smooth structures usually resulting from semi-empirical chromospheric modeling. We then can use this model to check to what extent results from semi-empirical modeling can be reproduced as properties of the time averaged model.

Fig.(4.21) shows the mean temperatures for our sample of stars. As functions of the column mass density m [g cm^{-2}] the figure displays the mean chromospheric temperatures together with the initial radiative equilibrium temperatures. The time-dependent models

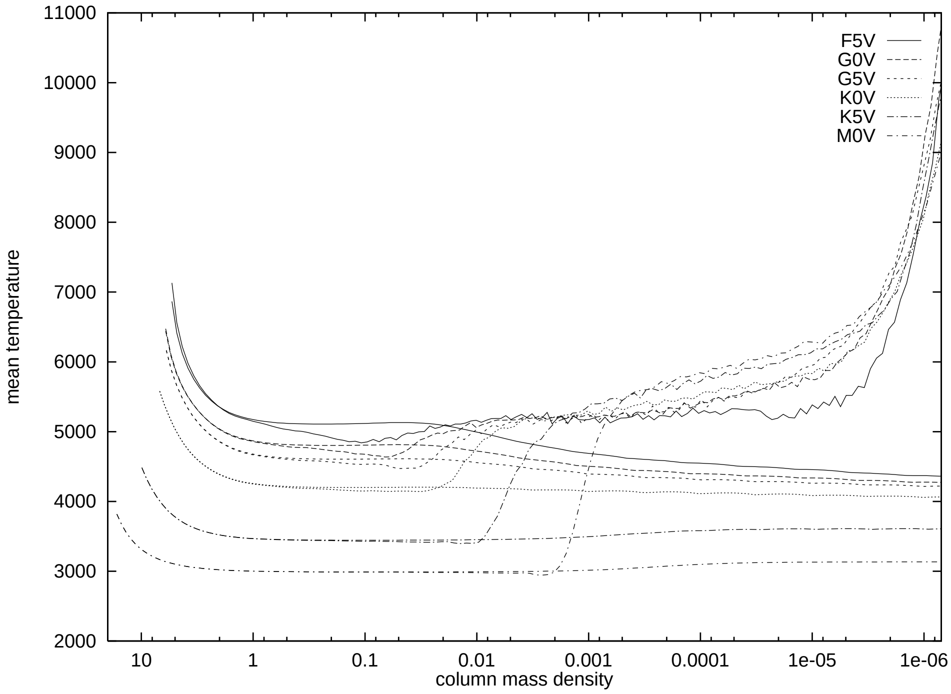

Figure 4.21: Mean chromospheric temperature and initial radiative equilibrium temperature [K] vs. column mass density [g cm^{-2}]

have been averaged over several wave periods to smooth the effects of the acoustic waves and shocks. The averaging procedure starts at a time step where the equilibrium is reached. The residual velocities do not cancel entirely, as is depicted in Fig. (4.22). With the exception of the F5 V star, where the signature of the pulsating atmosphere still is apparent, the remaining velocities are small. We therefore assume that all models have reached their final state, which is characterized by the balance between shock heating and radiative cooling. Comparing the mean chromospheres, one notes that all models show a temperature plateau

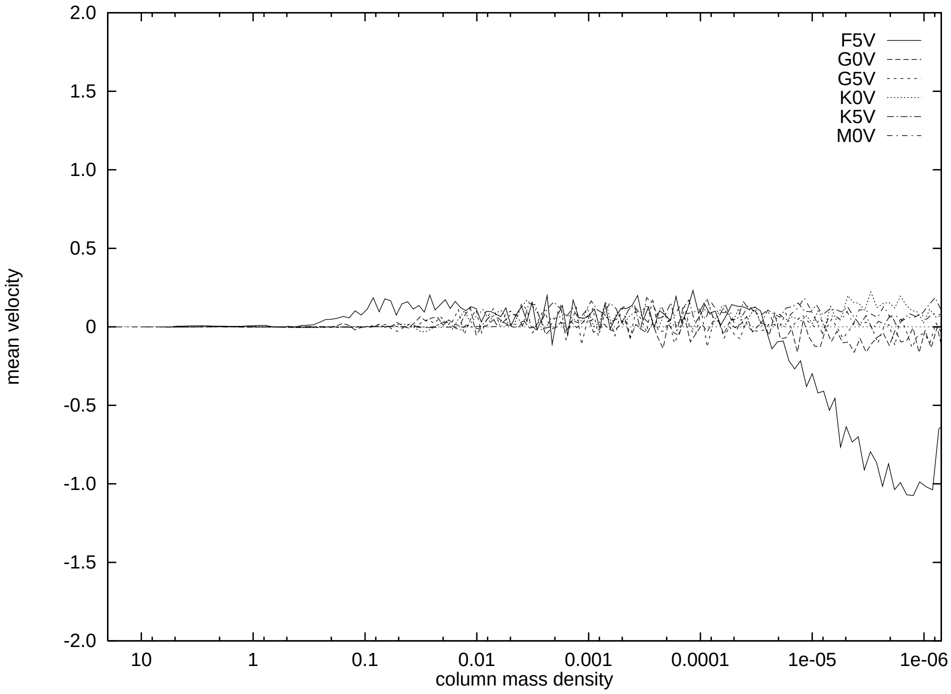

Figure 4.22: Mean velocities [cm $\sec^{-1}$] vs. column mass density for the time averaged models.

with temperatures in the region around $T = 5500$K. The plateau temperature is lowest for the F5 V star, where it is found to be only 5200 K. The highest temperature is reached by the model of the M0 V star with a mean temperature between $\log m = -3$ and $\log m = -5$ of 6000 K. The chromospheric temperature rise steepens with decreasing $T_{\rm eff}$ and is located at smaller column mass densities.

This behavior is caused by the differences in the mechanical input flux, wave amplitudes and the different efficiency of radiative cooling. The F5 V star with a flux of $F_{\rm M} = 6.6 \cdot 10^8$ erg cm^{-2} sec^{-1} has its point of shock formation at a larger density than the M0 V star where much smaller wave amplitudes form shocks in larger heights. Thus the chromospheric temperature enhancement starts at larger mass column densities for the hotter star. As the shocks form in a region where the F5 V star has large radiative cooling by H^-, the temperature increases more slowly than in the M0 V star, where the sudden temperature rise is not counterbalanced by radiative damping until line radiation starts its strong contributions.

The chromospheric temperature enhancement in the outer regions of the atmospheres is accompanied by a temperature depression around the point of shock formation and just before the temperature inversion starts. The mean temperature is depressed below the radiative equilibrium temperature despite the fact that the propagating waves provide additional energy. This effect has been described earlier (Ulmschneider et al. 1978, Kalkofen,Ulmschneider and Schmitz, 1984) and is due to the nonlinearity of the Planck function with respect to the temperature. For sufficiently large wave amplitudes the temperature fluctuations δT are large. The actual temperature T is the sum of the mean temperature $\overline{T}$ and the temperature fluctuation:

$$T = \overline{T} + \delta T \tag{4.34}$$

The temperature of the radiative equilibrium atmosphere T_0 can be used to write the energy balance as (Kalkofen, Ulmschneider and Schmitz ,1984)

$$T_0^4 = \overline{T}^4 \cdot \left[1 + 4\frac{\delta T}{\overline{T}} + 6\left(\frac{\delta T}{\overline{T}}\right)^2 + \ldots\right] \tag{4.35}$$

The additional wave flux is only a small fraction of the total radiative flux. Therefore we can assume that T_0^4 will be essentially unaltered by the wave and to compensate the effects of a large temperature amplitude, the mean temperature $\overline{T}$ has to decrease. In terms of the radiative energy exchange one can say that the excess emission which occurs for the cases with $\delta T > 0$ is not balanced by additional radiative heating which occurs for $\delta T < 0$. This effect is dependent on the amplitudes of the temperature fluctuations and thus the M0 V star, having a much smaller wave amplitude, also shows a much smaller temperature depression.

An extreme case of such a temperature depression is found for a star of spectral type F0 V. This star has not been included in the former discussions because of some difficulties encountered during the model calculations.

With an effective temperature of $T_{\rm eff} = 7200$K, this star is the hottest star of the sample. The flux used for the calculations is $F_{\rm M} = 1.2 \cdot 10^9$ erg cm^{-2} sec^{-1}. The temperature fluctuations are extremely large with values of $2\delta T \approx 2000K$. Due to these large fluctuations the mean temperature is depressed below the radiative equilibrium temperature by 1000 K. The temperature depression extends for more than two orders of magnitude in m

Fig.(4.23) shows the mean atmospheric temperature together with the radiative temperature structure and a snapshot after t=720 sec. The striking result is that almost the entire mean atmosphere has a temperature that lies below the radiative equilibrium temperature. Only for the outermost parts of the model atmosphere a temperature enhancement is found. As the wave period is $P = 60$ sec only 12 wave crests have entered the atmosphere at the time shown. Thus it is clear that the final equilibrium state has not yet been reached.

Nevertheless, the mean chromospheric emission calculated for MgII h+k in PRD is $\log F_{MgII} = 6.2$ and thus is consistent with the basal flux line as shown in the preceding section. A semi-empirical model producing the emission flux of the time-dependent model would need a temperature enhancement similar to those in the other models. It is therefore

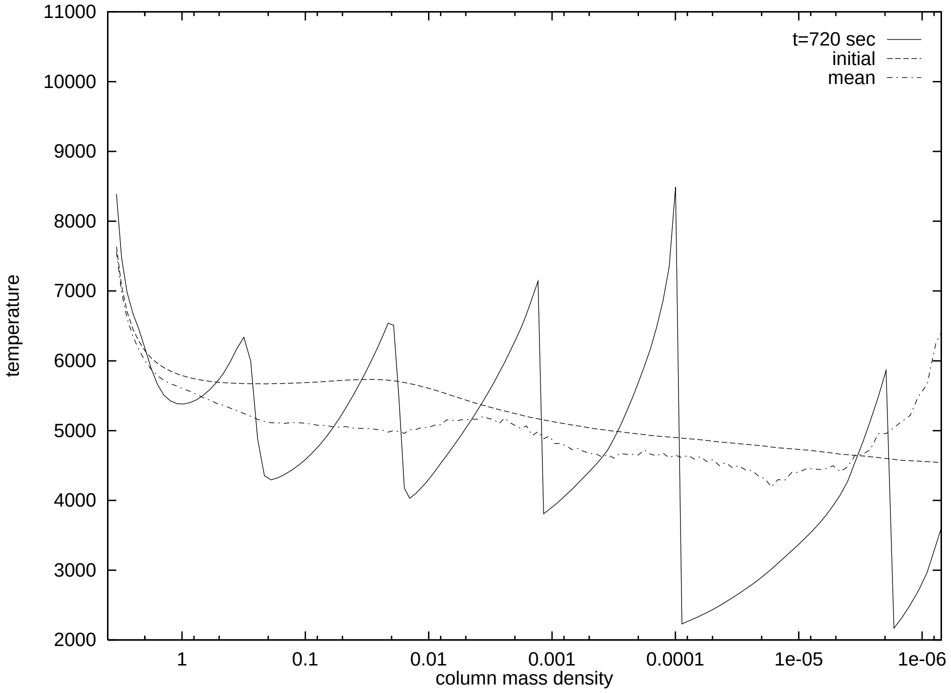

Figure 4.23: Temperature [K] vs. mass column density [g cm^{-2}] for the F0 V model. Shown are: temperature after 750 sec, initial radiative equilibrium temperature, and mean chromospheric temperature

not possible to simply interpret the occurrence of a chromospheric line emission as the result of an enhanced *mean* temperature in the emitting regions. The emission regions are highly variable with time. Enhanced emission occurs when a shock propagates through the line forming region. After the shock has passed, the temperature decreases again resulting in a reduction of line emissions. Thus the time mean of the emissions is dominated by the short phases of greatly enhanced temperatures.

In view of this result, we can state that the "chromosphere" which is observed in the emission cores of the MgII h+k and CaII H+K lines consists of hot regions behind shocks and is not related to a mean temperature enhancement.

However, a temperature enhancement of the mean atmosphere is indeed found in most of our models and we can examine whether the positions of the initial temperature rise (or temperature minimum) found from our models can be related to stellar parameters.

Ayres (1979) derived a simple scaling law connecting the position of the column mass density of the temperature minimum, m_*, with g and $T_{\rm eff}$ of the stars considered. Applied to stars of solar chemical composition and without magnetic activity, he found the simple relation

$$m_* \sim A \qquad \text{where } A = \left(\frac{g}{g_\odot}\right)^{-\frac{1}{2}} \left(\frac{T_{\text{eff}}}{T_{\text{eff},\odot}}\right)^{\frac{7}{2}} \quad . \tag{4.36}$$

To derive this relation, Ayres (1979) did not use a specified heating mechanism but assumed, that the temperature enhancement starts where the strong cooling effects of H^- vanish. Figure (4.24) shows that indeed a linear relation between m_* and A is found from our mean chromospheric models. The constant of proportionality found from Fig. (4.24) for our

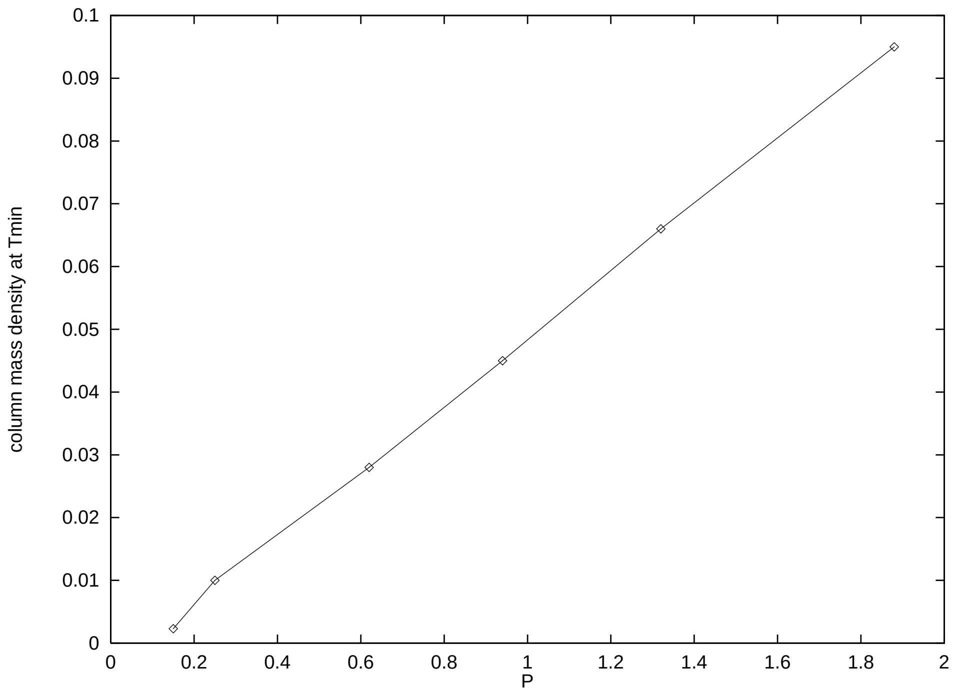

Figure 4.24: Column mass density m_* vs. the scaling parameter A

chromospheric models is ≈ 0.05 g cm^{-2} in good agreement with the value of 0.046 g cm^{-2} which can be derived using observational results for Procyon and the sun, as given in Ayres and Linsky (1975).

4.7 Theoretical Cooling Rates

Once the chromospheres have reached their final equilibrium state, the mean chromospheric heating rate is exactly balanced by the mean radiative cooling rate. The resulting time averaged cooling rate $\overline{\Phi}$ then also gives the height dependence of the time averaged heating rates caused by the shock waves. Figure.(4.25) shows the time averaged values of the cooling rate per gram [erg sec^{-1} g^{-1}] for the main sequence stars. In the radiative damping zone at the bottom of the atmosphere the heating rates are different for the different stars. This is due to the different temperature fluctuations and the resulting differences in the damping function D. The onset of the chromospheric temperature inversion is characterized by the sudden rise in the cooling rates (and heating rates) which starts at the temperature minimum. After the temperature plateau is reached, the heating becomes constant with height and is almost equal for all stars, despite of the large differences of the input mechanical fluxes F_{M}. We find a constant heating rate of $\approx 3 \cdot 10^9$ erg g^{-1} sec^{-1}. The constancy of the

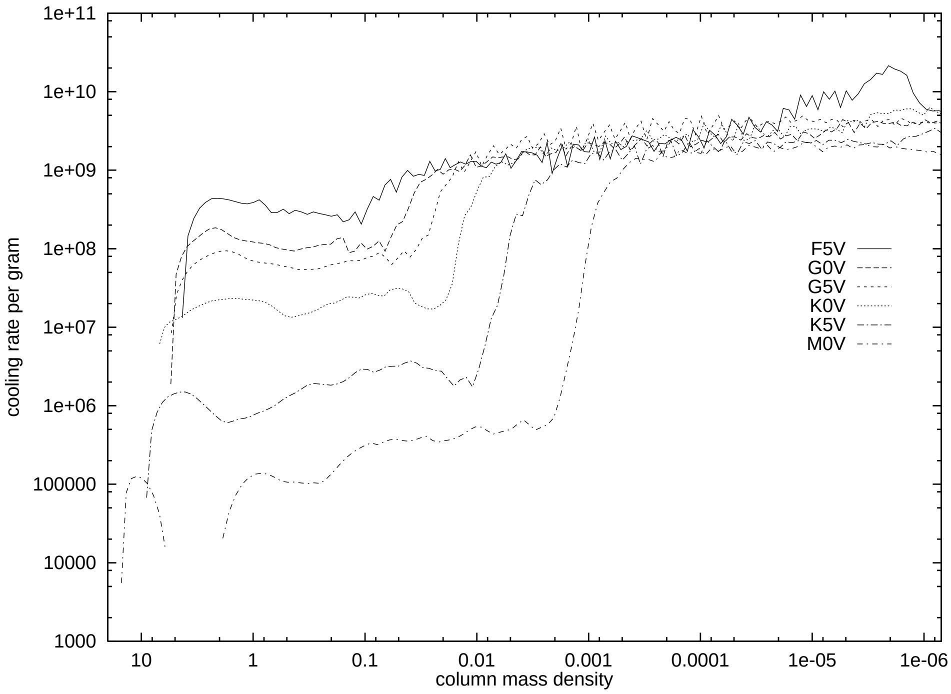

Figure 4.25: Time averaged cooling rate per gram [erg sec^{-1} g^{-1}] vs. mass column density [g cm^{-2}]

heating in the temperature plateau can be explained as a result of the limiting shock strength behavior.

The mechanical flux of a shock wave with sawtooth structure can be written as (Ulmschneider,1990)

$$F_{\mathrm{M}} \approx \frac{1}{12} \gamma p_0 \; c_s \eta^2 \tag{4.37}$$

with the shock strength η and p_0 is the unperturbed pressure. The change of the mechanical flux with height z, which gives the heating, can be written as

$$\frac{\mathrm{d}F_{\mathrm{M}}}{\mathrm{d}z} = \frac{1}{12} \frac{(\gamma+1)\gamma}{P} \; p_0 \; \eta^3 \approx -\frac{F_{\mathrm{M}}}{L_A} \tag{4.38}$$

with the *acoustic damping length*

$$L_A = \left(\frac{\gamma \; p_0 \; c_s^2}{12(\gamma+1)^2} \right)^{1/2} \; F_{\mathrm{M}}^{-1/2} \; P = \frac{c_s \; P}{(\gamma+1)\eta} \tag{4.39}$$

which depends on the wave period P. In case of shocks with limiting strength, η^{lim} according to equation (4.11), and our choice of $P = 0.2 \cdot P_{\mathrm{ac}} = 0.2 \cdot \frac{4\pi c_s}{\gamma g}$, the shock heating rate per gram can then be written as

$$\frac{\mathrm{d}F_{\mathrm{M}}}{\varrho \mathrm{d}z} \approx \frac{4\pi^2}{75} \frac{\gamma}{(\gamma+1)^2} c_s g \tag{4.40}$$

For our stellar models we find from equation (4.40) typical heating rates per gram of $2.4 \cdot 10^9$ erg g^{-1} sec^{-1}. This value is consistent with the results of our numerical simulations.

The constancy of the heating rate per gram which follows naturally from the assumption of heating by shocks with limiting strength, is empirically found for the sun (Anderson and Athay 1989), but the value derived from the semi-empirical model of the solar chromosphere is larger by a factor of ≈ 1.5. The reason for this difference is the fact, that Anderson and Athay (1989) added cooling by lines of the Fe group elements to their models which results in a larger cooling, which must be balanced by additional heating. In our models a greater heating rate could be produced by using larger wave periods as the limiting shock strength dependents on the wave period.

4.8 Theoretical Chromospheres for Giants

The surface gravity of main sequence stars compared to that of giants does not vary much. To examine the dependence on g of the chromospheric properties, we have to look therefore at stars with very different values of g. For this reason, two models for giants have been calculated. We choose a model for a K0III giant with $T_{\mathrm{eff}} = 4750$K and $\log g = 2.13$ and a model for a K5III star with $T_{\mathrm{eff}} = 3950$K and $\log g = 1.74$. For both stars we took the mechanical input flux according to equation (4.3) and monochromatic wave periods were taken as $P = 3500$ sec and $P = 8000$ sec, respectively. The model parameters are shown in Table (4.3).

In Figs. (4.26) and (4.27) we show snapshots of the wave calculations together with the initial and mean temperatures. Most of the shocks found in both models are quite small, but in each model one or two large shocks are present. These large shocks are the result of the merging of two or more of the smaller ordinary shocks. Note that the column mass density m at the bottom of the atmospheres of our giant stars is much larger than for the main sequence stars. This is due to the pressure dependence of the opacity. In dwarf stars the pressure and the opacity rise quickly and the optical depth of 1.3 is reached after going through much less mass.

The damping efficiency $\mathcal{E}$ for the giants is much larger than for a dwarf star of the same effective temperature. Furthermore the radiative damping zone are much more extended.

This results in a much greater radiative damping of the acoustic waves as they travel

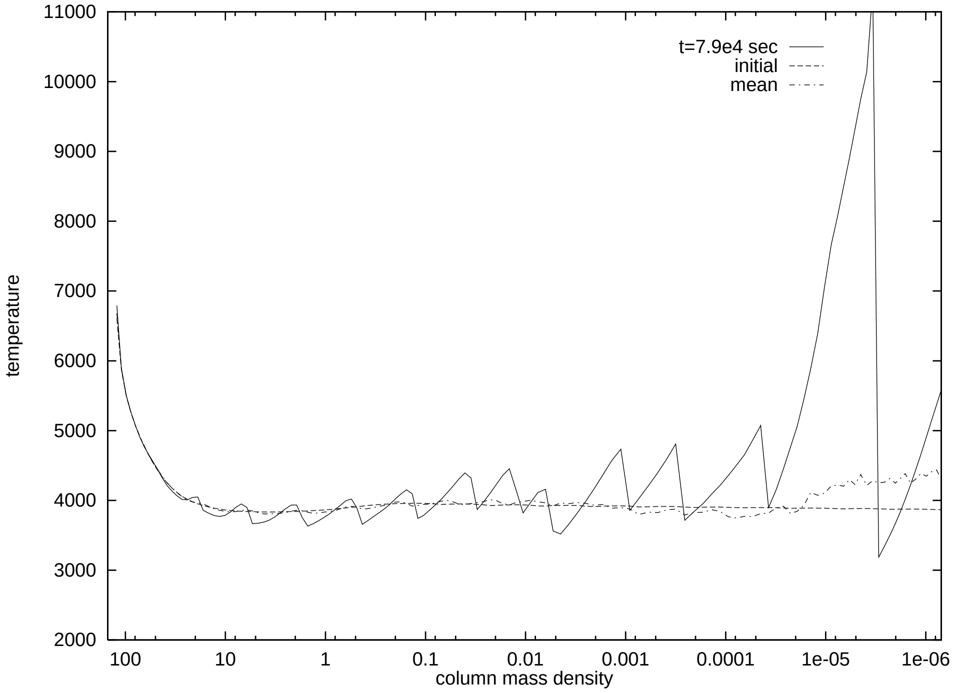

Figure 4.26: Temperature [K] vs. column mass density [g cm^{-2}] for the K0 III model. Shown are: temperature after $7.9 \cdot 10^4$ sec, initial radiative equilibrium temperature, and mean chromospheric temperature.

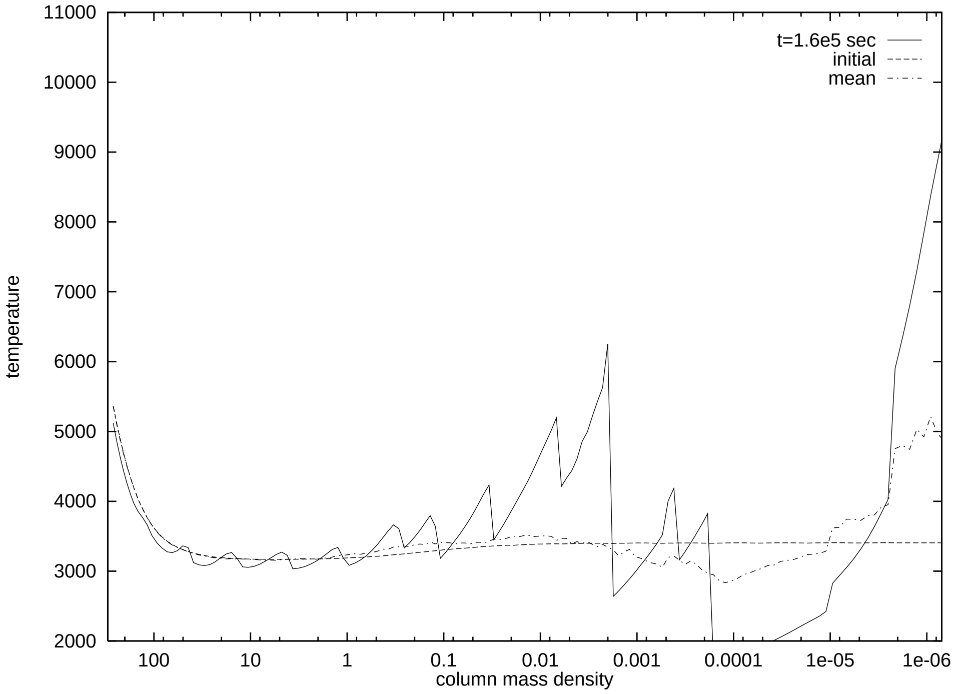

Figure 4.27: Temperature [K] vs. column mass density [g cm^{-2}] for the K5 III model. Shown are: temperature after $1.6 \cdot 10^5$ sec, initial radiative equilibrium temperature, and mean chromospheric temperature.

through the photosphere. By this effect the gravity dependence of the acoustic flux generation in the subphotospheric layers will not result in similar gravity dependence of the chromospheric line emissions. The time averaged cooling rates per gram for both stars still

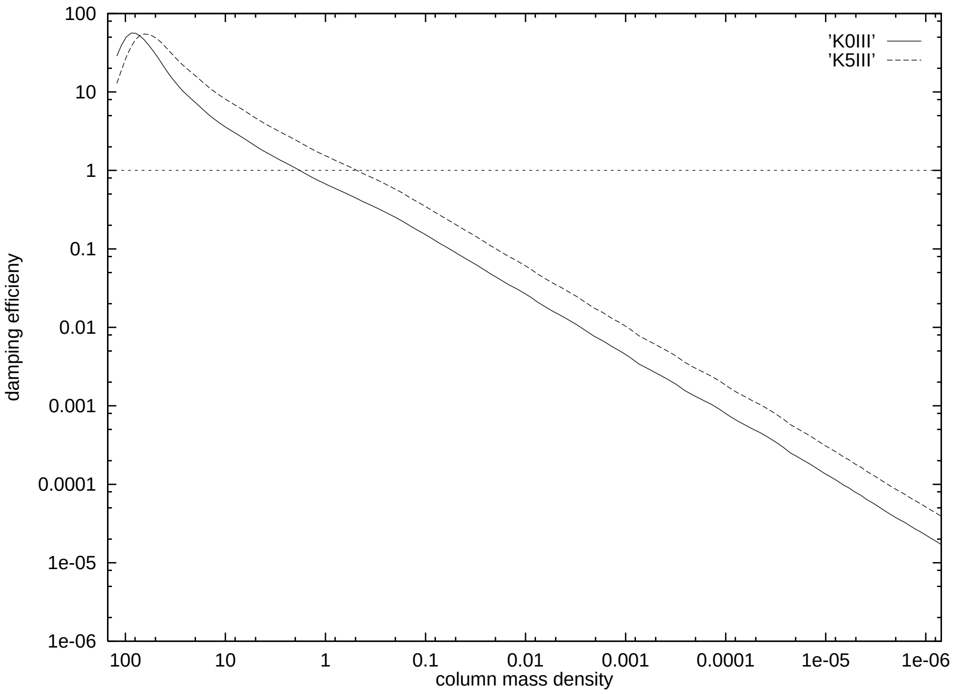

Figure 4.28: Radiative damping efficiency $\mathcal{E}$ vs. column mass density m [g cm^{-2}] for the time averaged giant models.

show large variations with height, indicating that the equilibrium state has not been reached yet. At the times depicted in Figs. (4.26) and (4.27) , 20 wave crests have entered the K5 giant and 14 still are present in the atmosphere. As several overtaking processes have occurred, no shock has left the atmosphere via the top boundary. The situation is similar for the K0 giant, where 26 wave periods have passed and 2 transmissions occurred. From equation (4.40) we expect a significant dependence of the limiting shock strength heating on gravity. The low gravity of the giant star results in a reduced heating rate per gram compared to the main sequence stars. For the K0 III model the heating rate calculated according to equation (4.32) is $1.5 \cdot 10^7 \mathrm{erg\,cm^{-1}\,sec^{-1}}$, which is by a factor of ≈ 200 lower compared to the main sequence stars, and for the K5 III star we find a reduction by a factor of ≈ 540. Despite the fact that our models are not yet in dynamical equilibrium, the time averaged cooling rates shown in Fig.(4.29) agree roughly with the results from equation (4.40). The time averaged chromospheric models do not show a temperature enhancement. The shocks did not heat up the atmosphere and the temperature stays near the equilibrium values. A similar result for a giant star with $T_{\mathrm{eff}} = 5012$ K and $\log g = 3$ has been found by Cuntz et al. (1994). In that paper, the author presented time dependent chromospheric

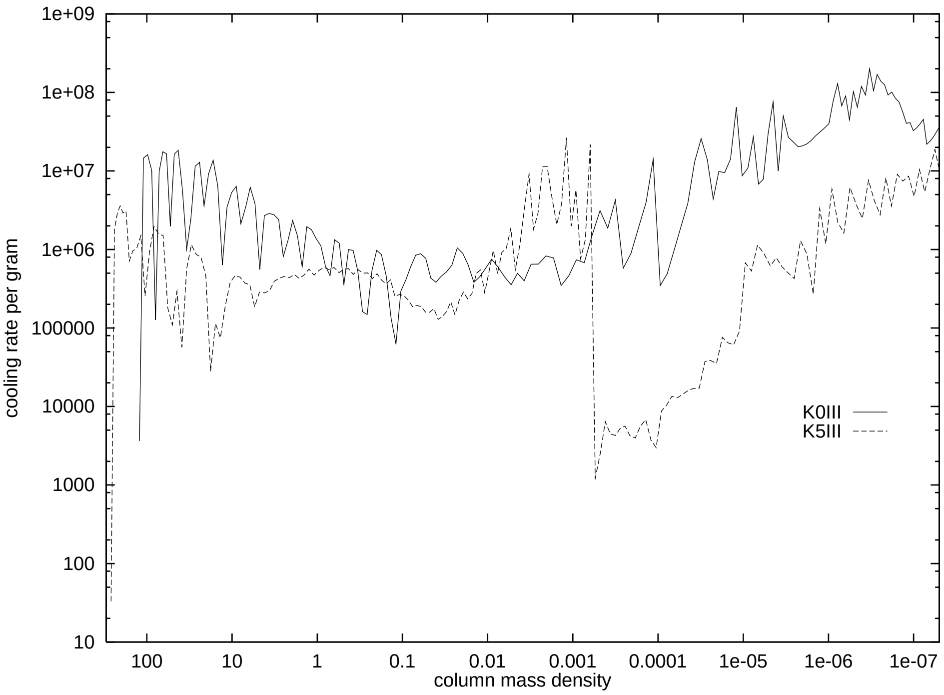

Figure 4.29: Time averaged cooling rate per gram [erg sec^{-1} g^{-1}] vs. mass column density [g cm^{-2} for the two giant stars.

	$T_{\rm eff}$	$\log g$	B-V	$\log F_{\rm M}$	$\log F_{\rm CaH+K}$	$\log F_{\rm Mgh+k}$
K0 III	4750 K	2.13	1.0	8.6	5.4	5.0
K5 III	3950 K	1.74	1.5	8.0	4.7	4.4

Table 4.3: Model parameters and mean emission fluxes for the giant stars.

models for stars with different metal abundances. Their model with solar abundances also did not exhibit a chromospheric temperature enhancement. Nevertheless the mean chromospheric emissions in CaII H+K and MgII h+k from their models are close to the basal flux line.

We show in Figure (4.30) the emergent line profile of the MgII k line for our K5 III star model. Due to the large shocks which form by overtaking, the variability of the profile is larger than for the dwarf stars. The mean chromospheric emission fluxes in CaII H+K and MgII h+k have been computed and are listed in Table (4.3). The emission fluxes for both stars are close to the basal flux line, as can be seen by comparing the results with those obtained for the main sequence stars (cf. Figure (4.19) and Table (4.2)). Our time dependent models thus reproduce the observational fact, that dwarf and giant stars show almost the same basal emission flux

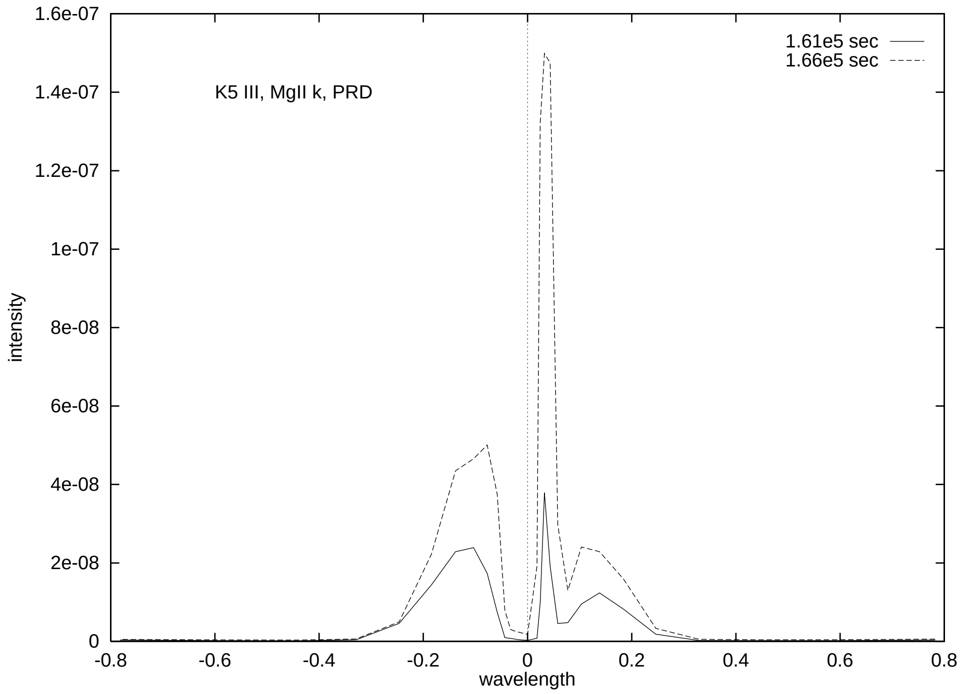

Figure 4.30: Emergent MgII line profile (PRD) from the K5 III model.Intensity (erg cm^{-2} sec^{-1} sr^{-1} Hz^{-1}) vs. displacement $\Delta\lambda$ [Å] from the line center at $\lambda_0 = 2796$ Å

Chapter 5

M-Dwarf chromospheres

5.1 Chromospheric Activity in M dwarfs

In a recent study of the chromospheric activity in M dwarf stars, Doyle et al. (1994) found for four stars of spectral class M the lowest emission fluxes yet detected. Despite relatively long integration times, only one of the four stars had detectable CaII H+K emissions. The surface flux derived from the observations for this star were found to be $8{\cdot}10^3$erg cm^{-2} sec^{-1}. Similarly, the IUE observations implied very weak MgII emission. In one of these stars the MgII h+k surface flux was less than $4{\cdot}10^3$erg cm^{-2} sec^{-1}. The predictions for these stars from the basal flux relation of Schrijver (1987) are $3 \cdot 10^4$erg cm^{-2} sec^{-1} which is about a factor of 7.5 higher. The combined fluxes of CaII and MgII observed were $\approx 2 \cdot 10^4$ erg cm^{-2} sec^{-1}

Another startling observation was the absence of H α in the spectra taken for the four low activity M dwarfs. The authors constructed semi-empirical models of these stars constrained by a zero equivalent width of H α and weak CaII H+K fluxes. The model atmospheres were based on Kurucz's (1991) model photosphere with $T_{\rm eff}$ = 3500K and the logarithm of the surface gravity was taken as $\log g = 4.8$. Above the photosphere an ad hoc chromospheric and transition structure was added with temperatures up to $3 \cdot 10^5$ K. Varying the positions of the temperature minimum and the base of the transition region, a series of model atmospheres were constructed and NLTE-radiation transfer calculations have been done to obtain the emission fluxes from CaII. The model calculations were performed under the condition of of hydrostatic equilibrium. We show in Figure (5.1) (from Doyle et al., 1994) the sequence of semi-empirical models. Best correspondence between the results of their modeling procedure and the observations were found for the models with the lower temperature minimum at $T_{\rm min}$ = 2660K. For these models a vanishing equivalent width of H α was found, together with a combined MgII and CaII emission flux of $2 \cdot 10^4$ erg cm^{-2} sec^{-1}.

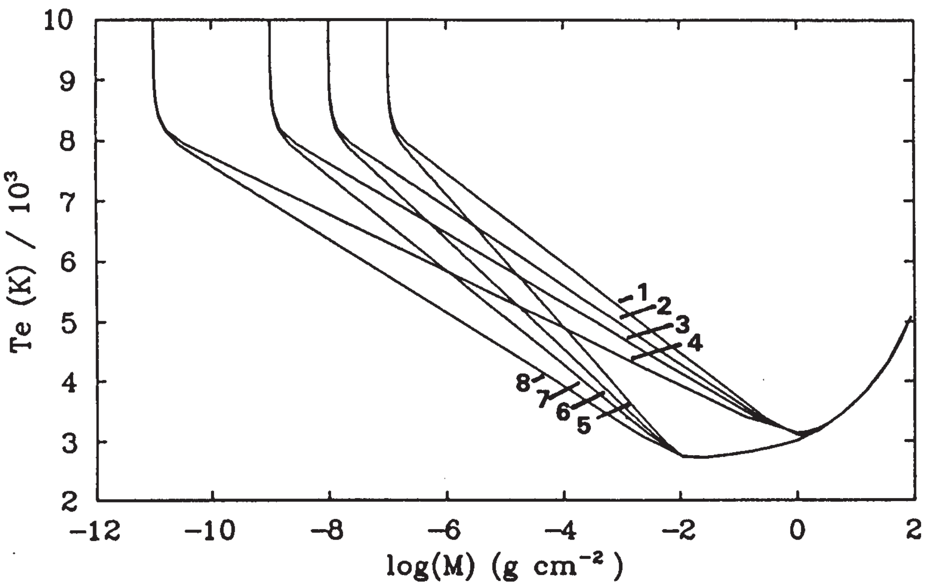

Figure 5.1: The set of 8 model atmospheres used by Doyle et al.(1994) for the calculations of the H α and CaII and MgII fluxes.

5.2 Molecular Opacities

The observational results of Doyle et al. (1994) clearly show, that the basal fluxes of M-dwarfs are not consistent with the flux-color relations adopted so far.

We constructed acoustic models of M dwarf chromospheres using the same methods described in the preceding chapter. In order to properly compute the radiative losses in the photosphere we had to modify the calculation of the opacities.

For our models of the chromospheres in main sequence stars of spectral class F0 V to M0 V we assumed that only the negative hydrogen ion H^- is responsible for the opacity in the photosphere. This approximation can no longer be justified if one considers stars of extremely low temperatures. Spectra of M dwarfs show absorption bands of several molecules among which H_2O and TiO are the most important.

We therefore added molecular opacities of TiO and water vapor to our models. Due to the low temperatures and the high densities it is possible to assume LTE conditions for the formation and destruction of the molecules. Since the total number of molecular lines is so large, a statistical approach is necessary to determine the effects of molecular opacity on the stellar absorption coefficients.

The absorption coefficients of H_2O which dominate the infrared opacity are interpolated in Ludwig's (1971) tables of *straight mean opacities*. The tables used, do not extend to wavelengths $\lambda < 1\mu m$. For that spectral range, H_2O opacities by Tsuji (1966) have been adopted.

For the opacities of the TiO molecules, which define the visual and near-infrared continuum in M dwarfs, we used tabulated straight mean opacities given by Collins (1975).

To save computer time we do not solve for the partial pressures of the molecules within the program but interpolate the values in a precomputed table provided to us by Allard and Hauschildt (1994). This table has been constructed by including 26 ionization stages of 39 elements as well as 105 molecules. For a detailed description of the method used to solve the equation of state and the full list of species included, see Allard and Hauschildt (1995). The table covers a temperature range of 960 K to 16800 K. The pressure ranges used for our models is $-6.00 \leq \log p \leq 8$.

We include the additional opacities in the calculation of the continuum radiative transfer. The method is the same used for radiation of H^- and the resulting radiative damping function of the continuous radiation is given by

$$D_{\rm cont} = \frac{4\pi}{T} \int_0^\infty [\kappa_\nu^{\rm bf} \, (J_\nu - S_\nu^{\rm bf}) + (\kappa_\nu^{\rm ff} + \kappa_\nu^{\rm mol})(J_\nu - B_\nu)] \, {\rm d}\nu \quad . \tag{5.1}$$

Here $\kappa^{\rm bf}$ and $\kappa^{\rm ff}$ are the opacities of H^- and the molecular opacities per gram $\kappa^{\rm mol}$ are simply added to the LTE opacities.

Contrary to the case of pure H^- radiation the opacities of H_2O and especially TiO show a large variation with wavelength λ. Therefore we need considerably more wavelength points to properly include the essential dependence of the opacity on λ. For the calculations presented in the preceding chapter, 19 wavelength points ranging from the far infrared at $\lambda = 35\,000\,$Å to the shortest wavelength at $\lambda = 1500\,$Å were sufficient to cover the variations of the H^- opacity with wavelength. With the molecular opacities included we need 90 wavelength points to properly resolve the run of the opacity with wavelength.

As the computational effort to solve the transfer equation grows linearly with the number of wavelength points used, we had to carefully select which wavelengths should be included in the calculations. In Figure (5.2) we show our selection of wavelength points in the range between $\lambda = 4000$Å and $\lambda = 35\,000\,$Å together with the opacity per gram of TiO and H_2O for $T = 2400$K and $\log p = 2$. The full line has been computed with 3500 wavelength points and the diamonds mark those wavelengths used in our calculations. The strong dependence of the molecular opacities on temperature and pressure is shown in Figure (5.3). In the wavelength range between 4000 Å and 10000 Å the opacity is dominated by TiO whereas water vapor is important for the longer wavelengths. The H_2O opacity is very sensitive to changes in temperature and pressure whereas TiO remains almost unaffected.

Due to the additional wavelengths and the need to interpolate the partial pressures and the opacities of the molecules, the computational time increases by a factor of 5 if molecular opacities are used.

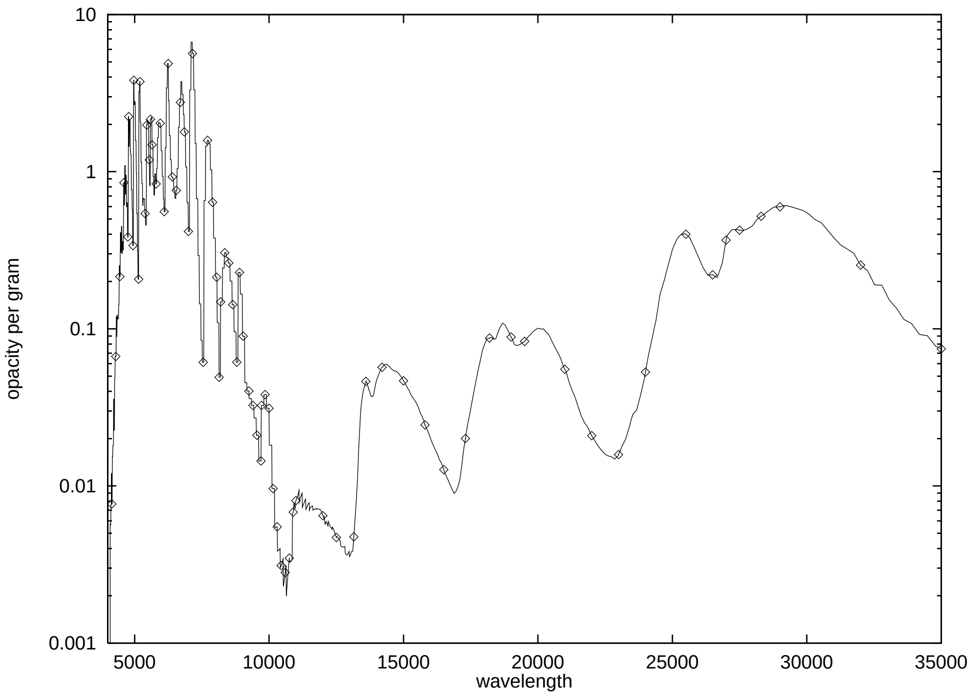

Figure 5.2: Molecular opacities per gram vs. wavelength $\lambda\,[\text{Å}]$. The wavelength points used in our time dependent calculations are marked with diamonds.

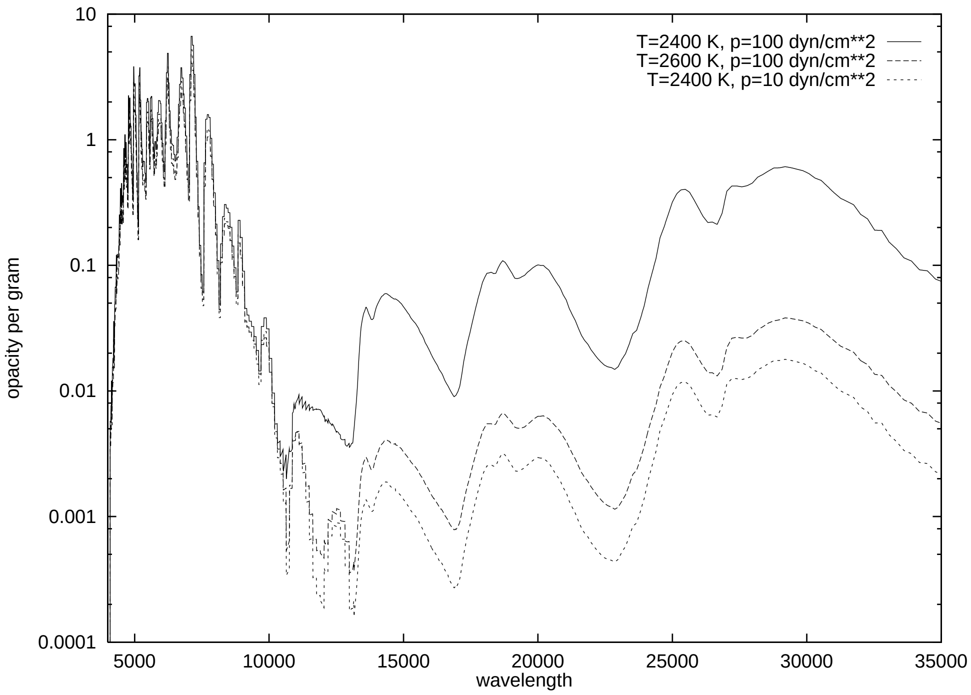

Figure 5.3: Molecular opacities per gram vs. wavelength $\lambda\,[\text{Å}]$ for different combinations of temperature and pressure.

5.3 Acoustically heated M-dwarf chromospheres

Doyle et al. (1994) constructed a semi-empirical model for a M dwarf with $T_{\rm eff} = 3500$K and $\log g = 4.8$. We used the same stellar parameters to calculate a radiative equilibrium model which includes the molecular opacities described above. Then we performed time dependent calculations in order to compare our results with those of Doyle.

The acoustic energy generation by turbulent convection has recently been revised by Musielak et al. (1994). Improved turbulent energy spectra were adopted for the calculation of the acoustic flux. On basis of convective velocities calculated by using Bohn's (1984) convective envelope code, the authors obtained the acoustic flux produced by the convection zone. This code employed gray radiative transfer without molecular opacities. For a star with iwith values of $T_{\rm eff}$ and $\log g$ as above an acoustic flux of only about $2{\cdot}10^3$erg cm^{-2} sec^{-1} was found (Ulmschneider, 1994, private communication).

The acoustic flux resulting from the calculations of Bohn (1984) for this stellar model would be $F_{\rm Bohn} = 1.0 \cdot 10^6$ erg cm^{-2} sec^{-1}.

A serious problem with the adoption of the method of Musielak et al. to M-dwarfs is that no molecular opacities had been included in the computation of the convective velocity fields. Thus the peak velocities in the convection zone are uncertain. Enhanced opacity by inclusion of molecules will bring the top of the convection zone to much shallower depths where the density is much lower. In this case the convective velocities must be considerably larger in order to transport the convective flux. As the acoustic flux generation scales with the eighth power of the convective velocity (Lighthill, 1952), this would greatly increase the resulting acoustic flux. thus a realistic flux for the above M-dwarf is expected to be much closer to Bohn's results.

In view of this problem and noting that the acoustic flux of $2 \cdot 10^3$ erg cm^{-2} sec^{-1} is even smaller than the very small observed emission fluxes from the least active M dwarfs, we use higher acoustic fluxes.

Another result from acoustic energy generation is that the peak of the acoustic flux spectrum is shifted towards longer periods for cooler M dwarfs. Therefore we can no longer simply adopt a monochromatic wave period of $P = 0.2 \cdot P_{\rm ac}$ but must use longer periods instead.

By using different acoustic input fluxes and wave periods we computed model chromospheres for the M dwarf in order to determine which combination will reproduce best the observations of Doyle at al. (1994). Moreover we want to compare our mean chromospheric models with their semi-empirical models.

We choose for our grid of chromospheric models input fluxes of $1.0 \cdot 10^6$ erg cm^{-2} sec^{-1}, $1.0 \cdot 10^5$ erg cm^{-2} sec^{-1}, and $2.0 \cdot 10^4$ erg cm^{-2} sec^{-1}. The wave periods are 15, 25, 40, 60, and 70 seconds and span the range from $0.2 \times P_{\mathrm{ac}}$ to $0.9 \times P_{\mathrm{ac}}$.

Due to numerical problems with the wave code the calculations with the largest flux could only be performed for the short period waves. The large wave flux together with the longer wave periods produced a large scale oscillation of the atmosphere which finally caused overflow error conditions. Therefore we could not include the models with periods of more than 25 seconds in our analysis. We show in Figure (5.4) the resulting mean chromospheric models for the remaining two wave periods. The time averaged chromosphere of the M dwarf

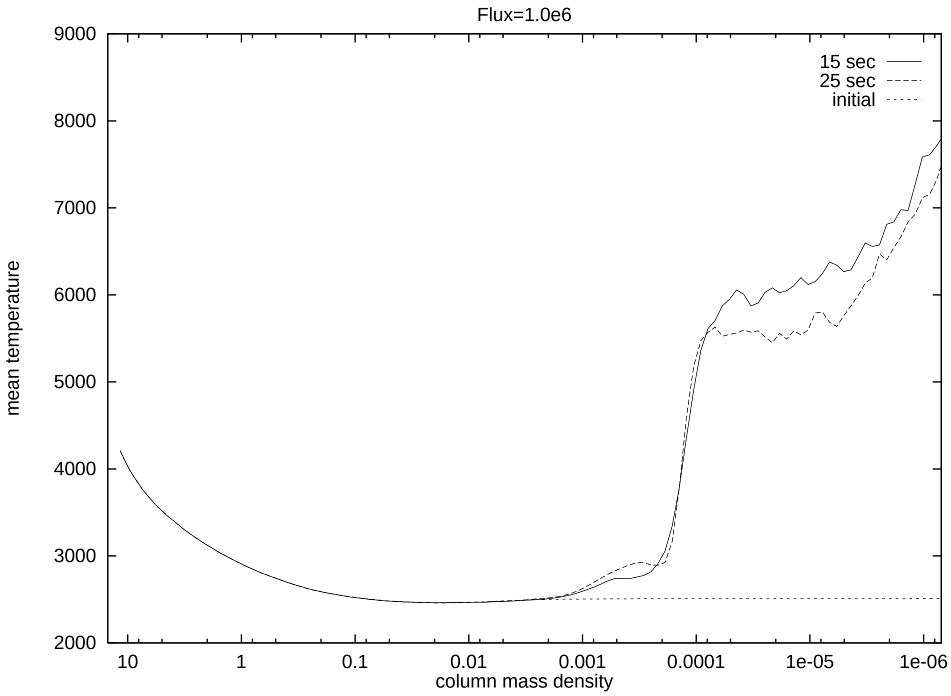

Figure 5.4: Mean chromospheric models for the M dwarf with $T_{\mathrm{eff}} = 3500$K and $\log g = 4.8$. Shown are the mean temperatures and the initial radiative equilibrium temperature. The acoustic input flux is $1.0 \cdot 10^6$ erg cm^{-2} sec^{-1}

closely resemble those of the other main sequence star chromospheres. The temperature inversion starts at $m = 2.5 \cdot 10^{-3}$ g cm^{-2}. The initial temperature enhancement is small and an intermediate temperature plateau at 2800 K is formed. At $m = 2.5 \cdot 10^{-4}$ g cm^{-2} the temperature steeply rises and reaches the final plateau with $T = 6000$K. The model calculated with $P = 25$ sec has a plateau temperature of 5500 K.

No temperature depression below the radiative equilibrium temperature is found in the M dwarf models. The wave amplitudes are too small to produce large deviations from the equilibrium state until the shocks form.

The models with the lower input fluxes could be computed without numerical problems. Therefore a complete set of mean chromospheric models with a flux of $F_{\mathrm{M}} = 1.0 \cdot 10^5$ erg cm^{-2} sec^{-1} is shown in Figure (5.5). Note the difference in the mass column density ranges shown in Figs. (5.4) and (5.5). The first apparent difference between the models with $F_{\rm M} = 1.0 \cdot 10^6$ erg cm^{-2} sec^{-1} and those of $F_{\rm M} = 1.0 \cdot 10^5$ erg cm^{-2} sec^{-1} is the disappearance of the 6000K-temperature plateau. In all stellar models including the main sequence stars described in Chapter 4, the temperature plateau extended up to a column mass density of about $m = 5.0 \cdot 10^{-6}$ g cm^{-2}. At greater heights the temperature started to increase further to values of over 10000 K. We did not discuss these atmospheric regions because our models do not allow for ionization of hydrogen. Thus the models can not reflect the correct physical state of the hotter regions. The rapid temperature growth in the layers above the temperature plateau is caused by the vanishing influence of radiative cooling by MgII. The gas is essentially adiabatic and the shocks are able to heat up the outer atmosphere to very large temperatures.

In our M dwarf models with the lower flux, the initial temperature increase is shifted outward to atmospheric regions with column mass densities of $m \leq 2.0 \cdot 10^{-5}$ g cm^{-2}. Therefore the steep temperature gradient reaches those regions where little line cooling remains. Instead of forming the plateau like structure, the temperature grows further. A

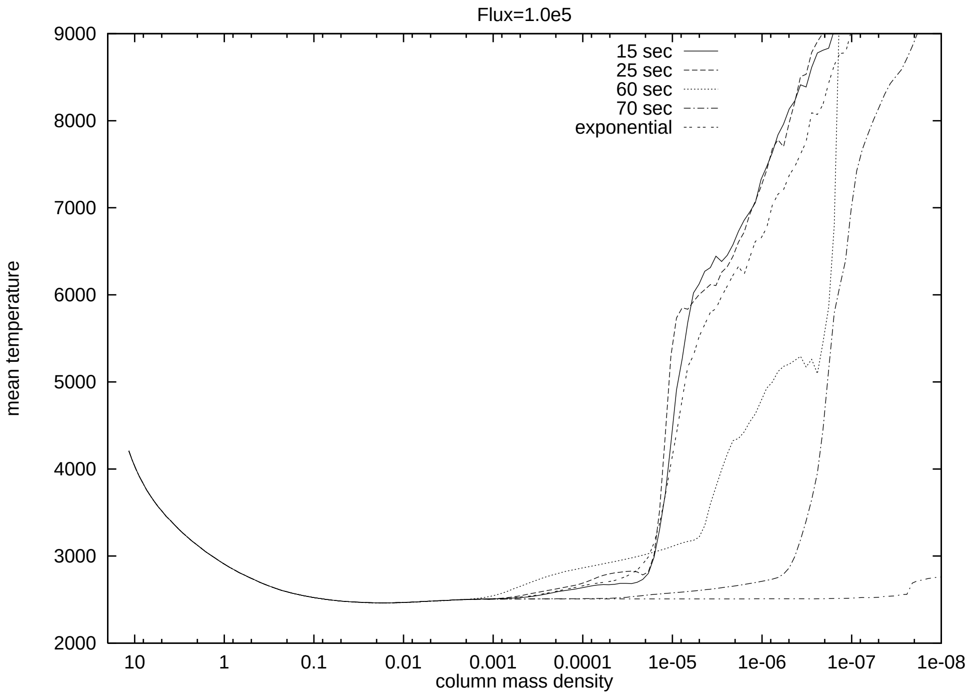

Figure 5.5: Mean chromospheric models for the M dwarf with $T_{\rm eff} = 3500$K and $\log g = 4.8$. Shown are the mean temperatures and the initial radiative equilibrium temperature. The acoustic input flux is $1.0 \cdot 10^5$ erg cm^{-2} sec^{-1}

similar result is found if we reduce the input flux further to a value of only $F_{\rm M} = 2.0 \cdot 10^4$ erg cm^{-2} sec^{-1}. Here again a steep temperature gradient is found at even lower densities and the temperature grows to transition region values without forming a plateau (cf. Fig

(5.6)).

In Figs.(5.5) and (5.6) we include a mean chromospheric model obtained from calculations with an acoustic spectrum instead of monochromatic waves. We were only able to perform these calculations with low input fluxes. The models with the highest flux showed the same problems we already encountered with the long period monochromatic waves. This is due to the fact, that the acoustic spectrum used contains partial waves with long periods.

The calculation of the acoustic spectrum was performed similar to the method of Sutmann and Ulmschneider (1994). For the calculations with acoustic spectra the motion of the piston at the bottom of our model atmosphere is determined as superposition of the partial waves. The time dependent velocity is computed as

$$u(t) = c_{\mathrm{s}} \sum M_n \cdot \sin(\omega_n t + \phi_n) \tag{5.2}$$

with the sound speed c_{s} and the Mach numbers M_n of the partial waves of frequency ω_n. The wave phases ϕ_n are arbitrary chosen but fixed throughout the calculations. For a given mechanical input flux F_{M} the Mach numbers of the partial waves are taken as

$$M_n = q\sqrt{\frac{F_{\mathrm{M}}}{\varrho c_{\mathrm{s}}^3}} \cdot f(\omega_n) \quad . \tag{5.3}$$

Here q is a normalization factor and the spectral distribution function $f(\omega_n)$ is given as

$$f(\omega_n) = \mathcal{N} \exp[-\frac{\omega_n}{\omega_{\mathrm{ac}}}] \quad . \tag{5.4}$$

This choice of $f(\omega_n)$ indicates that we use an exponential spectrum with exponentially decreasing amplitudes of the partial waves. Our choice is suggested by the acoustic spectra calculated by Bohn (1991) which show that the largest part of acoustic energy in M-dwarfs is produced at frequencies near the acoustic cutoff frequency. The acoustic power quickly decreases towards higher frequencies. The most interesting result from the calculations with acoustic spectra is, that the time averaged chromospheric models closely resemble those calculated with short period waves with $P \approx 15$ to 25 sec of the same input flux.

This agrees with the surprising results of Sutmann and Ulmschneider (1994), that the heating behavior by an acoustic frequency spectrum, largely independent of the shape of the spectrum, is similar to that of a short period monochromatic wave with $P \approx 0.2 \cdot P_{\mathrm{ac}}$.

5.4 Chromospheric Emissions

The calculations presented so far have been performed to investigate the properties of acoustically heated M dwarf chromosphere models. Comparing the models from Fig.(5.1) with our mean chromospheric models significant differences can be seen. The semi-empirical models of M stars do not resemble the mean models as they result from dynamical modeling.

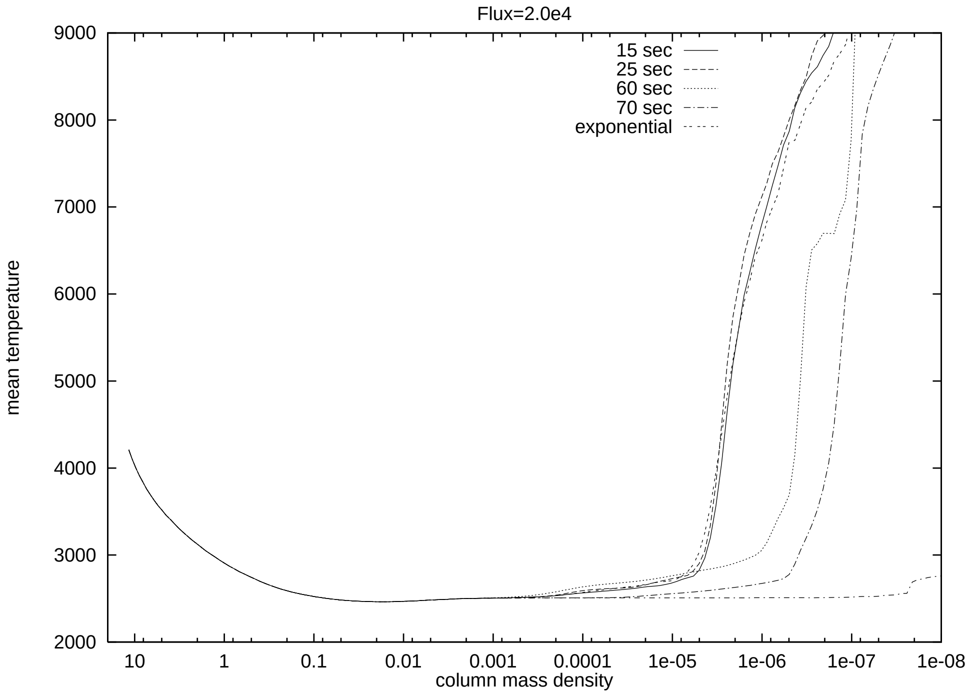

Figure 5.6: Mean chromospheric models for the M dwarf with $T_{\rm eff}$ = 3500K and $\log g$ = 4.8. Shown are the mean temperatures and the initial radiative equilibrium temperature. The acoustic input flux is $1.0 \cdot 10^5 \mathrm{erg\,cm^{-2}\,sec^{-1}}$

Neither the position of the temperature minimum nor the slope of the temperature inversion of our mean chromospheric models are similar to those of the models used by Doyle et al. (1994). We find from our calculations a broad temperature minimum region with $T_{\rm min} \approx 2500$ K, 300 K less than the value adopted by Doyle et al.

One result of the model calculations for the main sequence stars of earlier spectral classes was, that one has to use the time dependent models to obtain the correct emission fluxes. We therefore calculated for the models shown in the preceding section the emission fluxes of CaII H+K and MgII h+k.

We show in Figures (5.7) and (5.8) the variations with time of the MgII k line and the CaII K line for the model with a period of P = 15 sec and a flux of $F_{\rm M} = 1.0 \cdot 10^6$ erg cm^{-2} sec^{-1} The mean chromospheric fluxes found in this model star are $F_{\rm Mg} = 1.9 \cdot 10^4$ erg cm^{-2} sec^{-1} and $F_{\rm Ca} = 4.3 \cdot 10^3$ erg cm^{-2} sec^{-1} in excellent agreement with the observational results of Doyle et al. The model with $P = 25$ sec showed a similar emission flux. However, from the models with $F_{\rm M} = 1.0 \cdot 10^5$ erg cm^{-2} sec^{-1} we obtain emission fluxes of $F_{\rm Mg} \leq 800$ erg cm^{-2} sec^{-1} well below the observations.

This indicates, as already suspected above, that the Bohn(1994) fluxes for M-dwarfs are more realistic than those obtained using the approach of Musielak et al. (1994) with inadequate convection zone velocities.

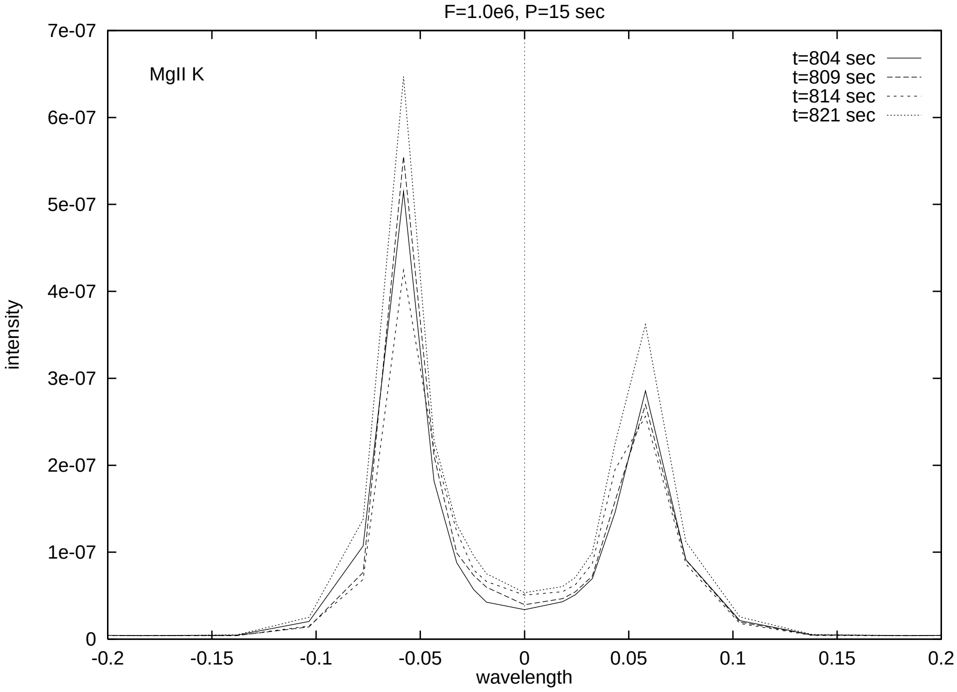

Figure 5.7: Intensity variations with time for the MgII k line (PRD) from the M dwarf model. Intensity erg cm^{-2} sec^{-1} sr^{-1} Hz^{-1} vs. displacement $\Delta\lambda$[Å] from the line center at $\lambda_0 = 2796$Å

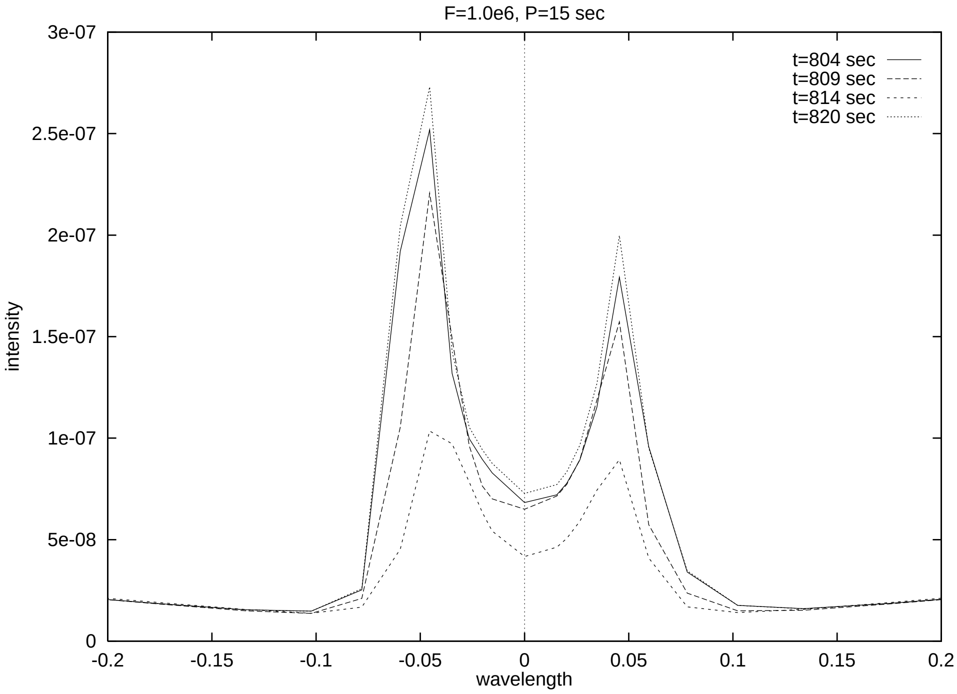

Figure 5.8: Intensity variations with time for the CaII k line (PRD) from the M dwarf model. Intensity erg cm^{-2} sec^{-1} sr^{-1} Hz^{-1} vs. displacement $\Delta\lambda$[Å] from the line center at $\lambda_0 = 3933$Å

Chapter 6

Conclusions

We computed time dependent models of chromospheres for late type stars of spectral types F0 V to M0 V and for two giant stars of spectral type K0 III and K5 III. Starting from initial model atmospheres in radiative equilibrium we induced acoustic waves with wave energy fluxes and periods according to theoretical calculations of Bohn (1981,1984). On basis of these theoretical acoustic chromosphere models, time dependent emission line profiles and time averaged emission fluxes in PRD were computed and the results compared with observations. We analyzed our time-averaged chromospheric models and discussed them relative to semi-empirical models.

- In order to properly treat the radiation losses by spectral lines in shock permeated atmospheres, a new fast and stable solution method for the radiative transfer equation has been developped.

- We found that the efficiency of acoustic energy transfer from the photosphere into the chromosphere increases with decreasing $T_{\rm eff}$ for the main sequence stars. The large extent of the radiative damping zone found for stars of spectral type K0 V and earlier, leads to severe radiative damping of the acoustic waves. For later type main sequence stars the wave flux is almost unaltered by radiative damping in the photosphere.

- The positions of the temperature minima found in the time averaged chromospheric models of stars between spectral types F5 V and M0 V obey the simple linear scaling law found empirically by Ayres (1979). For the stellar model of spectral type F0 V no significant temperature enhancement was found and therefore no pronounced temperature minimum is seen.

- The height dependence of the heating rates is found to be consistent with the limiting shock strength behavior as derived in Eq.(4.40). From this theory and the numerical computations we find a universal constant heating rate per gram of chromospheric regions where the shocks have reached their limiting strength. This heating rate is consistent with the results from semi-empirical modeling of the solar chromosphere by Anderson and Athay (1989). For the two giants the heating rate is lower by factors of 200 to 540 as expected from the limiting shock strength result of Eq.(4.40).

- The time averaged emission fluxes for the most important chromospheric diagnositic lines, CaII H+K and MgII h+k, simulated in our models for both main sequence stars and giants, are in very good agreement with the empirically established basal flux line (Rutten et al. 1991). By reproducing this observational fact with our theoretical modeling we can make it essentially certain, that the basal emission is indeed the result of acoustic heating.

- We extended our investigation to the cool M-dwarfs of spectral type M4 V and later. In order to ensure a realistic computation of the radiation losses at photospheric levels for these stars, wavelength dependent molecular opacities of H2O and TiO have been included. To our knowledge this is the first time such a detailed treatment of molecular opacities in time dependent modeling of chromospheres has been done.

- We generated a grid of M-dwarf models with different acoustic fluxes and wave periods in order to investigate the dependence of chromospheric properties on these parameters. Using acoustic fluxes according to Bohn (1984) we were able to reproduce recent observations of the lowest chromospheric emission fluxes of M-dwarfs (Doyle et al. 1994).

- Dynamical models are very different from monotonic models because the regions of line formation are the hot post shock parts of the waves. The positions as well as the temperatures and the densities of these regions vary with time as the waves propagate. Clearly this time dependent behavior can not be reproduced by the static models usually adopted for semi-empirical studies. Our F0 V-star model shows, that basal chromospheric emission flux can be produced by a time-dependent model which will not lead to a temperature enhancement of the corresponding time averaged model.

- Calculations of M-star models performed with acoustic spectra instead of monochromatic waves confirmed recent results of Sutmann & Ulmschneider (1994) concerning the dynamical properties of stellar atmospheres. We found that the mean chromospheres resulting from an realistic acoustic spectrum closely resemble those obtained with a monochromatic wave of the same flux and with a period of 1/5 the acoustic cutoff period.

As a concluding summary of all our results and the discussed work from other authors it now appears essentially certain that acoustic waves are the basic heating mechanism which is present in all stars.

Secondly, for realistic chromosphere models, it is absolutely essential to use time-dependent dynamical modeling.

In order to overcome the limitations of our modeling procedure, future investigations should use a more realistic treatment of the spectral line radiation. From semi-empirical modeling by Anderson and Athay (1989) we now know, that the myriads of subordinate lines generate a greater emission loss than the few prominent and strong lines used in this work.

Furthermore the effects of hydrogen ionization will have to be considered to get the correct solutions for the transition layer regions with temperatures above 10 000 K.

Bibliography

[1] Achmad L., de Jager C., and Nieuwenhuijzen H.: 1991, *Astron. Astrophys.* **250**, 445

[2] Allard F., Hauschildt P.H.: 1995, *Astrophys. J.* , in press

[3] Anderson L.S.,Athay,R.G.: 1989a, *Astrophys. J.* **336**, 1089

[4] Anderson L.S.,Athay,R.G.: 1989b, *Astrophys. J.* **346**, 1010

[5] Auer L.: 1987, in:*Numerical Radiative Transfer*, W.Kalkofen, Ed. Cambridge Univ.Press, Cambridge, England, p.101

[6] Auer L.: 1991, in: Stellar Atmospheres: Beyond Classical Models, L.Crivellari et al. Eds., Kluwer, Dordrecht, Netherlands, p.9

[7] Ayres T.R.: 1975, *Astrophys. J.* **201**, 799

[8] Ayres T.R.: 1979, *Astrophys. J.* **228**, 509

[9] Biermann L.: 1946, *Naturwiss.* **33**, 118

[10] Böhm-Vitense E., Dettman T.: 1980, *Astrophys. J.* **236**, 560

[11] Bohn H.U.: 1981, *Ph.D.Thesis* , Univ. Würzburg, Germany

[12] Bohn H.U.: 1984, *Astron. Astrophys.* **136**, 338

[13] Browne J.C., Dalgarno A.: 1969, *J. Phys. B* **2**, 885

[14] Buchholz B., Hauschildt P.H., Rammacher W., Ulmschneider P.: 1994, *Astron. Astrophys.* **285**, 987

[15] Buchholz B., Ulmschneider P.: 1994, *in: Cool Stars, Stellar Systems and the Sun*, J.P. Caillault Ed., ASP Conf. Series **64**,p.393

[16] Byrne P.B.: 1993, *Astron. Astrophys.* **278**, 520

[17] Cayrel R.: 1964, *SAO Special Report* **167**, 169

[18] Cheng Q.Q.: 1991, Ph.D.Thesis, Univ. Heidelberg, Germany

[19] Collins J.G.: 1975, *J.Phys. B* **0**, 304

[20] Courant R., Friedrichs K.O.: 1948, *Supersonic Flows and Shock Waves*, Interscience, New York

[21] Cuntz M.,Rammacher W.,Ulmschneider P.: 1994, *Astrophys. J.* **432**, 690

[22] Deubner F.-L.:1988, in: Pulsations and Mass Loss in Stars, R. Stalio, L.A.Willson Eds., Kluwer, Dordrecht, p. 163

[23] Doyle J.G., Houdebine E.R., Mathioudakis M., and Panagi P.M.: 1994, *Astron. Astrophys.* **285**, 233

[24] Duncan D.K., Vaughan A.H. et al.: 1991, *Astrophys. J.Suppl.* **76**, 383

[25] Dzhalilov N.S., Zhugzhda Y.D, and Staude J.: 1994, *Astron. Astrophys.* **291**, 1001

[26] Edlen B.: 1942, *Z. Astrophys.* **22**, 30

[27] Endler F., Deubner F.-L.: 1983, *Astron. Astrophys.* **121**, 291

[28] Gebbie K.B., Thomas R.N.: 1970, *Astrophys. J.* **161**, 229

[29] Gouttebroze P.: 1986, *Astron. Astrophys.* **160**, 195

[30] Gouttebroze P.: 1989, *Astron. Astrophys.* **337**, 536

[31] Hartree D.R.: 1952, *Los Alamos Report LA-HU-1*,

[32] Jordan St.D.: 1993, *Astrophys. J.* **414**, 337

[33] Kalkofen W., Ulmschneider P.: 1977, *Astron. Astrophys.* **57**, 193

[34] Kalkofen W., Ulmschneider P., Schmitz F.: 1984, *Astrophys. J.* **287**, 952

[35] Kalkofen W. Ulmschneider P.: 1984, *in: Methods of Radiative Transfer, Hrsg.: Kalkofen W.*, Cambridge Univ. Press

[36] Kuperus M., Ionson J.A., Spicer D.S.:1981, *Ann. Rev. Astron. Astrophys.* **19**,7

[37] Kurucz R.: 1970, *Smithsonian Astrophys. Obs. Spec. Rept.* **309**,

[38] Landau L.D., Lifshitz E.M.: 1959, *Fluid Mechanics*, Pergamon Press, London

[39] Lighthill M.J.: 1952, *Proc.Roy.Soc. London* **A211**,564

[40] Lister M.: 1960, *in :Math. Methods for Digital Computers I*, Hrsg.: Ralston A., Wilt H.S., Wiley, New York

[41] Ludwig C.B.: 1971, *Applied Optics Vol 10* **5**, 1057

[42] Paletou F., Auer L.H.: 1995, *Astron. Astrophys.* , submitted

[43] Mathioudakis M. and Doyle J.G.: 1992, *Astron. Astrophys.* **262**, 523

[44] McWhirter R.W.P., Thonemann P.C. Wilson R.: 1975, *Astron. Astrophys.* **40**, 63

[45] Menzel D.H.: 1937, *Astrophys. J.* **85**, 330

[46] Middlekop F.: 1982, *Astron. Astrophys.* **113**, 1

[47] Mihalas D.: 1978, *Stellar Atmospheres*, Freeman, San Francisco

[48] Mihalas D., Mihalas B.W.: 1984, *Foundations of Radiation Hydrodynamics*, Oxford University Press

[49] Milkey R.W., Mihalas D.: 1973, *Astrophys. J.* **70**, 213

[50] Musielak Z.E., Rosner R., Stein R.F.,Ulmschneider P.: 1994, *Astrophys. J.* **423**, 474

[51] Narain U., Ulmschneider P.:1990, *Space Sci. Rev.,* **54**,377

[52] Narain U., Ulmschneider P.:1995, *Space Sci. Rev.,* in press

[53] Olson G.L., Auer L., Buchler J.R.: 1986, *J. Quant.Spectroc. Radiat. Transfer* **35**, 431

[54] Olson G.L., Kunasz P.B.: 1987, *J.Quant. Spectrosc. Radiat.Transfer* **38**, 325

[55] Oranje B.J., Zwaan C.: 1985, *Astron. Astrophys.* **147**, 265

[56] Rammacher W.:1991, Ph.D.Thesis, Univ. Heidelberg, Germany

[57] Rammacher W., Ulmschneider P.: 1992, *Astron. Astrophys.* **253**, 586

[58] Rutten R.G.M.: 1986, *Astron. Astrophys.* **159**, 291

[59] Rutten R.G.M., Schrijver C.J., Zwaan C., Duncan D.K. and Mewe R.: 1989, *Astron. Astrophys.* **219**, 239

[60] Rutten R.G.M., Schrijver C.J., Lemmens A.F.P., and Zwaan C.: 1991, *Astron. Astrophys.* **252**, 203

[61] Schmieder B.: 1977, *Solar Physics* **54**, 269 Schmitz F.,Ulmschneider P., Kalkofen W.: 1985, *Astron. Astrophys.* **148**, 217

[62] Schmitz F.: 1990, *Astron. Astrophys.* **229**, 177

[63] Schrijver C.J., Cote J., Zwaan C., Saar S.H.: 1989, *Astron. Astrophys.* **337**, 964

[64] Schrijver C.J.:1987 in Cool Stars, Stellar Systems and the Sun, J.L.Linsky, R.E.Stencel Eds., Lecture Notes in Physics **291**, Springer, Berlin, Germany

[65] Shine R.A.: 1973, *Ph.D. Thesis* , Univ.n Colorado

[66] Simon T., Landsmann W.: 1991, *Astrophys. J.* **380**, 200

[67] Spiegel E.A.: 1957, *Astrophys. J.* **126**, 202

[68] Stein R.F., Spiegel E.A.: 1967, *J. Acoustical Soc. of America* **42**, 866

[69] Stilley J.L., Callaway J.: 1970, *Astrophys. J.* **160**, 245

[70] Sutmann G.,Ulmschneider P.: 1995, *Astron. Astrophys.* , in press

[71] Tsuji T: 1966, *Publ. Astron. Soc. Japan* **18**, 127

[72] Ulmschneider P.: 1971, *Astron. Astrophys.* **14**, 275

[73] Ulmschneider P., Kalkofen W., Nowak T., Bohn U.: 1977, *Astron. Astrophys.* **54**, 61

[74] Ulmschneider P.: 1979, *Space Science Review* **24**, 71

[75] Ulmschneider P., Muchmore D., Kalkofen W.: 1987, *Astron. Astrophys.* **177**, 292

[76] Ulmschneider P.: 1989, *Astron. Astrophys.* **222**, 171

[77] Ulmschneider P.:1990, in Cool Stars, Stellar Systems and the Sun, G. Wallerstein Ed., **ASP** Conf.Series **9**,p 15

[78] Ulmschneider P.: 1994, *Astron. Astrophys.* **288**, 1021

[79] Unsöld A.: 1955, *Physik er Sternatmosphären*, Springer-Verlag,, Berlin

[80] Unsöld A.: 1963, *Zeitschritf für Physik* **171**, 44

[81] Vardavas I.M.: 1976, *J.Quant. Spectrosc. Radiat.Transfer* **16**, 781

[82] Vernazza J.E., Avrett E.H., Loeser R.: 1973, *Astrophys. J.* **184**, 605

[83] Vernazza J.E., Avrett E.H., Loeser R.: 1981, *Astrophys. J.Suppl.* **45**, 635

[84] Walter F.M., Schrijver C.J.:1987, in: Cool Stars, Stellar Systems and the Sun, J.L.Linsky,R.E.Stencel Eds., Lecture Notes in Physics **291**, Springer, Berlin, Germany

[85] Whitham G.B.: 1974, *Linear and Nonlinear Waves*, John Wiley & Sons, New York

[86] Wiese W.L., Smith M.W., Miles B.M.: 1969, *Atomic Transition Probabilities, Vol* **2**, (NSRDS-NBS 22); Washington: GPO

[87] Wolf B.E., Schmitz F., Ulmschneider P.: 1981, *Astron. Astrophys.* **97**, 101

Danksagung

Diese Arbeit wurde unter der Anleitung von Herrn Prof. Dr. P.Ulmschneider durchgeführt. Seine stetes Interesse und die vielfältigen Hinweise und Anregungen haben wesentlich zum Erfolg dieser Arbeit beigetragen. Insbesondere sei ihm für seine Bemühungen um finanzielle Unterstützung gedankt, die es mir ermöglichten, die Resulate dieser Arbeit auf der Konferenz "Cool Stars, Stellar Systems and the Sun 8" in Athens, GA vorzustellen.

Herrn Priv. Doz. Dr. J.Krautter bin ich dankbar für seine Geduld und die Bereitschaft, über die Feiertage das Zweitgutachten zu erstellen.

Herrn Dr. P.Hauschildt danke ich für viele Anregungen und Hilfestellungen bei Problemen des Strahlungstransportes. Ich verdanke ihm auch die Daten und Routinen zur Behandlung der Molekülopazitäten. Seine Hilfsbereitschaft und Gastfreundschaft ermöglichten mir den Aufenthalt an der Arizona State University in Tempe, AZ.

Ich danke Herrn Dipl.Phys. M.Däther und Herrn Dipl.Phys. Rainer Kürschner, ohne deren unermütlichen Einsatz für ein reibungsloses Funktionieren der Netzwerke und Workstations die Fertigstellung dieser Arbeit schwierig geworden wäre.

Besonderer Dank gilt auch Herrn Dr. S.Viergutz für seinen Einsatz beim Korrekturlesen, das ihn bis in die frühen Morgenstunden beschäftigte.

Den Teilnehmern unserer allmittäglichen "Kaffeerunde" gebührt Dank für die stressreduzierenden Gesprächsthemen, die nur selten mit Astronomie zu tun hatten.

Allen Mitarbeiterinnen und Mitarbeitern des ITA sei hier für die entspannte Arbeitsatmosphäre gedankt.

Ganz besonders aber danke ich meiner geliebten Susanne, die mich ertragen hat, wenn ich unerträglich war, und mir auf vielfältige Weise immer wieder Kraft gegeben hat.

Für die finanzielle Unterstützung dieser Arbeit danke ich der Deutschen Forschungsgemeinschaft (Projekt Ul 57/14–1) und dem Land Baden–Württemberg, das mir im Rahmen der Landes-Graduierten-Förderung ein Stipendium gewährte.